

SPIN-SPIN INTERACTIONS OF MAGNETIC IMPURITIES IN GRAPHENE NANORIBBONS

**A Thesis Submitted to
the Graduate School of Engineering and Sciences of
İzmir Institute of Technology
in Partial Fulfillment of the Requirements for the Degree of**

MASTER OF SCIENCE

in Physics

**by
Anıl KOLAY**

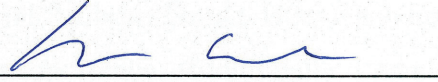
**July 2019
İZMİR**

We approve the thesis of **Anıl KOLAY**

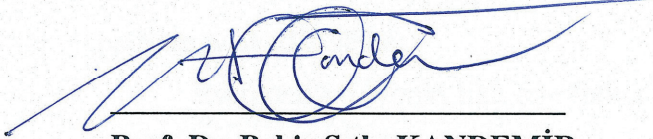
Examining Committee Members:



Assoc. Prof. Dr. Alev Devrim GÜÇLÜ
Department of Physics, İzmir Institute of Technology

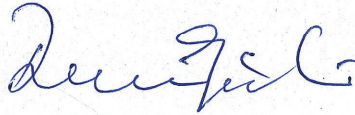


Prof. Dr. Nejat BULUT
Department of Physics, İzmir Institute of Technology

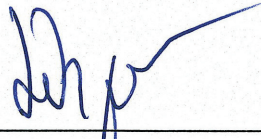


Prof. Dr. Bekir Sıtkı KANDEMİR
Department of Physics, Ankara University

17 July 2019



Assoc. Prof. Dr. Alev Devrim GÜÇLÜ
Supervisor, Department of Physics
İzmir Institute of Technology



Prof. Dr. Lütfi ÖZYÜZER
Head of the Department of
Physics

Prof. Dr. Aysun SOFUOĞLU
Dean of the Graduate School of
Engineering and Sciences

ACKNOWLEDGMENTS

I would like to express my deepest gratitude and sincerest appreciation to my supervisor Assoc. Prof. Dr. Alev Devrim Güçlü for introducing me to this exciting topic as well for the support on the way, his academic guidance and encouragement throughout this research. I am feeling grateful that I had the chance to work with my supervisor.

I would like to thank my advisor Prof. Dr. Nejat Bulut for providing and teaching the Hirsch-Fye Quantum Monte Carlo Algorithm, his academic guidance, patience and his lectures on many-body physics help me to understand many things.

I would like to thank all group mates Abdülmenaf Altıntaş, Korhan Çakmak and Bulut Kul for their help and invaluable discussions on our field. Also I would like to thank Mehmet Özcan, Utku Canbolat and Yağız Oyun for their friendship, chatting about random topics. Additionally, I would like to express my gratitude to Barış Çiçek for his patience, valuable discussions and support.

I am very grateful to Ezgi Sert who was literally always there whenever I needed help, for her patience and support. Thank you for not giving up on me throughout the path we walked together.

Eventually, I would like to express my deepest appreciation to each member of my family for their endless support.

This work was supported by The Scientific and Technological Research Council of Turkey (TUBITAK) under the 1001 Grant Project Number 114F331.

ABSTRACT

SPIN-SPIN INTERACTIONS OF MAGNETIC IMPURITIES IN GRAPHENE NANORIBBONS

In this thesis, we investigate the interaction between two impurity adatoms with high magnetic moment which are located on zigzag graphene nanoribbons that consist of 10516 atoms. The magnetic adatoms communicate with each other through the host electrons such as Ruderman-Kittel-Kasuya-Yoshida (RKKY) interactions. Firstly, in order to numerically calculate the two impurity Anderson model, we use quantum Monte Carlo technique. When the impurity adatoms are located far from edges, the results we obtained are consistent with the bulk graphene results in the literature. On the other hand, the specific location and orientation of adatoms on the sublattices, significantly affects the spin-spin correlations of the two impurities. However, we observe that while the adatoms approach to the edges, significant differences occur due to the edge effect of zigzag graphene nanoribbon. As a results of this, we found that the magnetic correlations can be also enhanced if the adatoms belong to the same sublattice as the edge atoms, since the states of the adatoms hybridize with edge states. Moreover, we show that changing chemical potential can crucially affect the magnitude of the correlations of the adatoms, and may lead to a phase transitions from ferromagnetic to antiferromagnetic or vice versa. Besides, we observe that when the width of the zigzag graphene nanoribbons is decreased, the spin-spin correlations are affected. On the other hand, we also calculated spin-spin correlations using mean-field approximation for the mean-field Anderson model. We found that results significantly differ from quantum Monte Carlo results. In addition, when the electron-electron interactions of the host atoms are taken into account, crucial differences are obtained at the impurity correlations.

ÖZET

GRAFEN NANOŞERİTLERDEKİ MANYETİK SAFSIZLIKLARIN SPİN-SPİN ETKİLEŞİMLERİ

Bu tezde, 10516 atomdan oluşan zigzag grafen nanoşeritlerin üzerinde bulunan yüksek manyetik momentli iki safsızlık adatomu arasındaki etkileşimi araştırıyoruz. Manyetik adatomlar, Ruderman-Kittel-Kasuya-Yoshida (RKKY) etkileşimleri gibi konak elektronları yoluyla birbirleriyle iletişim kuruyorlar. İlk olarak, iki safsızlık Anderson modelini sayısal olarak hesaplamak için, kuantum Monte Carlo tekniğini kullanıyoruz. Safsızlık adatomları kenarlardan uzağa yerleştirildiğinde, elde ettiğimiz sonuçlar literatürdeki yığın grafen sonuçlarıyla tutarlıdır. Öte yandan, alt örgüler üzerindeki adatomların spesifik konumu ve yönelimi, iki safsızlığın spin-spin korelasyonlarını önemli ölçüde etkiler. Bununla birlikte, adatomlar kenarlara yaklaşırken, zigzag grafen nanoribbonun kenar etkisinden dolayı önemli farklılıklar olduğunu gözlemliyoruz. Bunun bir sonucu olarak, adatomların kenar durumları ile melezleştikten, adatomların kenar atomlarıyla aynı alt örgüye ait olması durumunda manyetik korelasyonların artabileceğini bulduk. Dahası, değişen kimyasal potansiyelin, adatomların korelasyonlarının büyüklüğünü önemli ölçüde etkileyebileceğini ve ferromanyetikten antiferromanyetiğe veya tersi bir faz geçişine yol açabileceğini gösteriyoruz. Ayrıca, zigzag grafen nanoşeritlerin genişliği azaldığında, spin-spin korelasyonlarının etkilendiğini gözlemliyoruz. Diğer taraftan, ortalama alan Anderson modeli için ortalama alan yaklaşımı kullanarak spin-spin korelasyonlarını da hesapladık. Sonuçların kuantum Monte Carlo sonuçlarından önemli ölçüde farklı olduğunu bulduk. Ek olarak, konak atomların elektron-elektron etkileşimleri hesaba katıldığında, safsızlık korelasyonlarında önemli farklılıklar elde edilir.

TABLE OF CONTENTS

| | |
|---|------|
| LIST OF FIGURES | viii |
| LIST OF ABBREVIATIONS | xvi |
| CHAPTER 1. INTRODUCTION | 1 |
| CHAPTER 2. GRAPHENE | 4 |
| 2.1. Graphene..... | 4 |
| 2.2. Fabrication Techniques..... | 5 |
| 2.2.1. Mechanical Exfoliation | 5 |
| 2.2.2. Chemical Vapour Deposition | 6 |
| 2.2.3. Thermal Decomposition of <i>SiC</i> | 6 |
| 2.2.4. Bottom-up Synthesis of Graphene Nanoribbons..... | 7 |
| 2.3. Edge Effect of Graphene Nanoribbons | 8 |
| CHAPTER 3. THEORETICAL MODELS | 12 |
| 3.1. Tight Binding Model | 12 |
| 3.2. Anderson Model..... | 15 |
| 3.3. Mean-Field Hubbard Model | 17 |
| CHAPTER 4. NUMERICAL METHODS | 24 |
| 4.1. Tight-Binding..... | 24 |
| 4.2. Hirsch-Fye Quantum Monte Carlo Algorithm | 25 |
| 4.2.1. New Green's Function from the Old Green's Function | 29 |
| 4.2.2. Initial Calculation of Green's Function G^σ from G^0 and e^V | 31 |
| 4.2.3. Ratio of the Determinants..... | 33 |
| 4.2.4. Calculation of Updated Impurity Green's Function for the New Spin Field Configuration | 35 |
| 4.2.5. Quantum Monte Carlo Measurements | 36 |
| 4.3. Mean-Field approximation process for the Hubbard model | 38 |
| 4.4. Mean-Field Hubbard to Mean-Field Anderson Model | 40 |
| 4.4.1. Calculation of $\chi_{dd'}$ Solving Mean-Field Approximation | 41 |

| | |
|---|----|
| 4.5. RKKY Interaction | 44 |
| CHAPTER 5. RESULTS | 46 |
| 5.1. Results for Quantum Monte Carlo Measurements..... | 49 |
| 5.1.1. All Chains from the Middle to Edge of the ZGNR | 51 |
| 5.1.2. Torus and ZGNR | 60 |
| 5.1.3. Changing Chemical Potential $\mu \neq 0$ | 61 |
| 5.1.4. Different Width of ZGNRs | 63 |
| 5.2. Results for Mean-Field Approximation Measurements | 66 |
| 5.2.1. Results of Different Electron-Electron Interaction Values for the Host Atoms (U_{host}) | 70 |
| CHAPTER 6. CONCLUSION | 77 |
| REFERENCES | 79 |

LIST OF FIGURES

| <u>Figure</u> | <u>Page</u> |
|---|-------------|
| Figure 2.1. Schematic representation of a graphene (left) and zoom in any point on graphene to show the structure of a single carbon atom where blue orbital p_z represent the free valance electron in the z -plane, and that carbon atom connect to the other carbon atoms with sigma bonds. (Reprinted from (Guclu et al. (2014))) | 4 |
| Figure 2.2. Honeycomb lattice of graphene where marked by red is A sublattice and the other one is B sublattice, and $a_{1,2}, b$ is primitive unit vectors. (Reprinted from (Guclu et al. (2014))) | 6 |
| Figure 2.3. Thanks to the optical microscope, images of the graphene samples where single and a few layers of graphene are showed by lighter and darker regions, respectively. (Reprinted from (Exfoliation (2018))) | 7 |
| Figure 2.4. (a) Fabricated ZGNR, (b) observation of the edge states using scanning tunneling spectroscopy and (c) DFT based edge states. (Reprinted from (Ruffieux et al. (2016))) | 8 |
| Figure 2.5. Edge geometry of graphene nanoribbon. (a) zigzag edge and (b) arm-chair edge. (Reprinted from (Çakmak (2018))) | 9 |
| Figure 2.6. TB energy spectrum of different length of ZGNRs shows the degenerate states in the vicinity of the Fermi level. These ZGRNs respectively consist of (a) 36 atoms, (b) 68 atoms, (c) 132 atoms and (d) 260 atoms. . | 10 |
| Figure 2.7. Demonstration of probability distribution of highest valance band of small ZGNRs system. Upper edge totally A sublattice marked by blue one and lower edge totally B sublattice marked by red one. Also, big blue and red circle on the edges defines probability distribution of electrons. | 10 |
| Figure 2.8. (a) Representation of probability density distribution of our actual system that consists of 10516 host atoms. Width of the graphene is $W = 44$ or $4.54nm$ and (b) Just visualization of zigzag | 11 |
| Figure 3.1. Graphene band structure. Obtained from (Castro Neto et al. (2009)) | 16 |
| Figure 3.2. (a) Eigenvalues of the host electrons which was obtained from TB results. (b) Two magnetic impurities are embeded in the homogeneous host states with energy E_d . (c) Adatom state will be located above the Fermi level with energy $2E_d + U$ if the adatom state is doubly occupied. | 17 |

| | |
|---|----|
| Figure 4.1. Zigzag graphene nanoribbon consists of 36 carbon atoms | 25 |
| Figure 4.2. Feynman diagram for the impurity Green's function $G_{dd'}^0(i\omega_n)$ and $U = 0$. Double lines denote $G_{dd'}^0(i\omega_n)$ and single lines denote $g_c(i\omega_n)$ and $g_d(i\omega_n)$ for the non-interacting Green's functions. | 33 |
| Figure 4.3. Feynman diagram for the impurity Green's function with spin dependency $G_{dd'}^\sigma(i\omega_n)$. Double lines denote $G_{dd'}^\sigma(i\omega_n)$ and single lines denote $g_c(i\omega_n)$ and $g_d(i\omega_n)$ for the non-interacting Green's functions. | 42 |
| Figure 4.4. Schematic demonstration of (a) direct exchange and (b) indirect exchange. (Reprinted from the source (Ashcroft and Mermin (1976))) | 44 |
| Figure 5.1. Representation of two magnetic impurities which are randomly located on the zigzag graphene nanoribbons. | 46 |
| Figure 5.2. (a) Demonstration of ZGNR with PBC what we use in this research and consists of 10516 host atoms and it is showed middle, upper and downer edge. (b) it is zoomed in specific location on Figure (a) . (c) we focus on specific areas in middle and upper edge of the graphene and two black rectangle which are <i>Chain1</i> and <i>Chain11</i> | 47 |
| Figure 5.3. (a) Indicating of all chain we have and their first calculations are marked by red ($A_0 - A_1$). (b) Just representation of χ_{12} versus number of Chains | 48 |
| Figure 5.4. The static magnetic susceptibility between two magnetic impurities along the zigzag direction as a function of distance for the <i>AA</i> sublattice and <i>Chain1</i> which is located on the middle of ZGNRs. The solid lines are obtained by QMC simulations for different inverse temperature β . The dashed line is the RKKY results obtained from Ref.(Sherafati and Satpathy (2011b)). All results are ferromagnetic. | 49 |
| Figure 5.5. The static magnetic susceptibility between two magnetic impurities along the zigzag direction as a function of distance for the <i>BB</i> sublattice and <i>Chain1</i> which is located on the middle of ZGNRs. The solid lines are obtained by QMC simulations for different inverse temperature β . The dashed line is the RKKY results obtained from Ref.(Sherafati and Satpathy (2011b)). Also, all results show same ferromagnetic behaviour. | 50 |
| Figure 5.6. The static magnetic susceptibility between two magnetic impurities along the zigzag direction as a function of distance for the <i>AB</i> sublattice and <i>Chain1</i> which is located on the middle of ZGNRs. The solid | |

| | |
|---|----|
| lines are obtained by QMC simulations for different inverse temperature β . The dashed line is the RKKY results obtained from Ref.(Sherafati and Satpathy (2011b)). Also, all results show same antiferromagnetic behaviour. | 51 |
| Figure 5.7. The static magnetic susceptibility between two magnetic impurities along the zigzag direction as a function of distance for the <i>AA</i> sublattice. The solid lines and dashed lines are obtained by QMC simulations for the one specific inverse temperature $\beta = 16$. All results show same ferromagnetic behaviour. Also, <i>Chain1</i> and <i>Chain11</i> are located on the middle and edge of ZGNRs, respectively. | 52 |
| Figure 5.8. The static magnetic susceptibility between two magnetic impurities along the zigzag direction as a function of number of chains for the <i>AA</i> sublattice. The solid lines are obtained by QMC simulations for inverse temperature $\beta = 16$. All results show same ferromagnetic behaviour. ... | 53 |
| Figure 5.9. The static magnetic susceptibility between two magnetic impurities along the zigzag direction as a function of number of chains and specific distances for the <i>AA</i> sublattice. The solid lines and dashed lines are obtained by QMC simulations for the one specific inverse temperature $\beta = 32$. All results show same ferromagnetic behaviour. Also, <i>Chain1</i> and <i>Chain11</i> are located on the middle and edge of ZGNRs, respectively. | 54 |
| Figure 5.10. The static magnetic susceptibility between two magnetic impurities along the zigzag direction as a function of number of chains for the <i>AA</i> sublattice. The solid lines are obtained by QMC simulations for inverse temperature $\beta = 32$. All results show same ferromagnetic behaviour. ... | 56 |
| Figure 5.11. Demonstration of the energy levels of the impurities and the host atoms for (a) the <i>Chain1</i> and (b) <i>Chain11</i> | 56 |
| Figure 5.12. (a) The static magnetic susceptibility between two magnetic impurities along the zigzag direction as a function of distance for the <i>AA</i> sublattice. The solid lines and dashed lines are obtained by QMC simulations for the one specific inverse temperature $\beta = 64$. All results show same ferromagnetic behaviour. Also, <i>Chain1</i> and <i>Chain11</i> are located on the middle and edge of ZGNRs, respectively. (b) the static magnetic susceptibility as a function of number of chains. | 57 |
| Figure 5.13. The static magnetic susceptibility between two magnetic impurities | |

| | |
|---|----|
| along the zigzag direction as a function of distance for the BB sublattice. The solid lines and dashed lines are obtained by QMC simulations for the one specific inverse temperature $\beta = 32$. All results show same ferromagnetic behaviour. Also, $Chain1$ and $Chain11$ are located on the middle and edge of ZGNRs, respectively. | 58 |
| Figure 5.14. The static magnetic susceptibility between two magnetic impurities along the zigzag direction as a function of number of chains and specific distances for the BB sublattice. The solid lines and dashed lines are obtained by QMC simulations for the one specific inverse temperature $\beta = 32$. All results show same ferromagnetic behaviour. Also, $Chain1$ and $Chain11$ are located on the middle and edge of ZGNRs, respectively. | 58 |
| Figure 5.15. The static magnetic susceptibility between two magnetic impurities along the zigzag direction as a function of distance for the AB sublattice. The solid lines and dashed lines are obtained by QMC simulations for the one specific inverse temperature $\beta = 32$. All results show same ferromagnetic behaviour. Also, $Chain1$ and $Chain11$ are located on the middle and edge of ZGNRs, respectively. | 59 |
| Figure 5.16. The static magnetic susceptibility between two magnetic impurities along the zigzag direction as a function of number of chain for the AB sublattice. The solid lines and dashed lines are obtained by QMC simulations for the one specific inverse temperature $\beta = 32$. All results show same ferromagnetic behaviour. Also, $Chain1$ and $Chain11$ are located on the middle and edge of ZGNRs, respectively. | 59 |
| Figure 5.17. The static magnetic susceptibility between two magnetic impurities along the zigzag direction as a function of distance for (a) the AA sublattice. The solid lines and dashed lines are obtained by QMC simulations for the different inverse temperature β . Here, the dashed line belongs to the ZGNR and also, as known, our system has PBC. Besides, the solid lines shows Torus graphene it means that there are no any edges. So, there are no difference between both solid lines $Chain1$ and $Chain11$ when the shape of ZGNR is reshape to the Torus graphene. .. | 60 |
| Figure 5.18. The static magnetic susceptibility between two magnetic impurities along the zigzag direction as a function of distance for the AB sublattice. The solid lines and dashed lines are obtained by QMC simulations | |

for the different inverse temperature β . Here, the dashed line belongs to the ZGNR and also, as known, our system has PBC. Besides, the solid lines shows Torus graphene it means that there are no any edges. So, there are no difference between both solid lines *Chain1* and *Chain11* when the shape of ZGNR is reshape to the Torus graphene. 61

Figure 5.19. The static magnetic susceptibility between two magnetic impurities along the zigzag direction as a function of changing chemical potential μ for the *AA* sublattice shows ferromagnetic behaviour. The solid lines are obtained by QMC simulations for the inverse temperature $\beta = 32$. Also, *Chain1* and *Chain11* are located on the middle and edge of ZGNRs, respectively. 62

Figure 5.20. The static magnetic susceptibility between two magnetic impurities along the zigzag direction as a function of changing chemical potential μ for the *AB* sublattice shows antiferromagnetic behaviour. The solid lines are obtained by QMC simulations for the inverse temperature $\beta = 32$. Also, *Chain1* and *Chain11* are located in the middle and edge of ZGNRs, respectively. 63

Figure 5.21. The static magnetic susceptibility between two magnetic impurities along the zigzag direction as a function of distance for the *AA* sublattice and *Chain1* is located on the middle of ZGNRs, respectively. The solid lines are obtained by QMC simulations for the inverse temperature $\beta = 32$. Besides, each separated chains belong to different width of ZGNRs $W = 12, 20, 28, 43$ and 44 and $W = 44$ is original width of our ZGNR we used in the beginning of the research. 64

Figure 5.22. The static magnetic susceptibility between two magnetic impurities along the zigzag direction as a function of distance for the *AA* sublattice and *Chain11* is located on the edge of ZGNRs, respectively. The solid lines are obtained by QMC simulations for the inverse temperature $\beta = 32$. Besides, each separated chains belong to different width of ZGNRs $W = 12, 20, 28, 43$ and 44 and $W = 44$ is original width of our ZGNR we used in the beginning of the research. 65

Figure 5.23. The static magnetic susceptibility between two magnetic impurities along the zigzag direction as a function of distance for the *AB* sublattice and *Chain1* is located on the middle of ZGNRs, respectively. The solid lines are obtained by QMC simulations for the inverse tempera-

| | |
|--|----|
| ture $\beta = 32$. Besides, each separated chains belong to different width of ZGNRs $W = 12, 20, 28, 43$ and 44 and $W = 44$ is original width of our ZGNR we used in the beginning of the research. | 66 |
| Figure 5.24. The static magnetic susceptibility between two magnetic impurities along the zigzag direction as a function of distance for the AB sublattice and $Chain11$ is located on the edge of ZGNRs, respectively. The solid lines are obtained by QMC simulations for the inverse temperature $\beta = 32$. Besides, each separated chains belong to different width of ZGNRs $W = 12, 20, 28, 43$ and 44 and $W = 44$ is original width of our ZGNR we used in the beginning of the research. | 67 |
| Figure 5.25. The static magnetic susceptibility between two magnetic impurities along the zigzag direction as a function of distance for the AA sublattice and $Chain1$ is located on the middle of ZGNRs. The solid lines and dashed lines are obtained by QMC and MFA calculations for different inverse temperature β , respectively. All results show same ferromagnetic behaviour. (b) MFA and $Beta = 32$ calculation is zoomed and shown in the inset. | 68 |
| Figure 5.26. The magnetization of QMC results and MFA results as a function of inverse temperature for the AA sublattice, $Chain1$ and 1st adatom. The blue solid line, the black solid line and the red dashed line belong to MFA results, QMC results and curve fitting of the MFA results, respectively. | 69 |
| Figure 5.27. The static magnetic susceptibility between two magnetic impurities along the zigzag direction as a function of distance for the AA sublattice and $Chain11$ is located on the edge of ZGNRs.. The solid lines and dashed lines are obtained by QMC and MFA calculations for different inverse temperature β , respectively. All results show same ferromagnetic behaviour. | 70 |
| Figure 5.28. The magnetization of QMC results and MFA results as a function of inverse temperature for the AA sublattice, $Chain11$ and 1st adatom. The blue solid line and the black solid line belong to MFA results and QMC results, respectively. | 71 |
| Figure 5.29. The static magnetic susceptibility between two magnetic impurities along the zigzag direction as a function of distance for the AB sublattice and $Chain1$ is located on the middle of ZGNRs. . The solid | |

| | |
|--|----|
| lines and dashed lines are obtained by QMC and MFA calculations for different inverse temperature β , respectively. All results show same antiferromagnetic behaviour. | 72 |
| Figure 5.30. The static magnetic susceptibility between two magnetic impurities along the zigzag direction as a function of distance for the AB sublattice and $Chain11$ is located on the edge of ZGNRs. The solid lines and dashed lines are obtained by QMC and MFA calculations for different inverse temperature β , respectively. All results show same antiferromagnetic behaviour. | 73 |
| Figure 5.31. The static magnetic susceptibility between two magnetic impurities along the zigzag direction as a function of distance for the AA sublattice and $Chain1$ is located on the middle of ZGNR. The solid lines and dashed lines are obtained by MFA calculations for different inverse temperature $\beta = 32$ and $\beta = 128$, respectively. All results show same ferromagnetic behaviour. All calculation is done for different on-site Coulomb repulsion of the host carbon atoms taken as $U_{host} = 0, 1, 1.5$ and 2 in units of t^{-1} | 74 |
| Figure 5.32. The static magnetic susceptibility between two magnetic impurities along the zigzag direction as a function of distance for the AA sublattice and $Chain11$ is located on the edge of ZGNR. The solid lines and dashed lines are obtained by MFA calculations for different inverse temperature $\beta = 32$ and $\beta = 128$, respectively. All results show same ferromagnetic behaviour. All calculation is done for different on-site Coulomb repulsion of the host carbon atoms taken as $U_{host} = 0, 1, 1.5$ and 2 in units of t^{-1} | 75 |
| Figure 5.33. The static magnetic susceptibility between two magnetic impurities along the zigzag direction as a function of distance for the AB sublattice and $Chain11$ is located on the edge of ZGNRs. The solid lines and dashed lines are obtained by MFA calculations for different inverse temperature $\beta = 32$ and $\beta = 128$, respectively. All results show same antiferromagnetic behaviour. All calculation is done for different on-site Coulomb repulsion of the host carbon atoms taken as $U_{host} = 0, 1, 1.5$ and 2 in units of t^{-1} | 75 |
| Figure 5.34. The static magnetic susceptibility between two magnetic impurities along the zigzag direction as a function of distance for the AB sublattice and $Chain11$ is located on the edge of ZGNRs. The solid lines and dashed lines are obtained by MFA calculations for different inverse temperature $\beta = 32$ and $\beta = 128$, respectively. All results show same antiferromagnetic behaviour. All calculation is done for different on-site Coulomb repulsion of the host carbon atoms taken as $U_{host} = 0, 1, 1.5$ and 2 in units of t^{-1} | 75 |

tice and *Chain1* is located on the middle of ZGNRs. The solid lines and dashed lines are obtained by MFA calculations for different inverse temperature $\beta = 32$ and $\beta = 128$, respectively. All results show same antiferromagnetic behaviour. All calculation is done for different on-site Coulomb repulsion of the host carbon atoms taken as $U_{host} = 0, 1, 1.5$ and 2 in units of t^{-1} 76

LIST OF ABBREVIATIONS

| | |
|-------|--------------------------------|
| GNRs | Graphene Nanoribbons |
| ZGNRs | Zigzag Graphene Nanoribbons |
| TB | Tight-Binding |
| QMC | Quantum Monte Carlo |
| HFQMC | Hirsch-Fye Quantum Monte Carlo |
| MFA | Mean-Field Approximation |
| RKKY | Ruderman-Kittel-Kasuya-Yosida |
| FM | Ferromagnetic |
| AFM | Antiferromagnetic |

CHAPTER 1

INTRODUCTION

Throughout the history, people have improved themselves and learned more with conventional technology, materials and knowledge. They have kept improving themselves with increasing knowledge and science and obtained new achievements which were found accidentally or on purpose. Either way they have always served to humanity in any areas by taking themselves to the next further information.

In 2004, the extraordinary carbon based material graphene was fabricated with mechanical exfoliation by Novoselov and his group mates (Novoselov et al. (2004)). However, long before fascinating discovery, the graphene was theoretically investigated by P.R.Wallace in 1947 (Wallace (1947)) who found remarkable features such as semimetallic behaviour due to the zero energy band gap and linear dispersion relation around K and K' point by using tight-binding approach (TB). Moreover, graphene significantly differ from any semiconductor or metal due to some vital properties such as two dimensionality, linear energy dispersion, controllable chemical potential potential by applying gate voltage and the charge carriers similar to massless Dirac fermions (Novoselov et al. (2005); Castro Neto et al. (2009); Geim and Novoselov (2007)). As a consequence, the discovery of graphene led to a large number of possible applications (Geim and Novoselov (2007); Geim (2009); Castro Neto et al. (2009)). In addition to possible roles in nanoelectronics and optoelectronics, all graphene materials have also been suggested for applications in spintronics (Yazyev (2010)), such as information storage as binary code, data sharing on storage at higher speeds and communication than today's conventional electronic devices (Chappert et al. (2007); Awschalom and Flatté (2007)). The main physical idea behind spintronics is to take advantage of charge of electrons and spin with its intrinsic angular momentum.

On the other hand, graphene's lack of a bandgap limits possible application areas. One way of dealing with this problem is to reduce the size of the graphene to the nanoscale. This comes with additional striking effects. Particularly, the electronic and magnetic properties start to depend on its geometric shape by breaking sublattice symmetry of graphene along a direction (Han et al. (2007); Yang et al. (2007)). Two edge terminated graphene nanoribbons which can be armchair or zigzag edged show a band gap due to breaking sublattice symmetry at the edges and have been theoretically shown

many times (Son et al. (2006); Jung et al. (2009); Jung and MacDonald (2009)). On the other hand, zigzag graphene nanoribbons is theoretically expected to have ferromagnetically spin polarization within each edges and antiferromagnetically coupled edges according to the Lieb's theorem (Lieb (1989)) for a bipartite lattice. Moreover, zigzag graphene nanoribbons have been experimentally produced by using the bottom-up approaching and some research group show that narrow, long and disorder ZGNRs can be fabricated (Kilmouche et al. (2015); Ruffieux et al. (2016)). Besides, thanks to relation between bandgap and width of narrow nanoribbon, magnetic phase transition can be indirectly observed (Magda et al. (2014)). These results promise for the graphene based spintronic devices.

Another possible process of graphene based spintronics is occurrence of disorders that arise in graphene. This may lead to magnetism (Yazyev and Helm (2007)), despite the fact that carbon atom of graphene is not magnetic. Indeed, the magnetism in graphene is not caused by d or f orbitals of any impurity. So, magnetism is occurred by breaking sublattice symmetry with small zigzag edge domains and started to form around vacancy (Palacios et al. (2008); Zhang et al. (2016)).

Another striking way for using graphene in spintronic applications, is to dope of graphene with magnetic impurities. However, in this condition, graphene is acting as host for these transition metal atoms unlike two previous approaches (reducing the size of graphene and creating vacancy). Moreover, graphene host electrons mediate interactions in order to transfer spin information between the impurities. Besides, the interaction strongly depends on the electronic structure of the host atoms. This is the indirect exchange interaction also known as Ruderman-Kittel-Kasuya-Yosida (RKKY) interaction (Ruderman and Kittel (1954); Kasuya (1956); Yosida (1957)). This type of interaction should oscillate and decay as a function of distance between the two impurities. In addition to that, the oscillations are defined by the Fermi surface of the host atoms, and decay power of interaction depends on dimension of the host material. Namely, RKKY interaction should be expected to decay as R^{-3} in the graphene (Wunsch et al. (2006)) where R is the distance between the two impurities unlike the behaviour of a two dimensional electron gas where the decay goes as R^{-2} (Fischer and Klein (1975)). A recent work by Ref.(Guclu and Bulut (2015)) shows that full treatment of spin correlations about magnetic adatoms on graphene significantly differ from the RKKY model in bulk graphene.

In this thesis, we consider the zigzag graphene nanoribbons that has zero energy edge states at Fermi level unlike armchair edges that has no such specific states (Fujita et al. (1996); Nakada et al. (1996)). Because of that, spin-spin interactions of magnetic impurities in zigzag graphene nanoribbons with periodic boundary conditions are stud-

ied using the two impurity Anderson model. Due to the edge states in the ZGNRs, the magnetic properties of two impurities could lead to new behaviours which are different from the bulk graphene or metallic system results in the literature. To examine deeply and broaden horizons on this topic, mean-field Anderson model are introduced in order to make comparison between the mean-field Anderson model and the two-impurity Anderson model. Moreover, in the MF Anderson model, electron-electron interactions taken into account for the host electrons could lead to vital results.

CHAPTER 2

GRAPHENE

In this chapter, we will briefly explain graphene and its lattice structure. Then, several fabrication techniques of graphene nanostructures will be described. Particularly, thanks to a specific method, ZGNRs with edge sites are experimentally fabricated. Because of that, we will theoretically focus on finite ZGNRs and distinctly examine its edge effect.

2.1. Graphene

A single carbon atom has 6 electrons in the $1s^2, 2s^1$ and $2p^3$ orbitals. Moreover, there are 2 paired electrons in the $1s^2$ orbital. Carbon atom has 4 valance electrons. In graphene, three unpaired electrons occupy $2s^1, 2p_x^1$ and $2p_y^1$ orbitals that make sp^2 bonds with surrounding atoms or carbon atoms as seen in the Fig.(2.1). Furthermore, these three bonds are responsible for mechanical properties of graphene. The last electron fills the last $2p_z$ orbital that is perpendicular to surface and forms π bonds as seen in the Fig.(2.1). In addition, this electron that moves freely contributes to electronic properties of graphene.

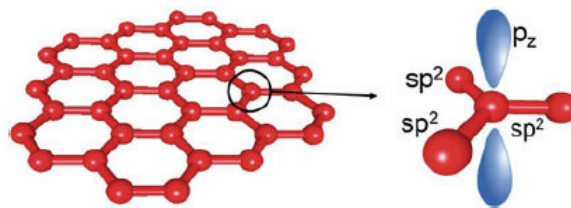


Figure 2.1. Schematic representation of a graphene (left) and zoom in any point on graphene to show the structure of a single carbon atom where blue orbital p_z represent the free valance electron in the z -plane, and that carbon atom connect to the other carbon atoms with sigma bonds. (Reprinted from (Guclu et al. (2014)))

In the following, the lattice of graphene that is honeycomb with lattice constant $a = 0.142nm$ between two carbon atoms consists of two different sublattices which are

A sublattice marked by red one and B sublattice marked by blue as seen in the Fig.(2.2). So, positions of all A and B carbon atoms can be found by using the following equation,

$$\mathbf{R}_A = n\mathbf{a}_1 + m\mathbf{a}_2 + \mathbf{b} \quad (2.1)$$

$$\mathbf{R}_B = n\mathbf{a}_1 + m\mathbf{a}_2 \quad (2.2)$$

where n and m are integers, \mathbf{b} is a vector between A and B carbon atom and $a_{1,2}$ is the lattice vector,

$$\mathbf{a}_1 = \frac{a}{2}(\sqrt{3}, 3), \mathbf{a}_2 = \frac{a}{2}(-\sqrt{3}, 3) \quad \text{and} \quad \mathbf{b} = a(0, 1) \quad (2.3)$$

Before discovering existence of graphene, the electronic structure of graphene was theoretically investigated by P.R.Wallace in 1947 (Wallace (1947)). Wallace made two major assumptions. One of them is that when space between graphene layers in graphite is enlarged, this large space may lead to confine electrons that move only in the graphene plane. The other one is that electronic properties of graphene can be described by only using $2p_z$ orbital within tight-binding approximation. Moreover, in the sec.(4.1), we will see tight-binding methods for the finite system and examine all process in detail. In the next section, a few experimental techniques will be examined in order to fabricate finite graphene and graphene nanoribbon structures.

2.2. Fabrication Techniques

In this section, several production ways are described in order to fabricate graphene and graphene nanoribbon samples. A few production methods are presented. Moreover, a recent fabrication method that produced ZGNRs is briefly explained.

2.2.1. Mechanical Exfoliation

Exfoliation of graphene is the first and basic method in order to acquire the graphene by brute force. This method, also known as "Scotch Tape Method", was used by Novoselov, Geim and their group in 2004, (Novoselov et al. (2004)). On the other hand, graphite con-

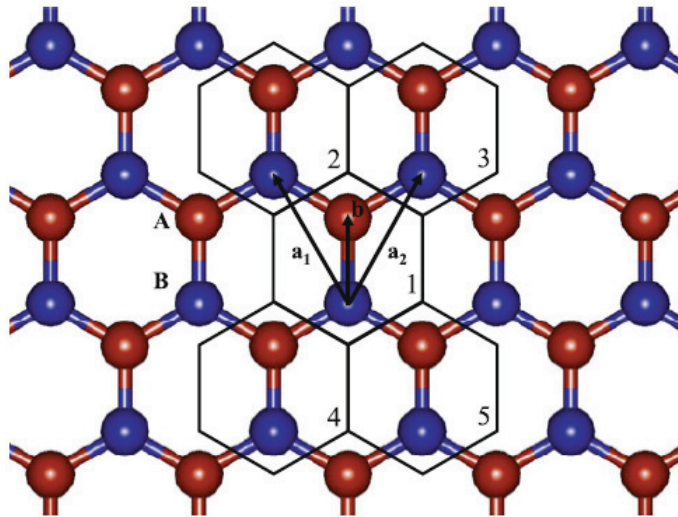


Figure 2.2. Honeycomb lattice of graphene where marked by red is A sublattice and the other one is B sublattice, and $a_{1,2}$, b is primitive unit vectors. (Reprinted from (Guclu et al. (2014)))

sists of a hundreds of single layers of graphene that are bounded to each other by weak van der Waals forces. Furthermore, a piece of graphite is sticked to a scotch tape and thanks to the adhesive force of the tape, peeling the tape off leaves a few graphite. Then, this process is applied over and over again. So, layers of graphite is separated from each other by breaking the these bonds in order to get single layer graphite. After that, the graphene should be transferred to a substrate such as SiO_2 . Namely, the tape is pressed on the substrate and peeled off.

2.2.2. Chemical Vapour Deposition

One of the most commonly used method is CVD in order to obtain the synthesis of high quality graphene which contains controlled number of layers in a wide area or single layer of graphene. In this method, two mainly different transition metal films are used such as Copper (Cu) and Nickel (Ni). So, main point is that one can get a single layer graphene by using Cu (Yan et al. (2012)). On the other hand, the other method is used to achieve controllable growth of graphene layer that depends on changing nickel thickness or growth time. After that, obtained graphene can be transferred to arbitrary substance (Reina et al. (2009)). Thus, using different transition metal affects quality, efficiency of graphene.

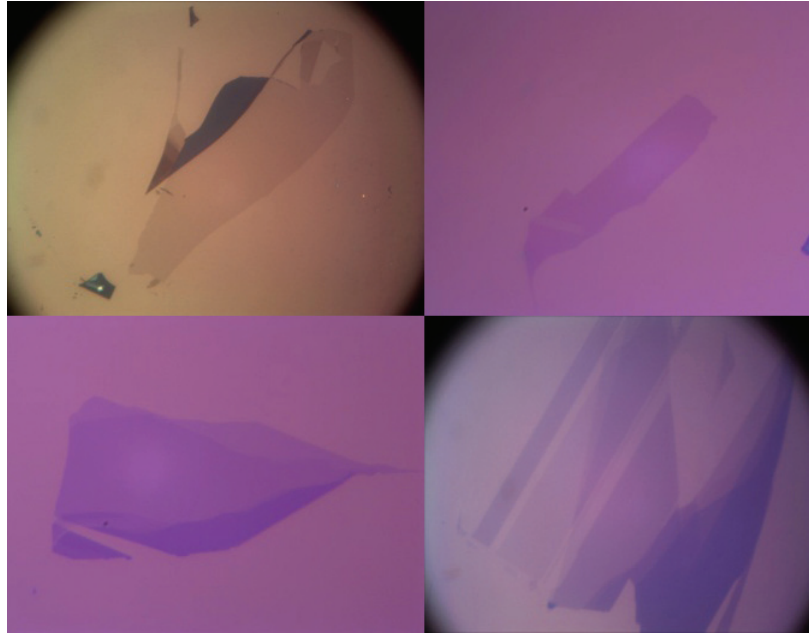


Figure 2.3. Thanks to the optical microscope, images of the graphene samples where single and a few layers of graphene are showed by lighter and darker regions, respectively. (Reprinted from (Exfoliation (2018)))

2.2.3. Thermal Decomposition of *SiC*

Another approach is thermal decomposition of *SiC* to epitaxially grow single layer of graphene directly on *SiC* substrate (Berger et al. (2004, 2006)). This substrate has same hexagonal lattice structure like graphene and is heated. Then, temperature of the substrate is increased up to 1100°C in order to break *Si* bonds from surface. After that, surface carbon atoms rebind to each other to obtain shape of monolayer or multilayers of graphene (Hass et al. (2008)). Moreover, quantity of the graphene can be controlled on *SiC*. Also, using of this technique is to give a chance to obtain different forms like nanoribbons and quantum dots (Tapasztó et al. (2008); Sprinkle et al. (2010); Palacio et al. (2015)).

2.2.4. Bottom-up Synthesis of Graphene Nanoribbons

A few techniques have been performed in order to successfully obtain the graphene nanostructures. Furthermore, one of them is bottom-up method (Cai et al. (2010, 2014);

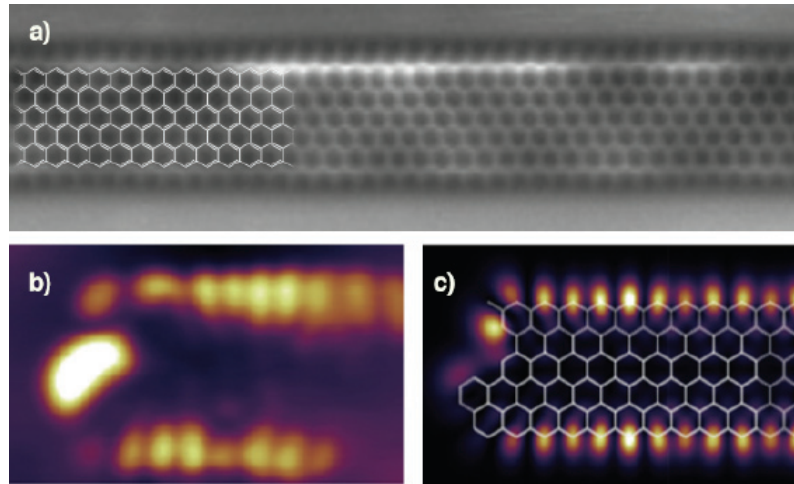


Figure 2.4. (a) Fabricated ZGNR, (b) observation of the edge states using scanning tunneling spectroscopy and (c) DFT based edge states. (Reprinted from (Ruffieux et al. (2016)))

Massimi et al. (2015); Ruffieux et al. (2016); Smerieri et al. (2016)). This method shows perfect edge sites (Ruffieux et al. (2016)) and is consistent with theoretical results (Nakada et al. (1996)) unlike top-down approach which failed due to the limited precision (Han et al. (2007); Li et al. (2008); Magda et al. (2014); Kosynkin et al. (2009); Wang and Dai (2010); Ma et al. (2013)). The bottom-up method is based on surface assisted polymerization with catalysed cyclodehydrogenation of U shaped monomer. This method atomically produces precise zigzag edges on $Au(111)$ substrate. As a results of this, as shown in the Fig.(2.4), edge states with ultra-narrow nanoribbons is successfully fabricated and observed by using scanning tunneling spectroscopy (Ruffieux et al. (2016); Kimouche et al. (2015)).

2.3. Edge Effect of Graphene Nanoribbons

In this section, we will explain that zigzag edged graphene nanoribbons is so vital for this research on the contrary armchair edged graphene nanoribbons. Moreover, we will show differences between distinct samples of ZGNRs. As we have mentioned before, we work on finite size of zigzag graphene nanoribbons with periodic boundary condition. First of all, we have two vectors which scans every each atom one by one on bulk graphene. Acceptable atoms are picked if each scanned atom provides our conditions

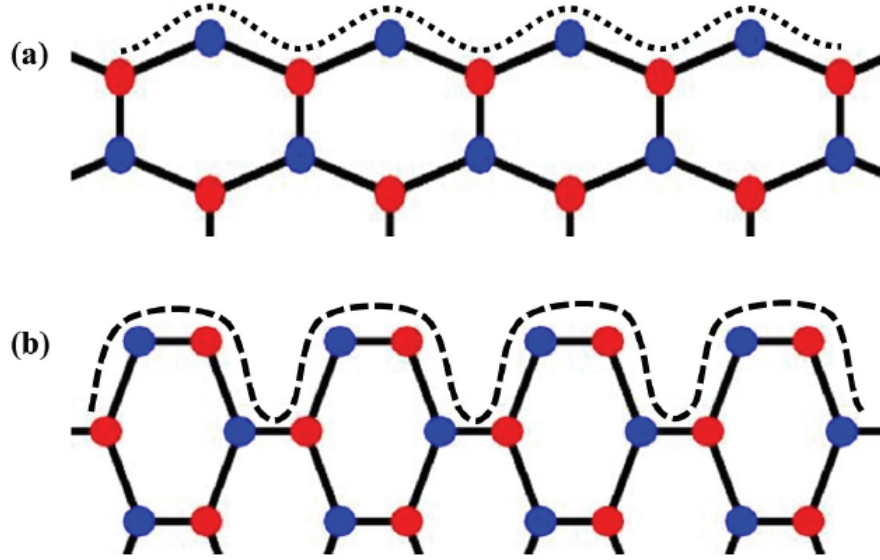


Figure 2.5. Edge geometry of graphene nanoribbon. **(a)** zigzag edge and **(b)** armchair edge. (Reprinted from (Çakmak (2018)))

which are defined by cutting axis. Also, according to the cutting axis conditions, we can obtain any shape of graphene system like zigzag or armchair edged graphene nanoribbons as can be seen in the Fig.(2.5). Moreover, these two edge patterns has a crucial role on electronic property of nanostructure. On the other hand, edge terminations of graphene nanoribbon have extra unpaired electrons per carbon atoms. In this thesis, we assume that all these sites are doped by hydrogen atoms. Namely, we make the edge passivation with the hydrogen atoms because hydrogen atom has only one unpaired electron on $1S$ state.

On the other hand, we need to narrow the subject to the specific shape of edges and let us begin with zigzag edges. After diagonalizing TB Hamiltonian, TB energy spectrum of ZGNRs is obtained for small different systems as seen in the Fig.(2.6). Also, zero energy states known as edge states are shown in the energy spectrum around the Fermi level due to broken sublattice symmetry (Castro Neto et al. (2009); Guclu et al. (2014); Nakada et al. (1996); Çakmak (2018); Özdemir (2016); Güçlü et al. (2013)). Moreover, armchair GNRs has no such these states. Furthermore, these edge states are increased with length of ZGNRs. Also, width of ZGNRs is same in all shown examples. Additionally, absence or presence of the edge states depend on sublattice symmetry, size and edge geometry shape and contribute undeniable extraordinary feature to the electronic properties of GNRs (Guclu et al. (2014)). As seen in the Fig.(2.7), we have probability

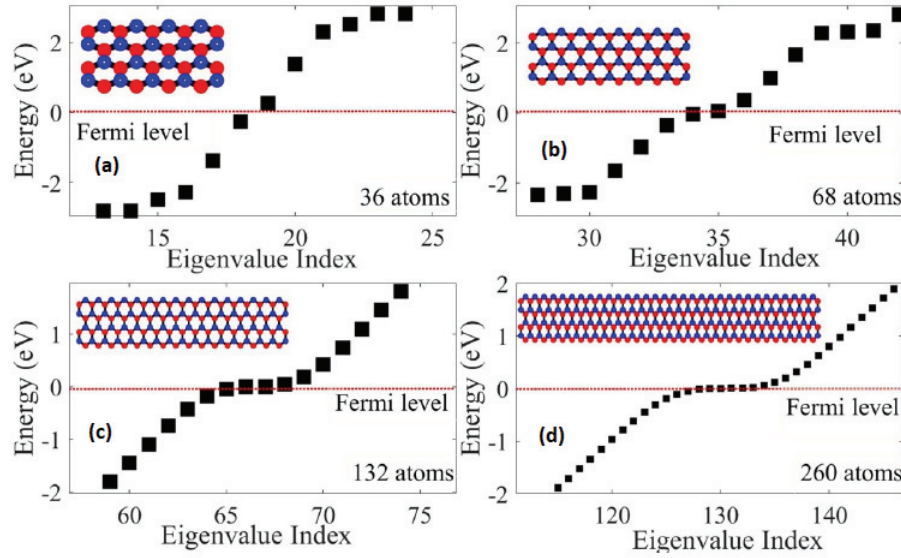


Figure 2.6. TB energy spectrum of different length of ZGNRs shows the degenerate states in the vicinity of the Fermi level. These ZGRNs respectively consist of **(a)** 36 atoms, **(b)** 68 atoms, **(c)** 132 atoms and **(d)** 260 atoms.

distribution of the highest valance state of the system. As we have known before, the graphene consists of two sublattices that are A marked by blue and B marked by red in the Fig.(2.7). Now, we focus on upper-half part of the graphene and go to top of the graphene. This probability distribution just spreads through the A sublattice. When looking at lower-half of the graphene, same spreading occurs there for the B sublattice. This feature unexpectedly affects our results. Moreover, we will discuss this effect in detail in the results chapter.

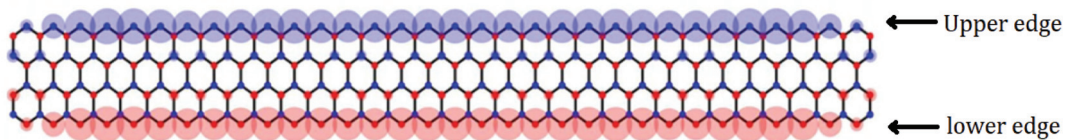


Figure 2.7. Demonstration of probability distribution of highest valance band of small ZGNRs system. Upper edge totally A sublattice marked by blue one and lower edge totally B sublattice marked by red one. Also, big blue and red circle on the edges defines probability distribution of electrons.

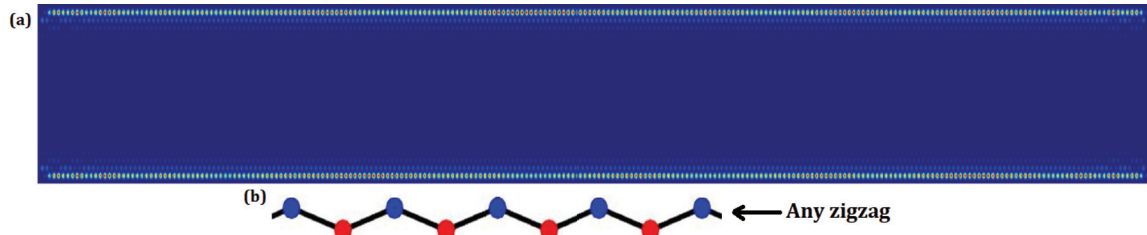


Figure 2.8. **(a)** Representation of probability density distribution of our actual system that consists of 10516 host atoms. Width of the graphene is $W = 44$ or $4.54nm$ and **(b)** Just visualization of zigzag

As shown in Fig.(2.8), the probability density of real system that we work on is indicated for the highest valance band of ZGRNs. According to the figure, the density of electrons are accumulated on the upper and lower edge sites. Then, they are spread from these edges to middle of the graphene like in the Fig.(2.7). However, this spreading effect is decreased until specific point unlike the Fig.(2.7), due to width of graphene. Consequently, the real system consist of 10516 host atoms with length of $58.66nm$ and width of $4.54nm$. On the other hand, as seen in the Fig.(2.7)(b), this is just one zigzag. So, there are 22 zigzag ($W = 44$).

CHAPTER 3

THEORETICAL MODELS

During this research, we investigated spin-spin correlation between two impurities. These two adatoms are attached to the graphene that is our host. In order to explain the physical fact and get correct results, we have employed some theoretical models which are tight-binding, two-impurity Anderson, mean-field Hubbard model. These models assist us to understand physics behind main event. Now, starting with defining Tight-Binding model in the following section.

3.1. Tight Binding Model

The tight-binding model is not only a basic, easier and accurate but also lower computational cost unlike mean-field approximation which we will examine in two next section. Roughly speaking, thanks to its low computational cost, one can simply simulate a system which may consist of ten thousand atoms and may be carbon based material such as graphene. Despite the fact that the simplest model for graphene is comparatively accurate, there is no spin dependence terms

To start from atomic limit by writing crystal Hamiltonian for an electron. It can be written as

$$H = H_{atomic} + \Delta U(\vec{r}) \quad (3.1)$$

where $\Delta U(\vec{r})$ periodic potential due to crystal structure. The periodic potential comes from all other atoms. We can write atomic wave function down,

$$H \psi_n = E_n \psi_n \quad (3.2)$$

where ψ is an eigenstate of Hamiltonian and E_n is atomic energy. One assumes Bloch wavefunction that assures periodicity of the lattice as

$$\psi_{nk}(\vec{r}) = \sum_R e^{i\vec{k}\cdot\vec{R}} \phi_n(\vec{r} - \vec{R}) \quad (3.3)$$

where ϕ_n is a molecular orbital and called Wannier function that is not an exact eigenstate of H_{atomic} . The Wannier functions can be expressed as Linear combination of atomic orbitals (LCAO) which is to approach to make a trial solution in the wavefunction and can be defined as

$$\phi_n(\vec{r} - \vec{R}) = \sum_n b_n \varphi_n(\vec{r} - \vec{R}) \quad (3.4)$$

where φ_n is atomic orbital. Each of them is multiplied by corresponding coefficient b_n . Now, one applies that Bloch's wavefunction defined by Eq.3.3 is substituted into Hamiltonian in Eq.3.2 because solution of Schrödinger equation must obey the Bloch's theorem,

$$H\psi_k(\vec{r}) = (H_{atomic} + \Delta U(\vec{r})) \psi_k(\vec{r}) = \varepsilon_k \psi_k(\vec{r}) \quad (3.5)$$

and one multiplies both side by $\int d^3r \varphi_m^*(\vec{r})$

$$\begin{aligned} \varepsilon_k \int d^3r \varphi_m^*(\vec{r}) \psi_k(\vec{r}) &= \underbrace{\int d^3r \varphi_m^*(\vec{r}) H_{atomic} \psi_k(\vec{r})}_{E_m \int d^3r \varphi_m^*(\vec{r}) \psi_k(\vec{r})} \\ &+ \int d^3r \varphi_m^*(\vec{r}) \Delta U(\vec{r}) \psi_k(\vec{r}) \end{aligned} \quad (3.6)$$

$$(\varepsilon_k - E_m) \int d^3r \varphi_m^*(\vec{r}) \psi_k(\vec{r}) = \int d^3r \varphi_m^*(\vec{r}) \Delta U(\vec{r}) \psi_k(\vec{r}) \quad (3.7)$$

one will substitute Eq.3.3 into Eq.3.7.

$$(\varepsilon_k - E_m) \int d^3r \varphi_m^*(\vec{r}) \sum_{R,n} b_n e^{i\vec{k}\cdot\vec{R}} \varphi_n(\vec{r} - \vec{R}) \quad (3.8)$$

$$= \int d^3r \varphi_m^*(\vec{r}) \Delta U(\vec{r}) \sum_{R,n} b_n e^{i\vec{k}\cdot\vec{R}} \varphi_n(\vec{r} - \vec{R}) \quad (3.9)$$

one will examine series over R summation in two different values which are $R = 0$ and $R \neq 0$

$$\begin{aligned}
& (\varepsilon_k - E_m) \underbrace{\sum_n b_n}_{b_m} \int d^3r \underbrace{\varphi_m^*(\vec{r}) \varphi_n(\vec{r})}_{\delta_{mn}} \underbrace{e^{i\vec{k}\cdot\vec{R}}}_{=1} \\
& + (\varepsilon_k - E_m) \sum_n b_n \left(\sum_{R \neq 0} e^{i\vec{k}\cdot\vec{R}} \underbrace{\int d^3r \varphi_m^*(\vec{r}) \varphi_n(\vec{r} - \vec{R})}_{\alpha(\vec{R})} \right) \quad (3.10)
\end{aligned}$$

$$\begin{aligned}
& = \sum_n b_n \underbrace{\int d^3r \varphi_m^*(\vec{r}) \Delta U(\vec{r}) \varphi_n(\vec{r})}_{-\beta} \\
& + \sum_n \left(\sum_{R \neq 0} e^{i\vec{k}\cdot\vec{R}} \underbrace{\int d^3r \varphi_m^*(\vec{r}) \Delta U(\vec{r}) \varphi_n(\vec{r} - \vec{R})}_{\gamma(\vec{R})} \right) \quad (3.11)
\end{aligned}$$

where $\alpha(\vec{R})$ is overlap integral and small term. Because of that we can ignore that term. Second term is β that is independent of k and energy shifting due to potential of the surrounding atoms. last term is $\gamma(\vec{R})$ that is mostly called as hopping integral and gives the energy interaction between different atoms. Graphene consists of two different sublattices. Each carbon atom in infinite graphene lattice has three opposite neighbouring atoms as seen in the Fig.(2.2). So, electron of each carbon atom sites feels potential (ΔU) of other atoms at its lattice. Because of that, electron are hopping next nearest neighbour due to screening effect.

$$\gamma(\vec{R}) = - \int d^3r \varphi_m^*(\vec{r}) \Delta U(\vec{r}) \varphi_n(\vec{r} - \vec{R}) \equiv t \quad (3.12)$$

Here, γ is the hopping integral. So, electron located at $\vec{r} - \vec{R}$ position is hopping to second site located position at \vec{r} or vice versa. Therefore, t is call as hopping parameter and depends on related material type. Also, this parameter is usually taken for the graphene as $t = -2.8eV$ (Castro Neto et al. (2009)). As a consequently of this, above Eq.(3.10) and (3.11) turn into the following,

$$(\varepsilon_k - E_m + \beta)b_m = \sum_{R \neq 0} e^{i\vec{k}\cdot\vec{R}} \gamma(\vec{R}) \quad (3.13)$$

where E_m and β will only result in a physical difference in the eigenvalues. So, we can ignore this energy (Ashcroft and Mermin (1976)),

$$\varepsilon_k b_m = t \sum_{R \neq 0} e^{i\vec{k} \cdot \vec{R}} \quad (3.14)$$

the above equation was found for any material. Thus, we need to use this equation for graphene. As a results of this, we can know that three nearest neighbour atom's vectors which are $\vec{a}_1 = \frac{a}{\sqrt{3}}\hat{i}$, $\vec{a}_2 = \frac{a}{\sqrt{3}}(\frac{-1}{2}\hat{i} + \frac{3}{2}\hat{j})$, $\vec{a}_3 = \frac{a}{\sqrt{3}}(\frac{-1}{2}\hat{i} - \frac{3}{2}\hat{j})$. After summation over all nearest neighbours, the following equation is defined,

$$f(k) = t(e^{i\vec{k} \cdot \vec{a}_1} + e^{i\vec{k} \cdot \vec{a}_2} + e^{i\vec{k} \cdot \vec{a}_3}) \quad (3.15)$$

$$f^*(k) = t(e^{-i\vec{k} \cdot \vec{a}_1} + e^{-i\vec{k} \cdot \vec{a}_2} + e^{-i\vec{k} \cdot \vec{a}_3}) \quad (3.16)$$

turning into eigenvalue equation in matrix form,

$$\varepsilon_k \begin{pmatrix} b_0 \\ b_1 \end{pmatrix} = \begin{pmatrix} 0 & tf(k) \\ tf^*(k) & 0 \end{pmatrix} \begin{pmatrix} b_0 \\ b_1 \end{pmatrix} \quad (3.17)$$

Hence, solution of the system,

$$\varepsilon_{\pm}(k) = \pm |tf(k)| \quad (3.18)$$

According to the obtained energy states for the bulk graphene as seen in the Fig.(3.1), we obtain two distinct energy levels which are valance band ($\varepsilon(k) < 0$) and conduction band ($\varepsilon(k) > 0$). Also, they are symmetric with respect to the fermi level ($\varepsilon(k) = 0$)

As a result of this, all above calculation was done for the bulk graphene in the momentum space. However, during this research, we did all calculations which are tight-binding model and mean-field Anderson model in real space. Namely, working in the real space gives us some advantages such as easily adding adatom, vacancy, potential or controlling each atoms. In the next section, Anderson model will be introduced for the HFQMC Algorithm.

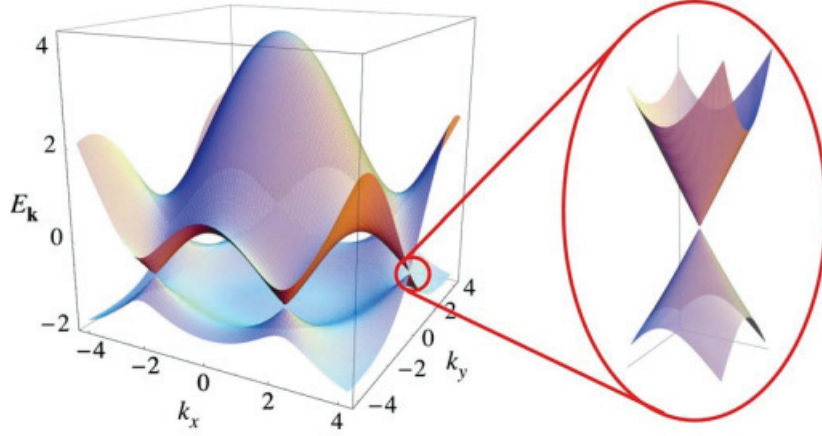


Figure 3.1. Graphene band structure. Obtained from (Castro Neto et al. (2009))

3.2. Anderson Model

Two magnetic impurities which interact with each other as RKKY are embedded in a homogenous host as can be seen in the Fig.(3.2). Firstly, one impurity system was described by Anderson (Anderson (1961)). The Anderson model gives us information about electronic and magnetic structure of transition metal impurities in the host material. In this thesis, the two impurities Anderson model for the ZGNRs is studied and given by,

$$\begin{aligned}
 H = & t \sum_{\langle i,j \rangle} c_{i\sigma}^\dagger c_{j\sigma} + \sum_{i,\sigma} (E_d - \mu) d_{i\sigma}^\dagger d_{i\sigma} \\
 & + \sum_{i,j,\sigma} (V_{ij} c_{i\sigma}^\dagger d_{j\sigma} + h.c.) + U \sum_i n_{id\uparrow} n_{id\downarrow}
 \end{aligned} \tag{3.19}$$

where t is hopping parameter of the host electrons, $c_{i\sigma}^\dagger$ ($c_{j\sigma}$) creates (annihilates) a host electron with spin σ , E_d is the impurity energy level, $d_{i\sigma}^\dagger$ ($d_{i\sigma}$) is creation (annihilation) operator at site i for the impurity electrons, V_{ij} is the hybridization between host and impurity electron, U term is the on-site Coulomb interaction for the d electrons and $n_{id\sigma} = d_{i\sigma}^\dagger d_{i\sigma}$ is the number operator for the impurity electrons.

Transition metal impurity has half-filled or partially-filled of d or f orbital. Therefore, electron exchanging only between impurity and host depends on state occupied by only one electron or doubly occupied by two electrons. So, there is no magnetization if

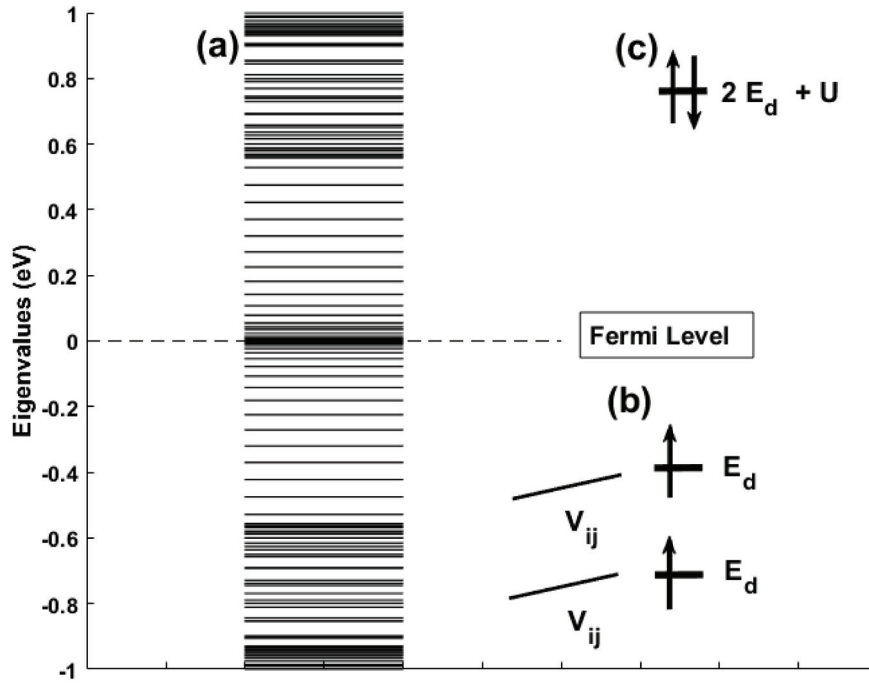


Figure 3.2. (a) Eigenvalues of the host electrons which was obtained from TB results. (b) Two magnetic impurities are embeded in the homogeneous host states with energy E_d . (c) Adatom state will be located above the Fermi level with energy $2E_d + U$ if the adatom state is doubly occupied.

state is occupied by two electrons as shown in the Fig.(3.2). On the other hand, d or f states of transition metal that are unoccupied states is not allowed to communicate with each other. As a results of this, it is very hard to solve the Eq.(3.19) with on-site Coulomb term. Because of that, we will employ Hirsch-Fye quantum Monte Carlo (HFQMC) which is explained in the next chapter in order to solve the two impurity Anderson model, numerically. In the next section, we will derive mean-field Hubbard model.

3.3. Mean-Field Hubbard Model

In this section, another realistic approaching model will be discussed in order to comprehend magnetism and electronic structure of correlated materials unlike TB model that has no spin dependency. Hubbard model which was first proposed by J. Hubbard in 1963 (Hubbard and Flowers (1963)) gives us a chance to realize physical picture of mag-

netism with spin dependency σ . On the other hand, the Hubbard model is exactly solvable in one dimension which is 1D Ising model and was solved by E. Ising (Ising (1925)). Besides, two-dimensional Ising model was solved by L. Onsager (Onsager (1944)). So, basic system can be exactly solved without any approximation. As a consequence of this, we should employ approximation method that is known as Weiss mean-field theory in order to numerically solve unsolvable model. Therefore, many-body problem is reduced to one body problem by adding mean-field method. This method presumes that each electron feels an average interactions that comes from all others.

To begin with defining the system and its Hamiltonian which consisting of kinetic energy of electrons and their electron-electron interactions,

$$H = \sum_{i=1}^N \left(-\frac{\hbar^2}{2m} \nabla_i^2 \right) + \frac{1}{2} \sum_{\substack{i,j \\ i \neq j}} V_{ee}(r_i - r_j) \quad (3.20)$$

The Hamiltonian with field operators in second quantization,

$$H = \sum_{\sigma} \int d^3r \Psi_{\sigma}^{\dagger}(r) \left(-\frac{\hbar^2}{2m} \nabla^2 \right) \Psi_{\sigma}(r) \quad (3.21)$$

$$+ \frac{1}{2} \sum_{\sigma\sigma'} \int \int d^3r d^3r' \Psi_{\sigma}^{\dagger}(r) \Psi_{\sigma'}^{\dagger}(r') V_{ee}(r - r') \Psi_{\sigma'}(r') \Psi_{\sigma}(r) \quad (3.22)$$

where $\Psi_{\sigma}(r)$ is field operator,

$$\Psi_{\sigma}(r) = \sum_i \varphi_i(r) c_{i,\sigma} \quad (3.23)$$

After the above definitions, the many-body Hamiltonian in second quantization form was obtained,

$$H = \sum_{pq} t_{pq} c_p^{\dagger} c_q + \frac{1}{2} \sum_{pqrs} \langle pq|V|rs \rangle c_p^{\dagger} c_q^{\dagger} c_r c_s \quad (3.24)$$

where p, q, r and s are $i\sigma, j\sigma', k\sigma''$ and $l\sigma'''$, respectively. $\sigma = \uparrow / \downarrow$ is the spin of electrons. On the other hand, $\frac{1}{2}$ is double counting of interactions in front of second term of the Eq.3.24. Because of that, one must divide second term by 2.

$$t_{pq} = \langle p|t|q \rangle = \langle i\sigma|t|j\sigma' \rangle = \langle i|t|j \rangle \underbrace{\langle \sigma|\sigma' \rangle}_{\delta_{\sigma\sigma'}} = t_{ij}\delta_{\sigma\sigma'} \quad (3.25)$$

now, one will apply same thing for the second term in the Eq.3.24,

$$V_{pqrs} = \frac{1}{2} \sum_{pqrs} \langle pq|V|rs \rangle c_p^\dagger c_q^\dagger c_r c_s \quad (3.26)$$

$$= \frac{1}{2} \sum_{ijkl} \langle i\sigma j\sigma' |V|k\sigma'' l\sigma''' \rangle c_{i\sigma}^\dagger c_{j\sigma'}^\dagger c_{k\sigma''} c_{l\sigma'''} \quad (3.27)$$

$$= \frac{1}{2} \sum_{ijkl} \langle ij|V|kl \rangle c_{i\sigma}^\dagger c_{j\sigma'}^\dagger c_{k\sigma''} c_{l\sigma'''} \underbrace{\langle \sigma|\sigma''' \rangle}_{\delta_{\sigma\sigma'''}} \underbrace{\langle \sigma'|\sigma'' \rangle}_{\delta_{\sigma'\sigma''}} \quad (3.28)$$

Eventually, Eq.3.24 can be written as,

$$H = \sum_{\langle ij \rangle_\sigma} t_{ij} c_{i\sigma}^\dagger c_{j\sigma} + \frac{1}{2} \sum_{ijkl} \langle ij|V|kl \rangle c_{i\sigma}^\dagger c_{j\sigma'}^\dagger c_{k\sigma'} c_{l\sigma} \quad (3.29)$$

Now, one should consider two things which are $\langle ii|V|ii \rangle = U$ and $\langle ji|V|ij \rangle = V_{ij}$ about second term of Eq.3.29. Then, one will discuss them and their consequences. $\langle ii|V|ii \rangle = U$ means on-site Coulomb interaction term. Thus, $i = j = k = l$ and second term turn into following form,

$$\frac{1}{2} \sum_{ijkl} \langle ij|V|kl \rangle c_{i\sigma}^\dagger c_{j\sigma'}^\dagger c_{k\sigma'} c_{l\sigma} = \frac{1}{2} \sum_{i\sigma\sigma'} U c_{i\sigma}^\dagger c_{i\sigma'}^\dagger c_{i\sigma'} c_{i\sigma} \quad (3.30)$$

According to the Pauli exclusion principle, two identical fermions can not occupy same site i . So, σ and σ' ($\sigma \neq \sigma'$) must be different from each other. Also, one needs to firstly define commutation relations in order to use these properties which are $\{c_{i\sigma}, c_{j\sigma'}\} = 0$, $\{c_{i\sigma}^\dagger, c_{j\sigma'}^\dagger\} = 0$ and $\{c_{j\sigma'}^\dagger, c_{i\sigma}\} = \delta_{i,j} \delta_{\sigma\sigma'}$. Now, one will use commutation relations and expand the spin terms. So, one has two different configurations which are $\sigma = \uparrow, \sigma' = \downarrow$ or $\sigma = \downarrow, \sigma' = \uparrow$ for Eq.3.30. Thus, Eq.3.30 becomes,

$$\frac{U}{2} \sum_i \left(\underbrace{c_{i\uparrow}^\dagger c_{i\uparrow} c_{i\downarrow}^\dagger c_{i\downarrow}}_{n_{i\uparrow}} + \underbrace{c_{i\downarrow}^\dagger c_{i\downarrow} c_{i\uparrow}^\dagger c_{i\uparrow}}_{n_{i\downarrow}} \right) = U \sum_i n_{i\uparrow} n_{i\downarrow} \quad (3.31)$$

Similarly, for off-site repulsion term,

$$\langle ji|V|ij\rangle = V_{ij} \quad \text{and} \quad \frac{1}{2} \sum_{\substack{i \neq j \\ \sigma \sigma'}} \langle ji|V|ij\rangle c_{i\sigma}^\dagger c_{j\sigma'}^\dagger c_{j\sigma'} c_{i\sigma} \quad (3.32)$$

Thanks to the commutation relations $\{c_{i\sigma}, c_{j\sigma'}\} = 0$ and $\{c_{j\sigma'}^\dagger, c_{i\sigma}\} = \delta_{i,j} \delta_{\sigma\sigma'}$, one needs to rearrange operator order by swapping with each other one by one,

$$\begin{aligned} \frac{1}{2} \sum_{\substack{i \neq j \\ \sigma \sigma'}} V_{ij} c_{i\sigma}^\dagger c_{j\sigma'}^\dagger \underbrace{c_{j\sigma'} c_{i\sigma}}_{=-c_{i\sigma} c_{j\sigma'}} &= -\frac{1}{2} \sum_{\substack{i \neq j \\ \sigma \sigma'}} V_{ij} c_{i\sigma}^\dagger c_{j\sigma'}^\dagger c_{i\sigma} c_{j\sigma'} \\ &= -\frac{1}{2} \sum_{\substack{i \neq j \\ \sigma \sigma'}} V_{ij} c_{i\sigma}^\dagger (-c_{i\sigma} c_{j\sigma'}^\dagger + \underbrace{\delta_{i,j} \delta_{\sigma\sigma'}}_{=0}) c_{j\sigma'} \\ &= \frac{1}{2} \sum_{\substack{i \neq j \\ \sigma \sigma'}} V_{ij} n_{i\sigma} n_{j\sigma'} \end{aligned} \quad (3.33)$$

Again, one is going to expand the spin terms in the Eq.3.33. So, there are four possible spin term configurations which are $\{\sigma = \uparrow, \sigma' = \uparrow\}$, $\{\sigma = \downarrow, \sigma' = \downarrow\}$, $\{\sigma = \uparrow, \sigma' = \downarrow\}$ or $\{\sigma = \downarrow, \sigma' = \uparrow\}$. Therefore,

$$= \frac{1}{2} \sum_{i \neq j} V_{ij} (n_{i\uparrow} n_{j\uparrow} + n_{i\downarrow} n_{j\downarrow} + n_{i\uparrow} n_{j\downarrow} + n_{i\downarrow} n_{j\uparrow}) \quad (3.34)$$

$$= \frac{1}{2} \sum_{i \neq j} V_{ij} \underbrace{(n_{i\uparrow} + n_{i\downarrow})}_{n_i} \underbrace{(n_{j\uparrow} + n_{j\downarrow})}_{n_j} \quad (3.35)$$

$$= \frac{1}{2} \sum_{i \neq j} V_{ij} n_i n_j \quad (3.36)$$

Eventually, one will substitute the on-site interaction term in the Eq.3.31 and off-site direct interaction term in the Eq.3.36 into Eq.3.29 to get Hubbard and extended Hubbard Hamiltonian,

$$H = \underbrace{\sum_{\substack{\langle ij \rangle \\ \sigma}} t_{ij} c_{i\sigma}^\dagger c_{j\sigma}}_{\text{Hubbard Model}} + U \sum_i n_{i\uparrow} n_{i\downarrow} + \frac{1}{2} \sum_{i \neq j} V_{ij} n_i n_j \quad (3.37)$$

Extended Hubbard Model

After all, above equation is exact Hubbard Hamiltonian. We should do an approximation in order to solve Hubbard model by using Weiss mean-field theory that was first introduced by Weiss (Weiss (1907)). So, following equations is defined as,

$$n_{i\uparrow} = \langle n_{i\uparrow} \rangle + \underbrace{(n_{i\uparrow} - \langle n_{i\uparrow} \rangle)}_{\Delta n_{i\uparrow}} \quad (3.38)$$

$$n_{i\downarrow} = \langle n_{i\downarrow} \rangle + \underbrace{(n_{i\downarrow} - \langle n_{i\downarrow} \rangle)}_{\Delta n_{i\downarrow}} \quad (3.39)$$

Assuming $\Delta n_{i\uparrow}$ and $\Delta n_{i\downarrow}$ terms are really small and apply these terms to the on-site term in the Eq.(3.37),

$$\begin{aligned} n_{i\uparrow}n_{i\downarrow} &= [\langle n_{i\uparrow} \rangle + (n_{i\uparrow} - \langle n_{i\uparrow} \rangle)][\langle n_{i\downarrow} \rangle + (n_{i\downarrow} - \langle n_{i\downarrow} \rangle)] \\ &\approx \langle n_{i\uparrow} \rangle \langle n_{i\downarrow} \rangle + \langle n_{i\uparrow} \rangle (n_{i\downarrow} - \langle n_{i\downarrow} \rangle) + \langle n_{i\downarrow} \rangle (n_{i\uparrow} - \langle n_{i\uparrow} \rangle) \\ &\quad + \underbrace{(n_{i\uparrow} - \langle n_{i\uparrow} \rangle)(n_{i\downarrow} - \langle n_{i\downarrow} \rangle)}_{\approx 0} \\ &\approx n_{i\uparrow} \langle n_{i\downarrow} \rangle + n_{i\downarrow} \langle n_{i\uparrow} \rangle - \langle n_{i\uparrow} \rangle \langle n_{i\downarrow} \rangle \end{aligned} \quad (3.40)$$

On the other hand, defining these terms for off-site term and similarly applying,

$$n_i = \langle n_i \rangle + \underbrace{(n_i - \langle n_i \rangle)}_{\Delta n_i} \quad (3.41)$$

$$n_j = \langle n_j \rangle + \underbrace{(n_j - \langle n_j \rangle)}_{\Delta n_j} \quad (3.42)$$

these above terms turn into,

$$n_i n_j \approx n_i \langle n_j \rangle + n_j \langle n_i \rangle - \langle n_i \rangle \langle n_j \rangle \quad (3.43)$$

Consequently, Hamiltonian becomes by using Eq.(3.40) and Eq.(3.43),

$$\begin{aligned} H_{MF} &\approx \sum_{\substack{\langle ij \rangle \\ \sigma}} t_{ij} c_{i\sigma}^\dagger c_{j\sigma} + U \sum_i (n_{i\uparrow} \langle n_{i\downarrow} \rangle + n_{i\downarrow} \langle n_{i\uparrow} \rangle - \langle n_{i\uparrow} \rangle \langle n_{i\downarrow} \rangle) \\ &\quad + \frac{1}{2} \sum_{i \neq j} V_{ij} (n_i \langle n_j \rangle + n_j \langle n_i \rangle - \langle n_i \rangle \langle n_j \rangle) \end{aligned} \quad (3.44)$$

Moreover, there is another approximation that electrons of system interact with fixed ion. So, following values are defined as,

$$\langle n_i \rangle \equiv 1 \quad (3.45)$$

$$\langle n_{i\sigma} \rangle \equiv \frac{1}{2} \quad (3.46)$$

after that, one will define bulk mean-field Hamiltonian,

$$H_{MF}^{Bulk} = \sum_{\langle ij \rangle}^{\sigma} t_{ij} c_{i\sigma}^{\dagger} c_{j\sigma} + U \sum_i \left(\frac{n_{i\uparrow}}{2} + \frac{n_{i\downarrow}}{2} - \frac{1}{4} \right) + \frac{1}{2} \sum_{i \neq j} V_{ij} (n_i + n_j - 1) \quad (3.47)$$

now, one will obtain one body mean-field Hubbard Hamiltonian by using next expression and put each one of terms which are Eq.(3.44) and Eq.(3.47)

$$\begin{aligned} H_{MF} &= H_{MF} - H_{MF}^{Bulk} + H_{MF}^{Bulk} \\ &= \sum_{\langle ij \rangle}^{\sigma} t_{ij} c_{i\sigma}^{\dagger} c_{j\sigma} + U \sum_i (n_{i\uparrow} \langle n_{i\downarrow} \rangle + n_{i\downarrow} \langle n_{i\uparrow} \rangle - \langle n_{i\uparrow} \rangle \langle n_{i\downarrow} \rangle) \\ &\quad + \frac{1}{2} \sum_{i \neq j} V_{ij} (n_i \langle n_j \rangle + n_j \langle n_i \rangle - \langle n_i \rangle \langle n_j \rangle) \\ &\quad - \sum_{\langle ij \rangle}^{\sigma} t_{ij} c_{i\sigma}^{\dagger} c_{j\sigma} - U \sum_i \left(\frac{n_{i\uparrow}}{2} + \frac{n_{i\downarrow}}{2} - \frac{1}{4} \right) - \frac{1}{2} \sum_{i \neq j} V_{ij} (n_i + n_j - 1) \\ &\quad + \sum_{\langle ij \rangle}^{\sigma} t_{ij} c_{i\sigma}^{\dagger} c_{j\sigma} + U \sum_i \left(\frac{n_{i\uparrow}}{2} + \frac{n_{i\downarrow}}{2} - \frac{1}{4} \right) + \frac{1}{2} \sum_{i \neq j} V_{ij} (n_i + n_j - 1) \\ H_{MF} &= \underbrace{\sum_{\langle ij \rangle}^{\sigma} t_{ij} c_{i\sigma}^{\dagger} c_{j\sigma} + \frac{U}{2} \sum_i (n_{i\uparrow} + n_{i\downarrow}) + \frac{1}{2} \sum_{i \neq j} V_{ij} (n_i + n_j)}_{\sum_{\langle ij \rangle}^{\sigma} \tau_{ij} (c_{i\sigma}^{\dagger} c_{j\sigma} + h.c.)} \\ &\quad + U \sum_i \left[\left(\langle n_{i\uparrow} \rangle - \frac{1}{2} \right) n_{i\downarrow} + \left(\langle n_{i\downarrow} \rangle - \frac{1}{2} \right) n_{i\uparrow} \right] \\ &\quad + \frac{1}{2} \sum_{i \neq j} V_{ij} \left[\left(\langle n_i \rangle - 1 \right) n_j + \left(\langle n_j \rangle - 1 \right) n_i \right] + \kappa \end{aligned} \quad (3.48)$$

In addition, we know $V_{ij} = V_{ji}$. So, mean-field Hamiltonian turns into following last form,

$$\begin{aligned}
H_{MFH} = & \sum_{\substack{\langle ij \rangle \\ \sigma}} \tau_{ij} (c_{i\sigma}^\dagger c_{j\sigma} + h.c.) + U \sum_i [(\langle n_{i\uparrow} \rangle - \frac{1}{2})n_{i\downarrow} + (\langle n_{i\downarrow} \rangle - \frac{1}{2})n_{i\uparrow}] \\
& + \frac{1}{2} \sum_{i \neq j} V_{ij} [(\langle n_i \rangle - 1)n_j + (\langle n_j \rangle - 1)n_i] \tag{3.49}
\end{aligned}$$

Eventually, we told all models used in this thesis. So, we are done with this theoretical model chapter and need to keep moving with methods. In next chapter, we will get more detail about procedure of each models.

CHAPTER 4

NUMERICAL METHODS

In this chapter, we will define a method that is a observable path, procedure and duration in order to find out a truth in the scientific research for each defined models. All above models are going to be numerically solved to obtain results. Moreover, their working principle will be explained in detail one by one.

On the other hand, this thesis completely consists of two main part. One of them is to be Anderson model and tight-binding model that is integrated to the Anderson model in order to examine. Second one is mean-field Hubbard model that turns into the mean-field Anderson model. As a results of this, above explained first model will be distinctly discuss in this chapter. After using these models, we will obtain results that will be mentioned in result chapter. To begin with simple and precise TB.

4.1. Tight-Binding

In the section (3.1), we found the hopping parameter for the bulk graphene. During this research, we work on zigzag graphene nanoribbons with periodic boundary condition which has finite structure and certain atom numbers. Thus, we will apply the TB method to finite ZGNRs in real space. In this section, we will explain about application and inner working principle of TB method.

Let us introduce the TB Hamiltonian,

$$H_{tb} = t \sum_{\langle i,j \rangle} c_i^\dagger c_j \quad (4.1)$$

where $\langle i, j \rangle$ denotes only nearest neighbour hopping that is allowed, c_i^\dagger (c_j) is creation (annihilation) operator at site i (j) for an electron. Moreover, an electron is sitting at j site and suddenly hopping to the i site which is nearest neighbour of electron located at j site.

Now, we should construct the TB Hamiltonian by defining a method which is matrix for finite system size as shown in the Fig.(4.1). Here, we have mentioned before,

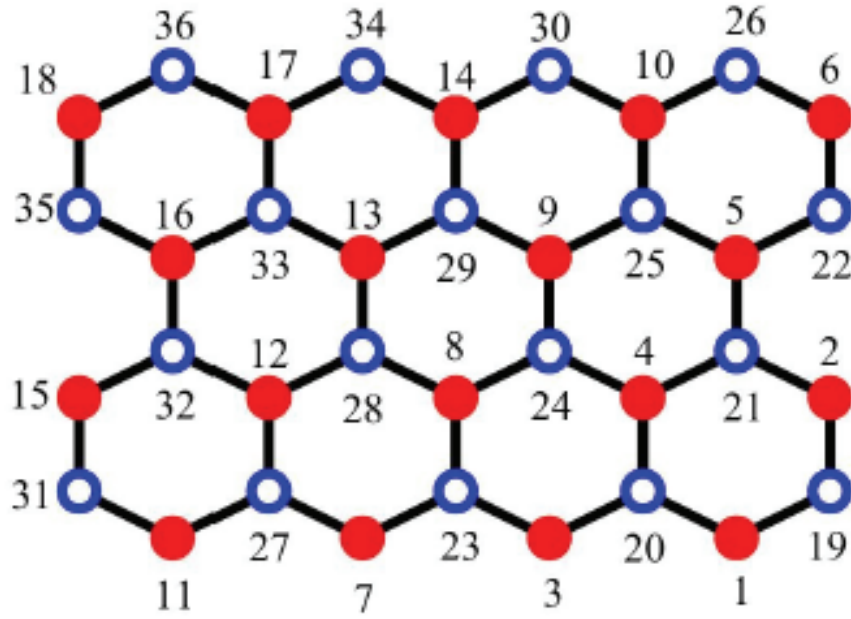


Figure 4.1. Zigzag graphene nanoribbon consists of 36 carbon atoms

graphene consists of two different sublattices which are A sublattice marked by blue and B sublattice marked by red in the Fig.(4.1). On the other hand, total number of atom is 36 atoms. So, atom number 1 on edge site has two neighbours which are 19th and 20th atoms. Secondly, the TB Hamiltonian matrix is built by $(N \times N)$ matrix where N is number of atom. Moreover, first row in the matrix belong to the our 1st atom that is hopping to 19th and 20th. Hence, we are writing hopping parameter as t to column of the 19th and 20th matrix element. So, rest of all elements are zero. Therefore, all rows are filled up with similar way, gradually.

After constructing the TB Hamiltonian matrix, one need to do diagonalization process in order to get results as numerical. Moreover, at end of this process, we will obtain eigenvalues and eigenfunctions of the above defined system corresponding to the labeled atom indices. As a results of this, we can obtain energy spectrum, density of states and probability density of related system by examining the results. Although there is no electron-electron interaction, we can obtain accurate results in a short time thanks to the TB for any system. As a results of this, the TB Hamiltonian is a part of the Anoderson model and mean-field Anderson model. In the next section, we will mention the Hirsch-Fye Quantum Monte Carlo Algorithm for the Anderson Model.

4.2. Hirsch-Fye Quantum Monte Carlo Algorithm

In this section, the Hirsch-Fye quantum Monte Carlo (HFQMC) algorithm for the two-impurities Anderson model given in the Eq.(3.19) will be described. The quantum Monte Carlo algorithm that we used was provided by Prof. Dr. Nejat Bulut (Bulut (2003); Bulut et al. (2007); Kandemir, Zafer et al. (2016); Mayda et al. (2017); Bulut and Maekawa (2006); Bulut (2002); Öztarhan (2018); Mayda (2013)) and uses two vital things which are Trotter decomposition and discrete Hubbard-Stratonovich (HS) transformation. HS transformation allows us to map a interacting electron system to a non-interacting electron system with a fluctuating magnetic field. Moreover, electrons move in that field which is determined by using a set of random spin configurations. Then, these random spin configurations are generated by using a heat-bath or Metropolis algorithm with a probability. Moreover, spin configurations are accepted or rejected by Monte Carlo method that is based on a random sampling technique to obtain numerical results. Thus, several methods can sample partition function in quantum mechanics in order to calculate expectation value of an observable (Gull et al. (2011); Sandvik and Kurkijärvi (1991)). Then they lead us to quantum Monte Carlo (QMC). On the other hand, in this research, a discrete partition function is used by defining the auxiliary field which discretizes the operator or the action. Therefore, the algorithm samples summation of the discrete partition function instead of dealing with all entire spin configuration. Moreover, the method is concerned with the calculation of the Green's function at finite temperature that allows researcher to measure the electronic and magnetic properties of the system.

The two-impurity Anderson Hamiltonian in the Eq.(3.19) can be written in two parts, H_0 and H_1 ,

$$H = H_0 + H_1 \quad (4.2)$$

where H_0 is the non-interacting terms

$$\begin{aligned} H_0 = & t \sum_{\substack{\langle i,j \rangle \\ \sigma}} c_{i\sigma}^\dagger c_{j\sigma} + \sum_{i,\sigma} (E_d - \mu) d_{i\sigma}^\dagger d_{i\sigma} \\ & + \sum_{i,j,\sigma} (V_{ij} c_{i\sigma}^\dagger d_{j\sigma} + h.c.) + \frac{U}{2} \sum_i (n_{id\uparrow} + n_{id\downarrow}) \end{aligned} \quad (4.3)$$

where H_1 is all interaction terms.

$$H_1 = U \sum_i n_{id\uparrow} n_{id\downarrow} - \frac{U}{2} \sum_i (n_{id\uparrow} + n_{id\downarrow}) \quad (4.4)$$

The partition function for the system can be written as,

$$Z = Tr e^{-\beta(H_0+H_1)} = Tr \prod_{i=1}^L e^{-\Delta\tau(H_0+H_1)} \quad (4.5)$$

Trotter approximation (Trotter (1959); Suzuki (1976); Hatano and Suzuki (2005)) is used in order to separate into simpler components. Then, the partition function can be written as,

$$\cong Tr \prod_{i=1}^L (e^{-\Delta\tau H_0} e^{-\Delta\tau H_1} + O(\Delta\tau^2)) \quad (4.6)$$

In addition, imaginary time interval between 0 and β is discretized into L time slice with defined $\beta = \Delta\tau L$. Now, we can use discrete the Hubbard-Stratonovich transformation (Hubbard (1959); Stratonovich (1957)) and define following identity (Hirsch (1983)),

$$n_{d\uparrow} n_{d\downarrow} = -\frac{1}{2} (n_{d\uparrow} - n_{d\downarrow})^2 + \frac{1}{2} (n_{d\uparrow} + n_{d\downarrow})^2 \quad (4.7)$$

and this identity is applied to the H_1 interaction term. So, following equation is obtained,

$$H_1 = -\frac{U}{2} \sum_i (n_{id\uparrow} - n_{id\downarrow})^2 \quad (4.8)$$

with $\cosh(\lambda_i) = e^{\frac{1}{2}\Delta\tau U_i}$,

$$e^{-\Delta\tau H_1} = \exp\left\{-\Delta\tau \sum_i \frac{U}{2} (n_{id\uparrow} - n_{id\downarrow})^2\right\} \quad (4.9)$$

$$= \frac{1}{2} \sum_{S_i=\pm 1} \exp\left\{\sum_i \lambda_i S_i (n_{id\uparrow} - n_{id\downarrow})\right\} \quad (4.10)$$

where S_i is an auxiliary field that is a fluctuating field. Moreover, that field takes the

values as $+1$ and -1 . So, the summation over these discrete S values is vital for HFQMC algorithm. After we apply the Trotter approximation and discrete Hubbard-Stratonovich transformation which allows us to map the many-body interacting problem to a system of non-interacting problem with a fluctuating field (Hirsch (1983); Kristjan (2006)), the partition function becomes,

$$\begin{aligned}
Z &= Tr \left\{ \prod_{l=1}^L \frac{1}{2} \sum_{S_{li}=\pm 1} \exp \left\{ -\Delta\tau H_0 \right\} \exp \left\{ \sum_i \lambda_i S_{li} (n_{id\uparrow} - n_{id\downarrow}) \right\} \right\} \\
&= Tr \prod_{l=1}^L \frac{1}{2} \sum_{S_{li}=\pm 1} \exp \left\{ -\Delta\tau \sum_{ij} K_{ij} c_{i\uparrow}^\dagger c_{j\uparrow} \right\} \exp \left\{ \sum_i +\lambda_i S_{li} n_{id\uparrow} \right\} \\
&\quad \exp \left\{ -\Delta\tau \sum_{ij} K_{ij} c_{i\downarrow}^\dagger c_{j\downarrow} \right\} \exp \left\{ \sum_i -\lambda_i S_{li} n_{id\downarrow} \right\} \quad (4.11)
\end{aligned}$$

where K is an $(N+2) \times (N+2)$ matrix form for the bilinear part of H and N is number of host electrons,

$$H_0 = \sum_{ij\sigma} K_{ij} a_{i\sigma}^\dagger a_{j\sigma} \quad (4.12)$$

$$H_\uparrow = \sum_{ij} K_{ij} c_{i\uparrow}^\dagger c_{j\uparrow} - \frac{\sum_i \lambda_i S_{li} n_{id\uparrow}}{\Delta\tau} \quad (4.13)$$

$$H_\downarrow = \sum_{ij} K_{ij} c_{i\downarrow}^\dagger c_{j\downarrow} + \frac{\sum_i \lambda_i S_{li} n_{id\downarrow}}{\Delta\tau} \quad (4.14)$$

Also, a shows c and d electrons. On the other hand, we define following equation,

$$V_i^\sigma = \sigma \lambda_i S_i |i\rangle \langle i| \quad (4.15)$$

the Eq.(4.15) is a potential and acting at the impurity sites. Moreover, its matrix form is a diagonal $(N+2) \times (N+2)$ matrix. Its matrix elements are $e^{V_i^\sigma}$ for the impurity sites, 1 for the host sites and 0 for rest of all off-diagonal terms. Additionally, we now introduce following matrix $B_{li}^\sigma = e^{-\Delta\tau K} e^{V_i^\sigma}$. After using previous defined equation, we can rewrite the partition function as,

$$Z = \sum_{\{S_{li}=\pm 1\}} \prod_{\sigma=\pm 1} \det[I + B_{Li}(\sigma)B_{L-1i}(\sigma) \dots B_{1i}(\sigma)] \quad (4.16)$$

$$= \sum_{\{S_{li}=\pm 1\}} \det \vartheta_{\uparrow}(\{S_{li}\}) \det \vartheta_{\downarrow}(\{S_{li}\}) \quad (4.17)$$

where ϑ_{li}^{σ} is an $(N+2)L \times (N+2)L$ matrix, N is the number of hosts with 2 adatoms and L is number of times slices. So, the single particle Green's function is defined as,

$$G_{dd'}^{\sigma} = -\langle T_{\tau} d_{d\sigma} d_{d'\sigma}^{\dagger} \rangle \quad (4.18)$$

$$= -\frac{1}{Z} Tr \{ e^{-\beta H} T_{\tau} d_{d\sigma}(l) d_{d'\sigma}^{\dagger}(l') \} \quad (4.19)$$

the one-particle Green's function is the inverse of the matrix ϑ_{ld}^{σ} . Thus, there is a relation between these two (Kristjan (2006); Fye and Hirsch (1988)).

$$G_{dd'} = (\vartheta_{ld}^{\sigma})^{-1} \quad (4.20)$$

As we has mentioned before, the size of the ϑ_{ld}^{σ} is $(N+2)L \times (N+2)L$. Thus, calculation of the Green's functions for the huge system size with the set of spin configurations is very difficult.

4.2.1. New Green's Function from the Old Green's Function

Here, new Green's function (G^{sigma})' will be derived with new spin configuration $\{S'_l\}$ from the old Green's function with old spin configuration $\{S_l\}$ by using Hirsch and Fye algorithm (Hirsch and Fye (1986); Fye and Hirsch (1988)). Moreover, they noticed that the Green's function can be calculated for a spin configuration. Then, after changing one spin flip, new spin configuration is arranged for new condition. So, G can be updated to the new Green's function with new spin configurations. Also, a Dyson's equatin connects to the Green's functions of different spin changing. Thus, we define G^{-1}

and $e^{V_{1d}}$ matrix with dropping the spin indices for simplicity.

$$G^{-1} = \begin{pmatrix} I & 0 & \cdots & & & B_L \\ -B_1 & I & 0 & & & 0 \\ 0 & -B_2 & I & & & \vdots \\ \vdots & \vdots & \vdots & \ddots & & \vdots \\ & & & & I & 0 \\ 0 & 0 & \cdots & 0 & -B_{L-1} & I \end{pmatrix}_{(N+2)L \times (N+2)L} \quad (4.21)$$

$$(e^{V_{1d}})^{-1} = \begin{pmatrix} [(e^{V_{1d}})]_{(N+2) \times (N+2)}^{-1} & & & & 0 \\ & [(e^{V_{2d}})]_{(N+2) \times (N+2)}^{-1} & & & \\ & & \ddots & & \\ 0 & & & & [(e^{V_{Ld}})]_{(N+2) \times (N+2)}^{-1} \end{pmatrix} \quad (4.22)$$

where $B_{lv} = e^{-\Delta\tau K} e^{V_{lv}}$. Also, dimension of above matrix is $(N+2)L \times (N+2)L$. So, matrix multiplication is done for these two matrices,

$$G^{-1}(e^{V_{1d}})^{-1} = \begin{pmatrix} [(e^{V_{1d}})]^{-1} & 0 & \cdots & & & e^{-\Delta\tau K} \\ -e^{-\Delta\tau K} & [(e^{V_{2d}})]^{-1} & 0 & & & 0 \\ 0 & -e^{-\Delta\tau K} & [(e^{V_{3d}})]^{-1} & & & \vdots \\ \vdots & \vdots & \vdots & \ddots & & \vdots \\ & & & & [(e^{V_{(L-1)d}})]^{-1} & 0 \\ 0 & 0 & \cdots & 0 & -e^{-\Delta\tau K} & [(e^{V_{Ld}})]^{-1} \end{pmatrix} \quad (4.23)$$

Here, following equation is obtained by using above calculations,

$$\tilde{G} = e^V G \quad (4.24)$$

$$(\tilde{G})^{-1} = G^{-1}(e^V)^{-1} \quad (4.25)$$

According to the above obtained result, off-diagonal elements of matrix do not depend on spin configuration. When the HS field is changed, only diagonal elements of above matrix change. So, it can be written,

$$(\tilde{G}')^{-1} - (\tilde{G})^{-1} = (e^{V'})^{-1} - (e^V)^{-1} \quad (4.26)$$

Now, multiplying both sides by \tilde{G} and \tilde{G}' ,

$$\tilde{G} - \tilde{G}' = \tilde{G}((e^{V'})^{-1} - (e^V)^{-1})\tilde{G}' \quad (4.27)$$

$$\tilde{G}' = \tilde{G} - \tilde{G}((e^{V'})^{-1} - (e^V)^{-1})\tilde{G}' \quad (4.28)$$

by using Eq.(4.25),

$$e^{V'}G' = e^VG - e^VG((e^{V'})^{-1} - (e^V)^{-1})e^{V'}G' \quad (4.29)$$

Then, dividing both sides by e^V ,

$$(e^V)^{-1}e^{V'}G' = G - G((e^V)^{-1}e^{V'} - I)G' \quad (4.30)$$

Adding G' to the both sides,

$$G'_{dd} = G_{dd} + (G_{dd} - I)((e^V)^{-1}e^{V'} - I)G'_{dd} \quad (4.31)$$

where G_{dd} is a $L \times L$ matrix that is old one, G'_{dd} is a $L \times L$ matrix that is new one. Moreover, $((e^V)^{-1}e^{V'} - I)$ is a $L \times L$ diagonal matrix where I is a $L \times L$ identity matrix. Accordingly, the relation between the new Green's function and the old Green's function is found as,

$$G'_{dd} = \{I - (G_{dd} - I)((e^V)^{-1}e^{V'} - I)\}^{-1}G_{dd} \quad (4.32)$$

4.2.2. Initial Calculation of Green's Function G^σ from G^0 and e^V

In the Hirsch-Fye quantum Monte Carlo method (Fye and Hirsch (1988)), the relation in the Eq.(4.32) was found between the new and old Green's function. Thus, we should do some adjustment in order to find new relation for the initial calculation of Green's function.

$$\begin{aligned} G' &\longrightarrow G^\sigma \\ G &\longrightarrow G^0 \end{aligned} \quad (4.33)$$

The equation in (4.32) turns into new one with above identities,

$$G_{dd}^\sigma = \{I - (G_{dd}^0 - I)((e^{V'-V} - I))^{-1}\} G_{dd}^0 \quad (4.34)$$

where G_{dd}^0 is the impurity Green's function for case $\{S_l\}$ that is set to zero. So, we can define and calculate the Green's function $G_{dd}^\sigma(l, l')$,

$$G_{dd'}^\sigma(l, l') = -\langle T_\tau d_{d\sigma} d_{d'\sigma}^\dagger \rangle \quad (4.35)$$

where T_τ is Matsubara time ordering operator. G_{dd}^0 is calculated from the H_0 part of the Hamiltonian that is recalled,

$$\begin{aligned} H_0 &= t \sum_{\substack{\langle i,j \rangle \\ \sigma}} c_{i\sigma}^\dagger c_{j\sigma} + \sum_{i,\sigma} (E_d - \mu) d_{i\sigma}^\dagger d_{i\sigma} \\ &+ \sum_{i,j,\sigma} (V_{ij} c_{i\sigma}^\dagger d_{j\sigma} + h.c.) + \frac{U}{2} \sum_i (n_{id\uparrow} + n_{id\downarrow}) \end{aligned} \quad (4.36)$$

The above impurity Green's function with hybridization and no Coulomb interaction ($U = 0$) can be calculated by using the following Feynman's diagrams, From the above Feynman's diagram, the Dyson's equation can be obtained,

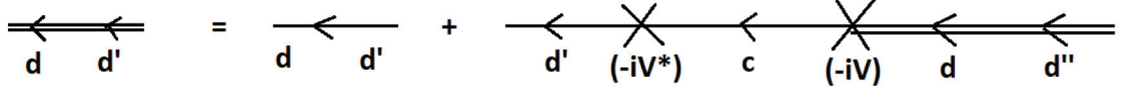


Figure 4.2. Feynman diagram for the impurity Green's function $G_{dd'}^0(i\omega_n)$ and $U = 0$. Double lines denote $G_{dd'}^0(i\omega_n)$ and single lines denote $g_c(i\omega_n)$ and $g_d(i\omega_n)$ for the non-interacting Green's functions.

$$G_{dd'}^0(i\omega_n) = \delta_{dd'} g_{d'}(i\omega_n) + \sum_{k,d''} g_{d'}(i\omega_n) V_{d'',k}^* g_c(k, i\omega_n) V_{k,d'} G_{d,d''}^0(i\omega_n) \quad (4.37)$$

$$G_{dd'}^0(i\omega_n) = \delta_{dd'} g_{d'}(i\omega_n) + \sum_{d''} g_{d'}(i\omega_n) \underbrace{\left\{ \sum_k |V_{d'',d'}|^2 g_c(k, i\omega_n) \right\}}_{\text{self-energy: } \Sigma(k, i\omega_n)} G_{d,d''}^0(i\omega_n) \quad (4.38)$$

Before going on, we should define two things that non-interacting Green's function for the impurities and host is defined with no hybridization ($V_{ij} = 0$) and no Coulomb ($U = 0$) interaction,

$$g_c(i\omega_n) = \frac{1}{i\omega_n - (\varepsilon_k - \mu)} \quad (\text{for the host electrons}) \quad (4.39)$$

$$g_d(i\omega_n) = \frac{1}{i\omega_n - (E_d - \mu)} \quad (\text{for the impurity electrons}) \quad (4.40)$$

where $\omega_n = (2n + 1)\pi T$ is Matsubara frequency with temperature T for fermion and n that is from $-\infty$ to ∞ . Also, we introduce the self-energy which is,

$$\Sigma(k, i\omega_n) = F_{d,d'}(k, i\omega_n) = \sum_k |V_{d,d'}|^2 \underbrace{\frac{1}{i\omega_n - (\varepsilon_k - \mu)}}_{g_c(i\omega_n)} \quad (4.41)$$

As a results of this, G^0 is calculated in the Eq.(4.38) which is the Dyson's equation and obtained in frequency space ($i\omega_n$). After calculating all Green's functions, they are transformed to imaginary time space ($\tau = it$). In this space, physical measurements are going to be done to obtain results.

4.2.3. Ratio of the Determinants

In this section, the ratio of the determinants will be calculated and used in updating Green's functions with new spin configuration S_{ld} . Namely, in a quantum Monte Carlo simulation, new spin configuration is generated by a probability of the ratio of the determinants of ϑ'_σ and ϑ_σ . Moreover, we omitted the spin indices for simplicity.

$$S_l \longrightarrow S'_l = -S_l$$

To start with recalling the following equation,

$$\tilde{G}'_{dd'} = \tilde{G}_{dd'} - \tilde{G}_{dd'}((e^{V'_{ld}})^{-1} - (e^{V_{ld}})^{-1})\tilde{G}'_{dd'} \quad (4.42)$$

where $\tilde{G}_{dd'} = e^{V_{ld}}G_{dd'}$. So, multiplying both sides by $(\tilde{G}'_{dd'})^{-1}$ on the right,

$$I = \tilde{G}_{dd'}(\tilde{G}'_{dd'})^{-1} - \tilde{G}_{dd'}((e^{V'_{ld}})^{-1} - (e^{V_{ld}})^{-1}) \quad (4.43)$$

$$\tilde{G}_{dd'}(\tilde{G}'_{dd'})^{-1} = I + \tilde{G}_{dd'}((e^{V'_{ld}})^{-1} - (e^{V_{ld}})^{-1}) \quad (4.44)$$

Recalling $G_{dd'} = (\vartheta_d)^{-1}$ from Eq.(4.20),

$$\tilde{G}_{dd'} = e^{V_{ld}}G_{dd'} \quad (4.45)$$

$$= e^{V_{ld}}(\vartheta_d)^{-1} \quad (4.46)$$

Thus, inserting Eq.(4.46) into Eq.(4.44),

$$(e^{V_{ld}}(\vartheta_d)^{-1})(e^{V'_{ld}}(\vartheta'_d))^{-1} = I + (e^{V_{ld}}G_{dd'})((e^{V'_{ld}})^{-1} - (e^{V_{ld}})^{-1}) \quad (4.47)$$

Here, multiplying by $e^{-V_{ld}}$ on the left and $e^{V'_{ld}}$ on the right,

$$(\vartheta_d)^{-1}(\vartheta'_d) = e^{-V_{ld}}e^{V'_{ld}} + G_{dd'}(I - e^{-V_{ld}}e^{V'_{ld}}) \quad (4.48)$$

$$= e^{-V_{ld}}e^{V'_{ld}}(G_{dd'} - I)(I - e^{-V_{ld}}e^{V'_{ld}}) + (I - e^{-V_{ld}}e^{V'_{ld}}) \quad (4.49)$$

Hence,

$$(\vartheta_d)^{-1}(\vartheta'_{ld}) = I + (I - G_{dd'})(e^{V'_{ld}}e^{-V_{ld}} - I) \quad (4.50)$$

Taking the determinant of the both sides, following equation is obtained,

$$\frac{\det \vartheta'_{ld}}{\det \vartheta_{ld}} = \det(I + (I - G_{dd'})(e^{V'_{ld}-V_{ld}} - I)) \quad (4.51)$$

Therefore, the ratio of the determinants with the spin dependency,

$$R_\sigma = \frac{\det \vartheta'_{ld}}{\det \vartheta_{ld}} = \det A_\sigma \quad (4.52)$$

where,

$$A_\sigma = I + (I - G_{dd'}^\sigma)(e^{V'_{ld}-V_{ld}} - I) \quad (4.53)$$

In the quantum Monte Carlo algorithm, heat-bath algorithm is used in order to determine the transition probability from the old spin configurations $\{S_{ld}\}$ to the new spin configurations $\{S'_{ld}\}$. On the other hand, random number is generated between 0 and 1. Additionally, if this probability is greater than the random number, the new spin configurations are acceptable move. Otherwise, that move is rejected.

$$P(S_{ld} \longrightarrow S'_{ld}) = \frac{P}{1 + P} \quad (4.54)$$

where

$$P = R_\uparrow R_\downarrow \quad (4.55)$$

4.2.4. Calculation of Updated Impurity Green's Function for the New Spin Field Configuration

In this section, new expressions will be derived for the updated Green's functions. As seen in the Eq.(4.31), there is the relation between the old and the new Green's function. So, Eq.(4.32) is recalled in order to insert into the following equation,

$$G'_{dd} = G_{dd} + (G_{dd} - I)((e^V)^{-1}e^{V'} - I)G'_{dd} \quad (4.56)$$

and

$$G'_{dd} = \{I - (G_{dd} - I)((e^V)^{-1}e^{V'} - I)\}^{-1}G_{dd} \quad (4.57)$$

The expression for the updated algorithm is obtained. Thus, when S_{ld} is flipped, the new impurity Green's function is given by,

$$(G'_{dd'})^\sigma = G_{dd'}^\sigma + (G_{dd'}^\sigma - I)(e^{V'_{ld}-V_{ld}} - I)A_\sigma^{-1}G_{dd'}^\sigma \quad (4.58)$$

where

$$A_\sigma = I + (I - G_{dd'}^\sigma)(e^{V'_{ld}-V_{ld}} - I) \quad (4.59)$$

4.2.5. Quantum Monte Carlo Measurements

Thanks to the Green's function method which are calculated by using Hirsch-Fye QMC technique, physical measurements is done. Moreover, the numerical results are obtained and represented in the results chapter. Roughly speaking, during the calculation time, we wait the system to reach equilibrium state at the given temperature. Speaking of equilibrium, number of warm up and number of measurements sweeps were described in the simulations. So, warm up is the thermalization of the system at given temperature.

After certain warm up, measurements start. Then, the Green's functions are calculated and sampled from the spin configurations $\{S_{ld}\}$. Thus, we take average of them over the QMC samples. The single Green's functions in the Matsubara time are defined by following equation,

$$G_{dd'}^\uparrow(\tau) = -\langle T_\tau d_{d\uparrow}(\tau' + \tau) d_{d'\uparrow}^\dagger(\tau') \rangle \quad (4.60)$$

$$G_{dd'}^\downarrow(\tau) = -\langle T_\tau d_{d\downarrow}(\tau' + \tau) d_{d'\downarrow}^\dagger(\tau') \rangle \quad (4.61)$$

where d and d' defines the impurities and T_τ is the Matsubara time ordering operator. The physical measurements is calculated in terms of the single particle Green's function using the following commutation relation between the impurity electrons,

$$\{d_{d\sigma}, d_{d'\sigma'}^\dagger\} = \delta_{dd'} \delta_{\sigma\sigma'} \quad (4.62)$$

the magnetization operators are defined by,

$$M_d^z = d_{d\uparrow}^\dagger d_{d\uparrow} - d_{d\downarrow}^\dagger d_{d\downarrow} \quad (4.63)$$

the equal-time magnetic correlation function,

$$\begin{aligned} \langle (M_d^z)^2 \rangle &= \langle (d_{d\uparrow}^\dagger d_{d\uparrow} - d_{d\downarrow}^\dagger d_{d\downarrow})(d_{d\uparrow}^\dagger d_{d\uparrow} - d_{d\downarrow}^\dagger d_{d\downarrow}) \rangle \quad (4.64) \\ &= \frac{1}{L} \sum_{i=1}^L \left\langle (G_{dd}^\uparrow(\tau_i, \tau_i) - G_{dd}^\downarrow(\tau_i, \tau_i))^2 \right. \\ &\quad + G_{dd}^\uparrow(\tau_i, \tau_i)(1 - G_{dd}^\uparrow(\tau_i, \tau_i)) \\ &\quad \left. + G_{dd}^\downarrow(\tau_i, \tau_i)(1 - G_{dd}^\downarrow(\tau_i, \tau_i)) \right\rangle_{mc} \quad (4.65) \end{aligned}$$

the square of the magnetic moment of the impurity is $\langle (M_d^z)^2 \rangle$, so,

$$(m_d^{eff})^2 = \langle M_d^z M_d^z \rangle \quad (4.66)$$

the magnetic correlation functions between the two impurities,

$$\langle (M_d^z M_{d'}^z) \rangle = \langle (d_{d\uparrow}^\dagger d_{d\uparrow} - d_{d\downarrow}^\dagger d_{d\downarrow})(d_{d'\uparrow}^\dagger d_{d'\uparrow} - d_{d'\downarrow}^\dagger d_{d'\downarrow}) \rangle \quad (4.67)$$

$$\begin{aligned} &= \frac{1}{L} \sum_{i=1}^L \left\langle (G_{dd}^\uparrow(\tau_i, \tau_i) - G_{dd}^\downarrow(\tau_i, \tau_i)) \right. \\ &\quad \times (G_{d'd'}^\uparrow(\tau_i, \tau_i) - G_{d'd'}^\downarrow(\tau_i, \tau_i)) \\ &\quad + G_{dd'}^\uparrow(\tau_i, \tau_i)(\delta_{dd'} - G_{d'd}^\uparrow(\tau_i, \tau_i)) \\ &\quad \left. + G_{dd'}^\downarrow(\tau_i, \tau_i)(\delta_{dd'} - G_{d'd}^\downarrow(\tau_i, \tau_i)) \right\rangle_{mc} \end{aligned} \quad (4.68)$$

In this research, we calculated the static magnetic susceptibility between two magnetic adatoms. So, above calculations were done in the imaginary time space for the magnetic correlation functions between the two impurities,

$$\chi(\tau) = \langle T_\tau M_d^z(\tau) M_{d'}^z(0) \rangle \quad (4.69)$$

Thus, we need to pass from the imaginary time to frequency space by taking the following inverse fourier transformation,

$$\chi(i\omega_n) = \int_0^\beta d\tau e^{i\omega_n \tau} \chi(\tau) \quad (4.70)$$

And the zero-frequency magnetic susceptibility is calculated by,

$$\chi(\omega = 0) = \int_0^\beta d\tau \langle M_d^z(\tau) M_{d'}^z(0) \rangle \quad (4.71)$$

4.3. Mean-Field approximation process for the Hubbard model

Before starting the process, Lieb's theorem (Lieb (1989)) is used in this method for a bipartite lattice. According to the Lieb's theorem, we define the number of spin up and down electrons in order to search ground state. So, the total spin of the system is defined by the following equation,

which $S_z = 0$ for the clean ZGNRs with PBC if $N_\uparrow = N_\downarrow$. Also, it is coupled antiferromagnetic edges and

$$S_z = \frac{|N_\uparrow - N_\downarrow|}{2} \quad (4.72)$$

Moreover, the ground state is $S_z = 0$ for the clean ZGNRs with PBC if the number of spin-up and down ($N_\uparrow = N_\downarrow$) equal to each other. Furthermore, during the mean-field calculations, Temperature are taken into account. So, Fermi-Dirac distribution is defined by,

$$f^\sigma(\varepsilon_i) = \frac{1}{1 + e^{\beta(\varepsilon^\sigma(i) - \mu^\sigma(i))}} \quad (4.73)$$

where β is inverse temperature taken as $\frac{1}{k_B T}$, k_B is Boltzmann's constant, T is temperature, ε^σ is energy of that i th particle and μ^σ is chemical potential with σ spin dependency. Additionally, μ^σ is defined by below equation,

$$\mu^\sigma = \frac{(\varepsilon^\sigma(N^\sigma) - \varepsilon^\sigma(N^\sigma + 1))}{2} \quad (4.74)$$

Starting with choosing a simple TB Hamiltonian given in the Eq.(4.1). After diagonalizing the TB Hamiltonian, we obtain its eigenvalues and eigenvectors. The obtained energy level are filled up by N_\uparrow, N_\downarrow with the Fermi Dirac distribution. After that, spin up and spin down densities are calculated by the following Eq.(4.75). Moreover, the mean occupation number can be calculated by the next Eq.(4.76). Also, N is total number of electrons,

$$\rho^\sigma(i, j) = \sum_i^N |\Psi_i^\sigma|^2 f^\sigma(\varepsilon_i) \quad (4.75)$$

$$\langle n_{i\sigma} \rangle = \text{diag}(\rho^\sigma(i, j)) \quad (4.76)$$

the U term in the Eq.(3.49) has two blocks which are spin-up Hamiltonian and spin-down Hamiltonian. As can be seen in the Eq.(3.49) the spin-up density calculated from the

Eq.(4.76) are added to the diagonal elements of the spin-down Hamiltonian. Then, same process is applied for the spin-up Hamiltonian. After diagonalizing spin-up and spin-down Hamiltonians, new spin-up and spin-down densities again are calculated. Besides, these new spin densities are used in order to find new spin Hamiltonian. Furthermore, this process is repeated itself until difference between last two energies is less than desired sensitivity.

4.4. Mean-Field Hubbard to Mean-Field Anderson Model

In this section, we have developed new model which are called mean-field Anderson model from the mean-field Hubbard model in the Eq.(3.49). So, we recall the Hamiltonian,

$$\begin{aligned}
H_{MFH} = & \sum_{\langle ij \rangle} \tau_{ij} (c_{i\sigma}^\dagger c_{j\sigma} + h.c.) + U \sum_i [(\langle n_{i\uparrow} \rangle - \frac{1}{2})n_{i\downarrow} + (\langle n_{i\downarrow} \rangle - \frac{1}{2})n_{i\uparrow}] \\
& + \frac{1}{2} \sum_{i \neq j} V_{ij} [(\langle n_i \rangle - 1)n_j + (\langle n_j \rangle - 1)n_i]
\end{aligned} \tag{4.77}$$

Our aim is to obtain the static magnetic susceptibility by using the mean-field approximation for the mean-field Anderson model. Because of that, we need to reproduce new model from above used model. The Hamiltonian consists of three terms which are the hopping term, on-site and off-site Coulomb interaction. However, during the research, off-site Coulomb interactions are not taken into account. Therefore, V_{ij} is zero. Secondly, one impurity or multi impurities could be in the system. Because of that, we derive general form of the model. So, we add another on-site Coulomb interaction for the impurity or impurities and hybridization term between the impurities and host electrons. As a results of this, new model is derived by,

$$\begin{aligned}
H_{MFA} = & \sum_{\langle ij \rangle} \tau_{ij} (c_{i\sigma}^\dagger c_{j\sigma} + h.c.) + \sum_{i,j,\sigma} (V_{ij} c_{i\sigma}^\dagger d_{j\sigma} + h.c.) \\
& U_{imp} \sum_i^{N_{imp}} [(\langle n_{i\uparrow} \rangle - \frac{1}{2})n_{i\downarrow} + (\langle n_{i\downarrow} \rangle - \frac{1}{2})n_{i\uparrow}] \\
& U_{host} \sum_i^{N_{host}} [(\langle n_{i\uparrow} \rangle - \frac{1}{2})n_{i\downarrow} + (\langle n_{i\downarrow} \rangle - \frac{1}{2})n_{i\uparrow}]
\end{aligned} \tag{4.78}$$

The first term belongs to the host electrons and τ_{ij} is effective hopping parameter between the host electrons for the graphene. Second one term is hybridization term between the impurities and host electrons. Third one is adatom term where U_{imp} is defined for the adatoms and N_{imp} is number of the impurity. The last one is the host term where U_{host} is taken for the host electrons and N_{host} is number of the host. On the other hand, there is one more thing to explain that when the Anderson model is looked in the Eq.(3.19), it has the impurity energy level which is E_d . Thus, in the Eq.(4.78), E_d term is compensated by the $\frac{1}{2}$ in the third adatom term. As a consequence of this, mean-field Anderson model was derived and is literally same with Anderson model if the last U_{host} host term is ignored.

4.4.1. Calculation of $\chi_{dd'}$ Solving Mean-Field Approximation

Here, we have obtained the mean-field Anderson model in the previous section in order to use in the mean-field approximation. So, the model was solved numerically in order to get specific ground state for AA configuration or AB configuration. First of all, we need to find ground state of the system by using the Eq.(4.72). According to the Lieb's theorem, ground state of the system will be $S_z = 0$ for clean ZGNRs if the number of spin-up and down electrons ($N_{\uparrow} = N_{\downarrow}$) equals to each other. Additionally, when two adatoms are put to the system, we have two extra electrons. Moreover, if two adatoms are located on the same AA sublattice, the new ground state will be $S_z = 1$ with two extra electrons. On the other hand, the new ground state will be $S_z = 0$ with two extra electrons if two adatoms are located on the different AB sublattice. Thus, according to these two configuration, the ground state of the system will be changed. Eventually, the system reaches the ground state at specific temperature with FD distribution. After that, we have obtained the expectation value of the two impurities for up and down electrons. During this research, two impurities are embedded to the system and performed in order to get correlation function between these two impurities. Accordingly, we marked adatoms as 1 and 2. So, their expectation values are defined by,

$$\langle n_{1,\uparrow} \rangle , \langle n_{1,\downarrow} \rangle \quad (\text{for the first adatom}) \quad (4.79)$$

$$\langle n_{2,\uparrow} \rangle , \langle n_{2,\downarrow} \rangle \quad (\text{for the second adatom}) \quad (4.80)$$

Besides, magnetization can be calculated by using above equations from the MFA,

$$m_d^{MF} = \langle n_{d,\uparrow} \rangle - \langle n_{d,\downarrow} \rangle \quad (4.81)$$

We basically try to obtain the magnetic susceptibility between two impurities by using the Green's function method. Before doing that, Feynman diagram is defined by, From the

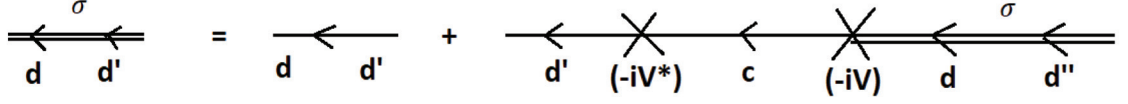


Figure 4.3. Feynman diagram for the impurity Green's function with spin dependency $G_{dd'}^\sigma(i\omega_n)$. Double lines denote $G_{dd'}^\sigma(i\omega_n)$ and single lines denote $g_c(i\omega_n)$ and $g_d(i\omega_n)$ for the non-interacting Green's functions.

above Feynman's diagram, the Dyson's equation can be obtained by,

$$G_{dd'}^0(i\omega_n) = \delta_{dd'} g_{d'}(i\omega_n) + \sum_{k,d''} g_{d'}(i\omega_n) V_{d'',k}^* g_c(k, i\omega_n) V_{k,d'} G_{d,d''}^0(i\omega_n) \quad (4.82)$$

$$G_{dd'}^0(i\omega_n) = \delta_{dd'} g_{d'}(i\omega_n) + \sum_{d''} g_{d'}(i\omega_n) \underbrace{\left\{ \sum_k |V_{d'',d'}|^2 g_c(k, i\omega_n) \right\}}_{\text{self-energy: } \Sigma(k, i\omega_n)} G_{d,d''}^0(i\omega_n) \quad (4.83)$$

In our system, there are two impurity and we will obtain the specific impurity Green's functions from the Dyson's equation,

$$G_{11}^\sigma = \frac{1}{(g_1)^{-1} - F_{11} \frac{F_{12} F_{21}}{(g_2)^{-1} - F_{22}}}, \quad G_{12}^\sigma = G_{11}^\sigma \frac{F_{21}}{(g_2)^{-1} - F_{22}} \quad (4.84)$$

$$G_{21}^\sigma = G_{22}^\sigma \frac{F_{12}}{(g_1)^{-1} - F_{11}}, \quad G_{22}^\sigma = \frac{1}{(g_2)^{-1} - F_{22} \frac{F_{12} F_{21}}{(g_1)^{-1} - F_{11}}} \quad (4.85)$$

non-interacting Green's functions for the impurities and host are defined with no hybridization. So, non-interacting Green's functions are defined by following equations,

$$g_c(i\omega_n) = \frac{1}{i\omega_n - \varepsilon_k} \quad (\text{for the host electrons}) \quad (4.86)$$

$$g_d(i\omega_n) = \frac{1}{i\omega_n - \tilde{E}_{d,\sigma}} \quad (\text{for the impurity electrons}) \quad (4.87)$$

where $\omega_n = (2n + 1)\pi T$ is Matsubara frequency with the temperature T for the fermion and $\tilde{E}_{d,\sigma} = E_d + \langle n_{d,\uparrow} \rangle \times U_{imp}$. Also, the self-energy is defined by,

$$\Sigma(k, \omega) = F_{d,d'}(k, \omega) = \sum_k |V_{d,d'}|^2 \underbrace{\frac{1}{i\omega_n - \varepsilon_k}}_{g_c(i\omega_n)} \quad (4.88)$$

According to above equations, we set up interacting Green's functions matrix,

$$G^\sigma(\omega) = \begin{pmatrix} G_{11}^\sigma & G_{12}^\sigma \\ G_{21}^\sigma & G_{22}^\sigma \end{pmatrix} \quad (4.89)$$

Eq.(4.89) is in the Matsubara frequency. Thus, we need to move to the Matsubara time by taking fourier transform of the interacting matrix,

$$G(\tau) = T \sum_{n=-\infty}^{\infty} e^{-i\omega_n \tau} G^\sigma(\omega) \quad (4.90)$$

We need to measure in the imaginary time space over one sample unlike QMC simulation by using following equation,

$$(M_d^Z(\tau)M_{d'}^Z(0)) = (d_{d\uparrow}^\dagger d_{d\uparrow} - d_{d\downarrow}^\dagger d_{d\downarrow})(d_{d\uparrow}^\dagger d_{d\uparrow} - d_{d\downarrow}^\dagger d_{d\downarrow}) \quad (4.91)$$

$$\begin{aligned} (M_d^Z(\tau)M_{d'}^Z(0)) &= \sum_{i=1}^L \left((G_{dd}^\uparrow(\tau_i, \tau_i) - G_{dd}^\downarrow(\tau_i, \tau_i)) \right. \\ &\quad \times (G_{d'd'}^\uparrow(\tau_i, \tau_i) - G_{d'd'}^\downarrow(\tau_i, \tau_i)) \\ &\quad + G_{dd'}^\uparrow(\tau_i, \tau_i)(\delta_{dd'} - G_{d'd}^\uparrow(\tau_i, \tau_i)) \\ &\quad \left. + G_{dd'}^\downarrow(\tau_i, \tau_i)(\delta_{dd'} - G_{d'd}^\downarrow(\tau_i, \tau_i)) \right) \end{aligned} \quad (4.92)$$

After getting measurement, we need to come back to the frequency space using the inverse-fourier transformation in order to find the static magnetic susceptibility by us-

ing following equation. So, the static magnetic susceptibility between two impurities is defined by,

$$\chi(\omega = 0) = \int_0^\beta d\tau (M_d^Z(\tau) M_{d'}^Z(0)) \quad (4.93)$$

4.5. RKKY Interaction

In this section, we will discuss that how two identical magnetic impurities communicate each other without any direct connections if these are embedded to specific location on the host material. First of all, we will define direct exchange interaction that conduction electrons of the host atoms communicate with each other due to overlap of charge distribution of ions as seen in the Fig.(4.4)**a**. Secondly, another one is indirect exchange interaction between two magnetic adatoms as seen in the Fig.(4.4)**b**. The magnetic moment of nucleus of first adatom scatters a conduction electron with spin. Additionally, interaction between electron and nuclear magnetic moment is hyperfine. Then, the magnetic moment of nucleus of second adatom feels that scattered electron with spin. Thus, the two magnetic adatoms indirectly see each other. As a result of this, this interaction first was studied in a metal host known as the Ruderman-Kittel-Kasuya-Yosida (RKKY) interaction (Ruderman and Kittel (1954); Kasuya (1956); Yosida (1957)). A few recent work (Kogan (2011); Sherafati and Satpathy (2011b)) have shown that decay of RKKY interaction is proportional to R^{-3} in the graphene, where R is the distance between two magnetic impurities

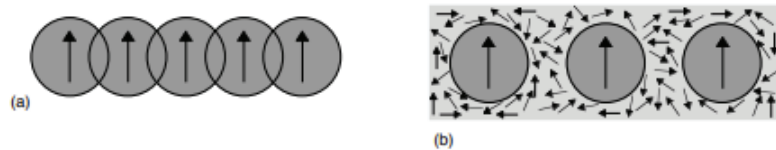


Figure 4.4. Schematic demonstration of **(a)** direct exchange and **(b)** indirect exchange. (Reprinted from the source (Ashcroft and Mermin (1976)))

In particular, effects and behaviours of the interaction has been searched in terms of shape of the host, impurity type (Black-Schaffer (2010b,a); Bunder and Lin (2009);

Hwang and Das Sarma (2008); Klinovaja and Loss (2013); Lee et al. (2012)) and different configurations of impurities (Uchoa et al. (2011); Sherafati and Satpathy (2011a); Dugaev et al. (2006); Saremi (2007); Brey et al. (2007)).

$$J_{AA} = -C \frac{1 + \cos[(K - K') \cdot R]}{(R/a)^3} \quad (4.94)$$

$$J_{AB} = 3C \frac{1 + \cos[(K - K') \cdot R + \pi - 2\theta_R]}{(R/a)^3} \quad (4.95)$$

where $C = 9\lambda^2\hbar^2/256\pi t$, K and K' is reciprocal lattice vector.

To sum up, during the research, we have worked on ZGRNs with PBC in order to calculate the spin-spin susceptibility of two magnetic impurities by using HFQMC simulation and mean-field approximation for the two-impurity Anderson model. Thus, we obtained the results far from the edges of ZGNRs. These two models will be mentioned and compared with RKKY model that Eq.(4.94) for AA configuration and Eq.(4.95) for AB configuration was used and taken from the Ref.(Sherafati and Satpathy (2011b)). In the next chapter, we will show and explain numerical results that we obtained by using QMC simulations and mean-field approximation.

CHAPTER 5

RESULTS

In this chapter, the static magnetic susceptibility χ_{12} between the two magnetic adatoms will be investigated for both the two-impurity Anderson model in the Eq.(3.19) and the mean-field Anderson model in the Eq.(4.78). These models were solved by using HFQMC algorithm and mean-field approximation, respectively. Then, we will explain these main models in two separated subtitles which are QMC measurements and MFA measurements. Moreover, ZGNRs consist of 10516 host carbon atoms and 22 zigzag edges ($W = 44$). Also, there are only two magnetic impurities on the ZGNRs.

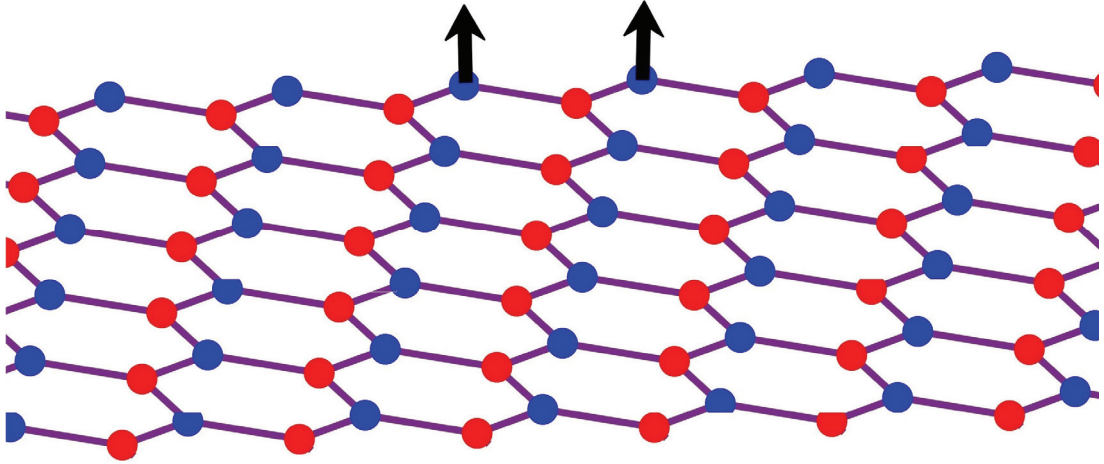


Figure 5.1. Representation of two magnetic impurities which are randomly located on the zigzag graphene nanoribbons.

Before beginning to explain results, we need to be more clear about a few things what we used in this thesis. As seen in the Fig.(5.1), two magnetic impurities are added to specific locations. Then, measurements are done in order to get the magnetic susceptibility between these two adatoms. Moreover, as seen in the Fig.(5.2)(c), one adatom is fixed at A_0 point and marked by black circle. Then, the other one is located at A_1 . So, the magnetic susceptibility was calculated at $R/b = 1$ where R is distance between two magnetic adatoms. Then, second adatom was moved to right lattice site. Again, the magnetic susceptibility was measured at $R/b = 2$ for these two adatoms. As a conse-

quence of this, that process was repeated one by one until 9^{th} carbon atom that is shown as A_9 . Moreover, as in the Fig.(5.2)(c), these correlation groups are called as *Chain*. Namely, *Chain1* is located on the middle of the ZGNRs. Then, when these correlation groups are located on the edge of ZGNRs, all they are called as *Chain11* as seen in the Fig.(5.2)(a). On the other hand, these calculations are done for different sublattices of the ZGNRs which are AA , BB and AB . Also, in the Fig.(5.2)(a), we show the ZGNR with PBC what we work on. Moreover, we marked two ends as y and y' that are connected with each other.

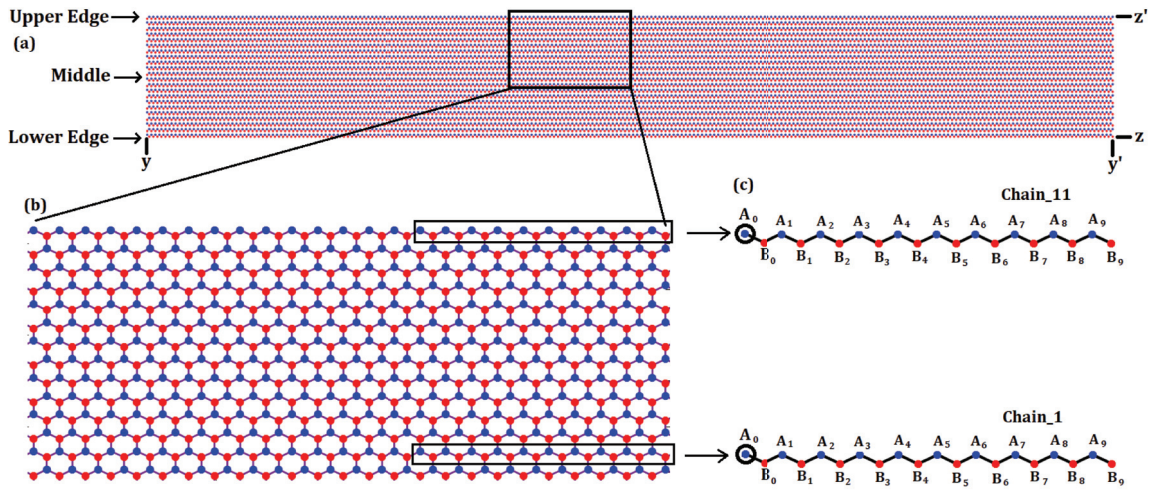


Figure 5.2. (a) Demonstration of ZGNR with PBC what we use in this research and consists of 10516 host atoms and it is showed middle, upper and downer edge. (b) it is zoomed in specific location on Figure (a). (c) we focus on specific areas in middle and upper edge of the graphene and two black rectangle which are *Chain1* and *Chain11*

During this research, the measurements was done on upper-half of ZGNRs as seen in the Fig.(5.2)(b). On the other hand, as seen in the Fig.(5.3)(a), another important point is all $A_0 - A_1$ calculations which belong to all *Chains*. Then, as seen in the Fig.(5.3)(b), all calculations are plotted by blue that is called as $R1$. On the other hand, all $A_0 - A_2$ calculations are plotted by red that is called as $R2$. As a results of this, we do these calculations in order to comprehend how all $A_0 - A_{1,2,\dots}$ calculations are changed at each R/b position when all correlation groups are moved from the middle to edge of the ZGNRs.

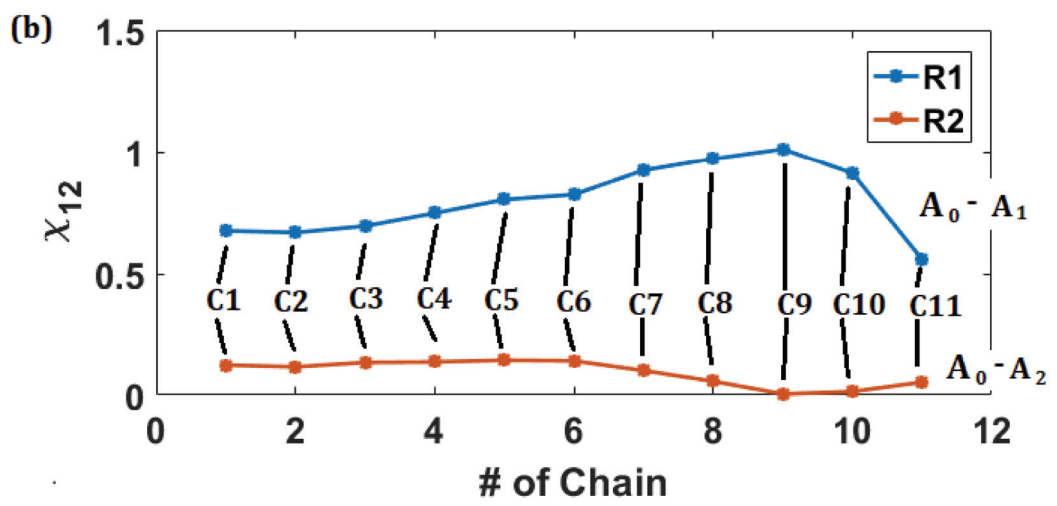
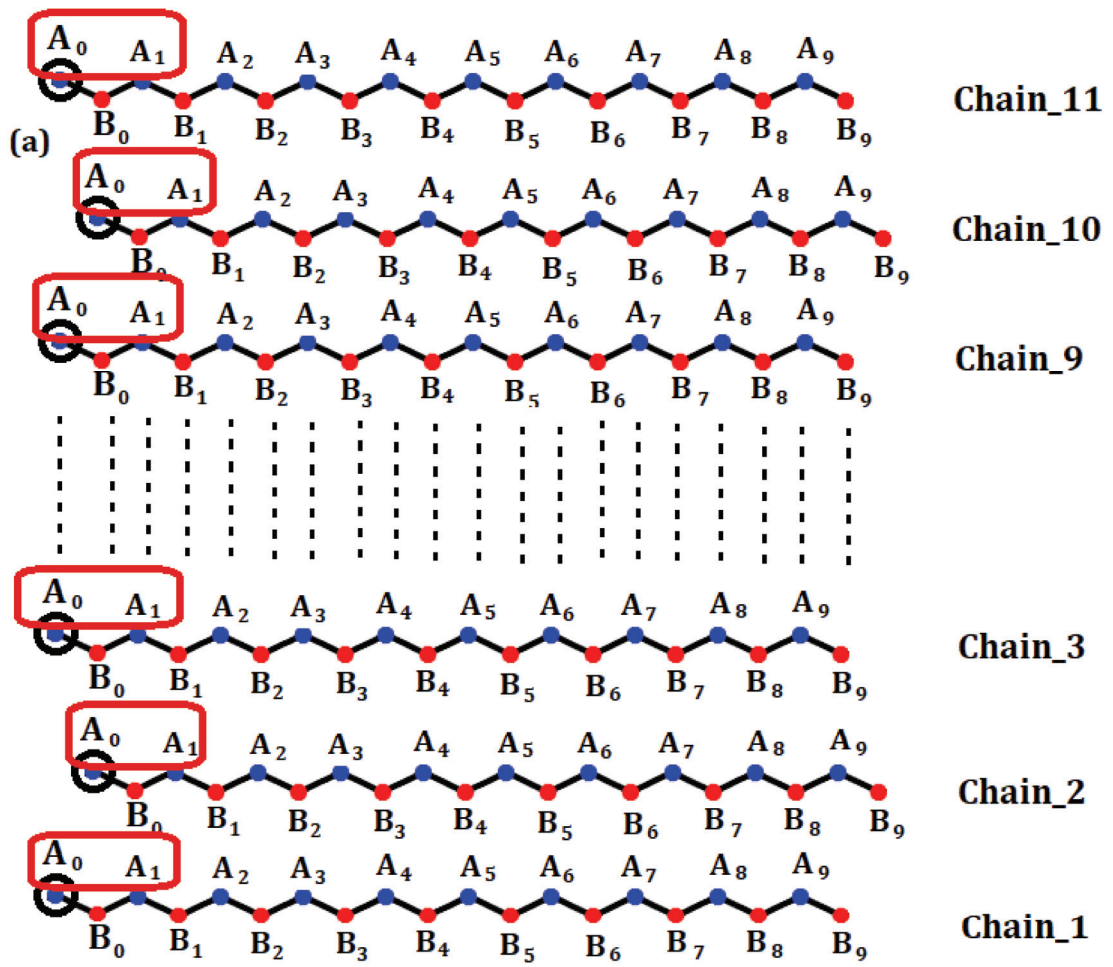


Figure 5.3. (a) Indicating of all chain we have and their first calculations are marked by red ($A_0 - A_1$). (b) Just representation of χ_{12} versus number of Chains

5.1. Results for Quantum Monte Carlo Measurements

In this section, we will indicate all QMC results. Before doing that, each QMC simulations have been performed using the Anderson Hamiltonian (3.19) for 10^4 warm up and 10^6 measurement sweeps and done 10 times which is number of simulations. Also, we need to define some certain constants which are energy level of the impurities taken as $E_1 = -1.2eV (-0.4t)$ for the first impurity and $E_2 = -1.2eV (-0.4t)$ for the second impurity, the on-site Coulomb repulsion taken as $U = 2.4eV (0.8t)$, chemical potential taken as $\mu = 0$ in units of t^{-1} , the size of the time step taken as $\Delta\tau = 1$ in units of t^{-1} and inverse temperature $\beta = L\Delta\tau$ expressed in terms of t^{-1} . Moreover, during QMC simulations, inverse temperatures are taken as $\beta = 16, 32$ and 64 which correspond to $T = 2177K, 1087K$ and $544K$, respectively. As we have mentioned before, all QMC simulations have been performed in terms of t^{-1} ($t = 3eV$).

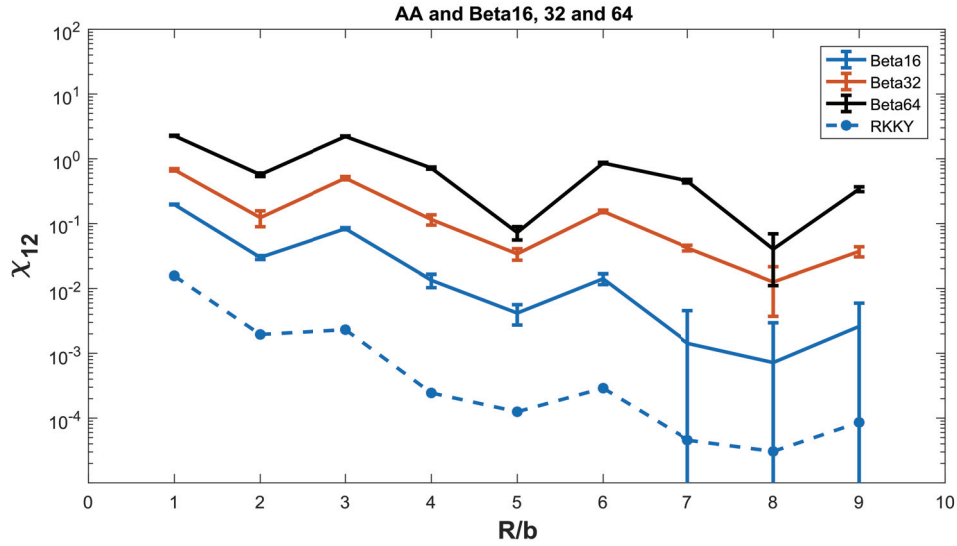


Figure 5.4. The static magnetic susceptibility between two magnetic impurities along the zigzag direction as a function of distance for the *AA* sublattice and *Chain1* which is located on the middle of ZGNRs. The solid lines are obtained by QMC simulations for different inverse temperature β . The dashed line is the RKKY results obtained from Ref.(Sherafati and Satpathy (2011b)). All results are ferromagnetic.

The static magnetic susceptibility is calculated by using Eq.(4.71) between two magnetic impurities along the zigzag direction as a function of distance (in units of the second nearest neighbour distance b). Moreover, these adatoms are located on the *AA*

sublattice which is blue carbon atom, the BB sublattice which is red carbon atom (impurities on the same sublattice) and the AB sublattice which is blue and red carbon atom (impurities on the opposite sublattice) as shown in the Fig.(5.1). Also, two impurities are located far from the edges. As seen in the Fig.(5.2) they are located in the middle of ZGNR. Moreover, as we have mentioned before, these correlation groups are called as $Chain1$. Besides, QMC calculations are obtained for different inverse temperature β and the analytical RKKY results, using these both Eqns.(4.94) for the AA sublattice and (4.95) for the AB sublattice and obtained from Ref.(Sherafati and Satpathy (2011b)), are showed with the dashed lines for the both figures in order to compare to QMC results. We begin to examine with Fig.(5.4),Fig.(5.5) and (5.6). For the AA and BB configurations (Fig.(5.4) and Fig.(5.5), respectively.), QMC results are consistent with RKKY results in terms of FM behaviour (positive susceptibility). Moreover, results of QMC simulation shows same Fermi oscillations (Saremi (2007)) with maxima at every $(3 + 3n)th$ A or B atom like RKKY results. On the other hand, although QMC simulations was done for two different sublattices, Fig.(5.4) for AA and Fig.(5.5) for BB show same behaviour. However, when temperature is decreased (inverse temperature is increased), the correlations is diverged from the RKKY results. So, at low temperature, the magnetic susceptibility becomes more important.

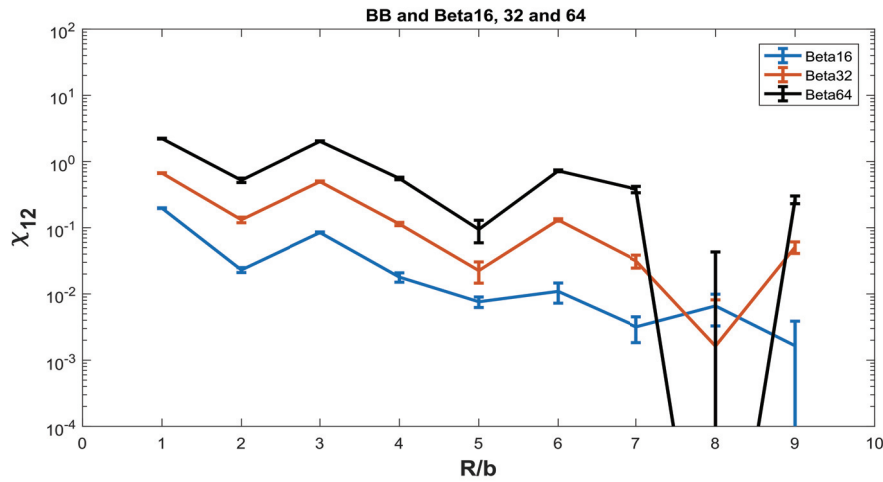


Figure 5.5. The static magnetic susceptibility between two magnetic impurities along the zigzag direction as a function of distance for the BB sublattice and $Chain1$ which is located on the middle of ZGNRs. The solid lines are obtained by QMC simulations for different inverse temperature β . The dashed line is the RKKY results obtained from Ref.(Sherafati and Satpathy (2011b)). Also, all results show same ferromagnetic behaviour.

On the other hand, same observations can be interpreted for the AB configuration (Fig.(5.6)), QMC simulation results that show AFM behaviour are same with the RKKY results (negative susceptibility). Moreover, QMC results have Fermi oscillations with minima at every $(2 + 3n)th$ B atom along the zigzag AB direction like RKKY results. However, when the temperature is decreased (β is increased), the QMC results diverge from the RKKY results like the AA and BB results. As a results of this, for the three cases which are AA, BB and AB , QMC results agree with RKKY results at high temperatures. Furthermore, the oscillations decay as R^{-3} . Besides, when the temperature is decreased, the magnitude of the static magnetic susceptibility is strongly enhanced at each sublattice configurations. On the other hand, although ZGNRs has finite system size, all results agree with the bulk graphene results in the literature (Guclu and Bulut (2015)).

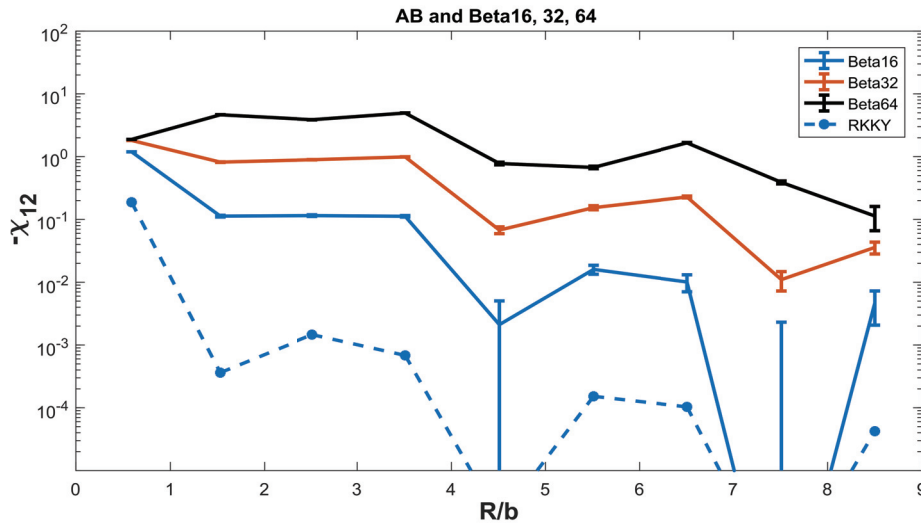


Figure 5.6. The static magnetic susceptibility between two magnetic impurities along the zigzag direction as a function of distance for the AB sublattice and $Chain1$ which is located on the middle of ZGNRs. The solid lines are obtained by QMC simulations for different inverse temperature β . The dashed line is the RKKY results obtained from Ref.(Sherafati and Satpathy (2011b)). Also, all results show same antiferromagnetic behaviour.

5.1.1. All Chains from the Middle to Edge of the ZGNR

In this section, we will examine all $Chains$ results from the $Chain1$ located on middle to the $Chain11$ on edge of ZGNR for the specific inverse temperature. However, we will show only $Chain1, 3, 6, 9$ and 11 results for simplicity. Moreover, we plot all

results into two groups which are solid lines and dashed lines in order to comprehend differences between them. Namely, the solid lines belong to *Chain1* and *Chain11* and the dashed lines belong to *Chain3*, *Chain6* and *Chain9*.

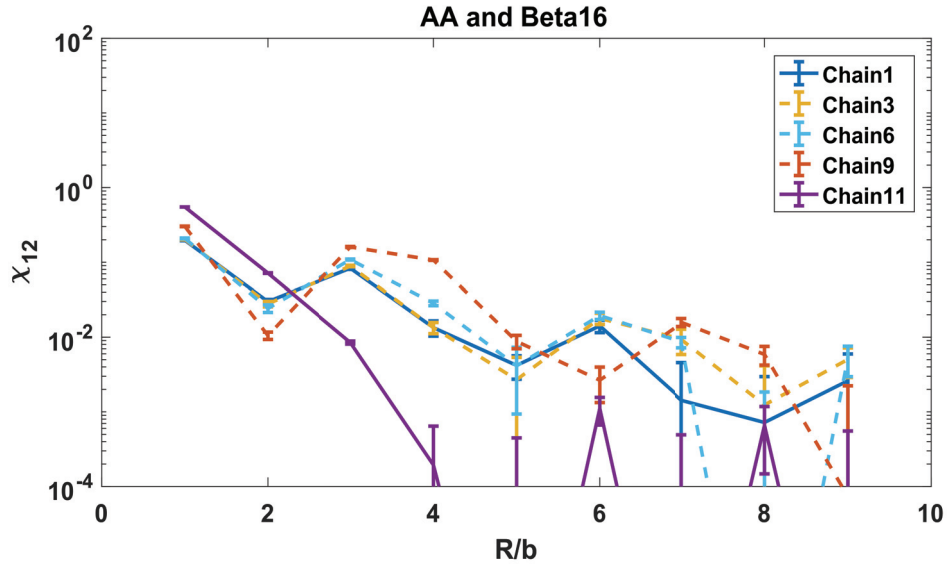


Figure 5.7. The static magnetic susceptibility between two magnetic impurities along the zigzag direction as a function of distance for the *AA* sublattice. The solid lines and dashed lines are obtained by QMC simulations for the one specific inverse temperature $\beta = 16$. All results show same ferromagnetic behaviour. Also, *Chain1* and *Chain11* are located on the middle and edge of ZGNRs, respectively.

In the Fig.(5.7), when the correlation groups are close to zigzag edges, the magnetic susceptibility as a function of distance between the two impurities are changed. The locations of adatoms where they are far from edges or on the edges, significantly affect the spin susceptibility. On the other hand, all QMC results show same Fermi oscillations and FM behaviour except *Chain11* that is located on the edges. Furthermore, in the *Chain11* that is purple one in the Fig.(5.7), major changing appears that there is no Fermi oscillation. Also, at shortest R distance, when *Chain1* and *Chain11* are compared, magnitude of *Chain11* is significantly enhanced.

On the other hand, in the Fig.(5.7), we focus on each R distance such as $R/b = 1$. Moreover, we need to obtain more information about how correlation groups at all R/b are affected when two impurities are close to the edges. As seen in the Fig.(5.8), the magnetic susceptibility as a function of number of chains is obtained for the $\beta = 16$. According to these results, the magnetic susceptibility are same for each graph exclude

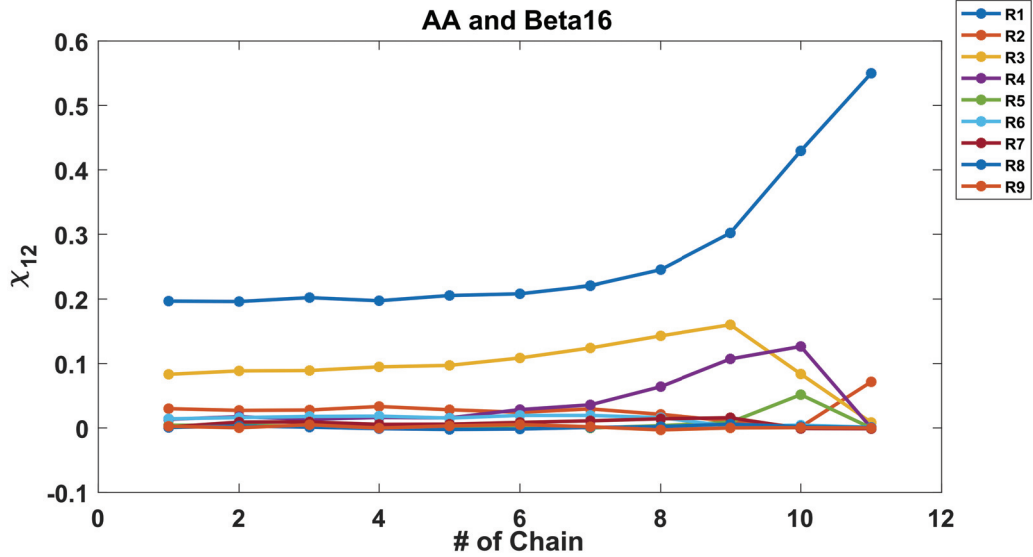


Figure 5.8. The static magnetic susceptibility between two magnetic impurities along the zigzag direction as a function of number of chains for the AA sublattice. The solid lines are obtained by QMC simulations for inverse temperature $\beta = 16$. All results show same ferromagnetic behaviour.

$R1$ ($R/b = 1$, blue one) that is dramatically increased. However, interpretation of this results are still difficult without observing other results.

In the Fig.(5.9), we will examine the AA configuration for $\beta = 32$. When correlation groups are close to the edges, the static magnetic susceptibility is significantly affected. On the other hand, as seen in the Fig.(5.10), remarkable results are appeared at the specific R distance which are $R1$ ($R/b = 1$, blue one), $R3$ ($R/b = 3$, yellow one) and $R4$ ($R/b = 4$, purple one). When adatoms are close to the edges, the spin susceptibility firstly is increased. Then, correlations are dramatically decreased. Because of that, we need to examine energy spectrums of $Chain1$ and $Chain11$ by marking two impurity states. As seen in the Fig.(5.11)(a), two impurity states marked as red and zero energy edge states are hybridized with each other at Fermi level for $Chain1$. Moreover, As seen in the Fig.(5.11)(b), two impurity states are located away from edge states for $Chain11$. Namely, impurity states and edge states are not hybridized with each other anymore. According to obtained information, when impurity states are hybridized with edge states, the magnetic correlations is significantly enhanced. Moreover, when these impurity states start to be separated from edge states, the correlations is suddenly decreased.

In the Fig.(5.12)(a), we will observe the AA configuration for $\beta = 64$. Same effects are occurred like $\beta = 16$ and 32 results. Thus, when correlation groups are

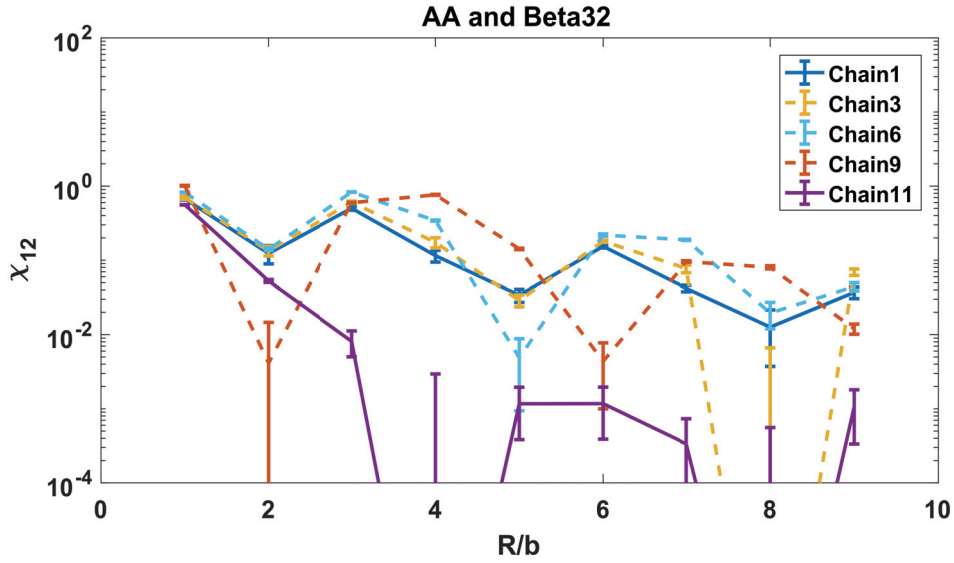


Figure 5.9. The static magnetic susceptibility between two magnetic impurities along the zigzag direction as a function of number of chains and specific distances for the AA sublattice. The solid lines and dashed lines are obtained by QMC simulations for the one specific inverse temperature $\beta = 32$. All results show same ferromagnetic behaviour. Also, $Chain1$ and $Chain11$ are located on the middle and edge of ZGNRs, respectively.

close to the edges, all QMC results show FM behaviour and Fermi oscillations. Also, for $Chain11$ which is the solid purple lines, there are no Fermi oscillations. Moreover, magnitude of the correlations is dramatically decreased by changing R distance. However, in the Fig.(5.12)(b), striking results are appeared at the specific R distances which are $R1$ ($R/b = 1$, blue one), $R3$ ($R/b = 3$, yellow one) and $R4$ ($R/b = 4$, purple one). When adatoms are close to the edges, the spin susceptibility firstly is increased. Then, the spin-spin correlations between two adatoms are rapidly decreased due to hybridization effect.

As a results of this, we have mentioned the edge effect of ZGNRs in (2.3) before, there are zero energy edge states in the ZGNRs. Furthermore, their effects are spread on the A sublattice and the upper edge of the ZGNRs as seen in the Fig.(2.7). On the other hand, as seen in the Fig.(5.11)(a) for the $Chain1$, adatom states marked by red are mixed with host atoms that are shown by blacks. Moreover, adatom states are located with the zero energy edge states at Fermi level and are hybridized with edge states. Because of that, when adatoms are close to the edges, the spin-spin correlations are positively affected. However, as seen in the Fig.(5.11)(b) for the $Chain11$, adatom states marked by red are

separated away from the zero energy states. So, there are no connection between mixed adatom states and zero energy states. Thus, when adatoms are close to the edges or on the edge sites, the spin-spin correlations of the adatoms is reduced due to the hybridization between the adatoms and edge states.

Furthermore, we have calculated at different temperatures $\beta = 16, 32$ and 64 for the BB and AB sublattices by using QMC simulation. Thanks to information of the probability density of our system as seen in the Fig.(2.8), the probability distributions are spread on A sublattice at upper half plane of ZGNRs. When two impurities are located on BB and AB sublattices, our system and the correlations of two magnetic impurities will be affected because of this information. Moreover, we will interpret these results and focus on the only $\beta = 32$ results.

We focus on the BB configuration results where both adatoms are located on the B sublattice (same sublattice). As seen in the Fig.(5.13), when adatoms are close to the edges, the static susceptibilities for the adatoms have same FM behaviour and Fermi oscillations for all *Chains* exclude *Chain11* that is the solid purple one. So, the correlations are gone at certain points for *Chain11*. On the other hand, we focus on the all particular R distances in order to comprehend very well how they are changed, internally. As seen in the Fig.(5.14), when the adatoms are close to the edges, spin-spin correlations are not affected or slowly and monotonically decreased unlike all results of AA sublattice. As a results of this, probability density distribution of the edge states are only spread on the A sublattice for upper-half of ZGNRs. Moreover, the two adatoms are located on the B sublattice. Because of that, there are no contributions to the magnetic correlations for the BB configuration.

On the other hand, we focus on results of the AB configuration where one adatom is located on the A sublattice and the other one is located on the B sublattice. As seen in the Fig.(5.15), the magnetic susceptibilities for the adatoms indicate same AFM behaviour and Fermi oscillations. Moreover, when the adatoms are close to the edges, the magnetic correlations are changed. Furthermore, for the *Chain11* which is the solid and purple one, the magnetic correlations is decreased with distance. Apparently, there is no Fermi oscillations. Now, we focus on the each particular distance in order to understand. As seen in the Fig.(5.16), the spin-spin correlations of the adatoms are significantly reduced like all BB configurations as we expected. However, this decreasing of the correlations are strikingly different then BB configurations. Because, one of adatoms sits on the B sublattice. Namely, this one are not affected much due to probability distributions on A sublattice and the other one located on A sublattice are influenced.

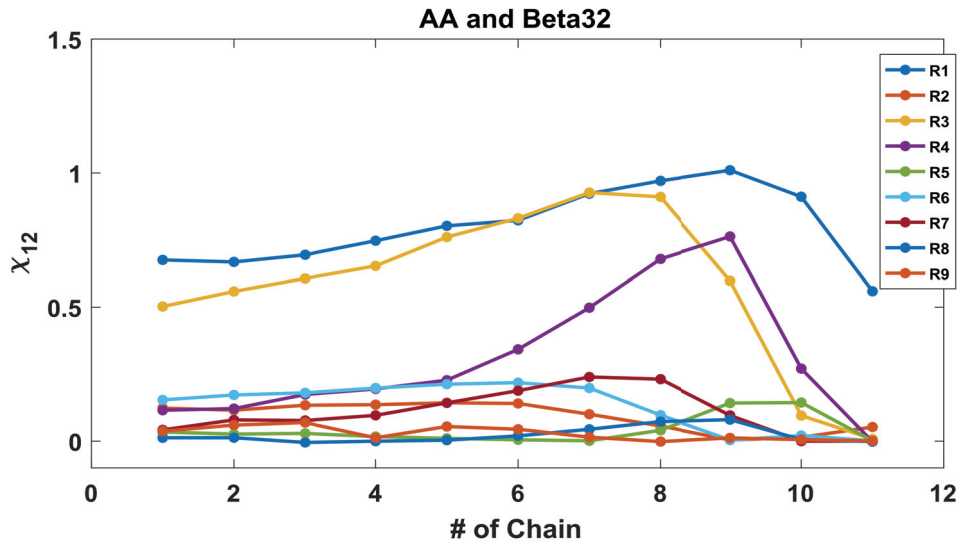


Figure 5.10. The static magnetic susceptibility between two magnetic impurities along the zigzag direction as a function of number of chains for the *AA* sublattice. The solid lines are obtained by QMC simulations for inverse temperature $\beta = 32$. All results show same ferromagnetic behaviour.

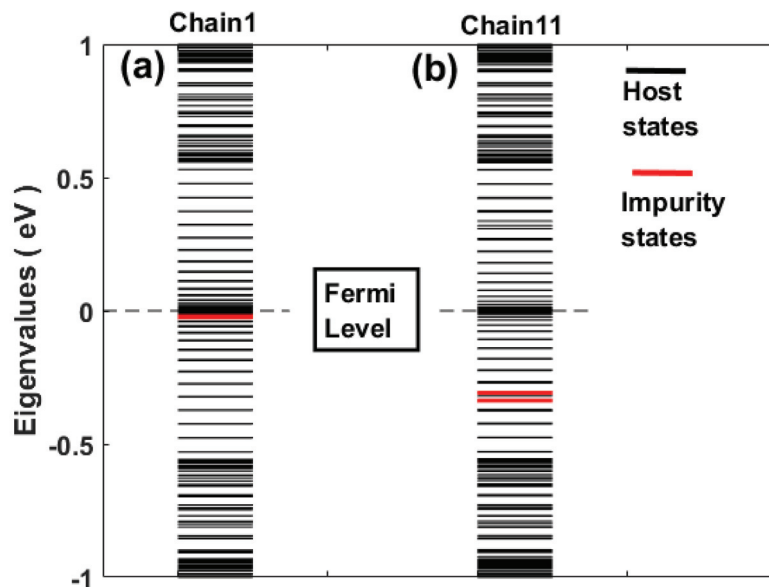


Figure 5.11. Demonstration of the energy levels of the impurities and the host atoms for (a) the *Chain1* and (b) *Chain11*

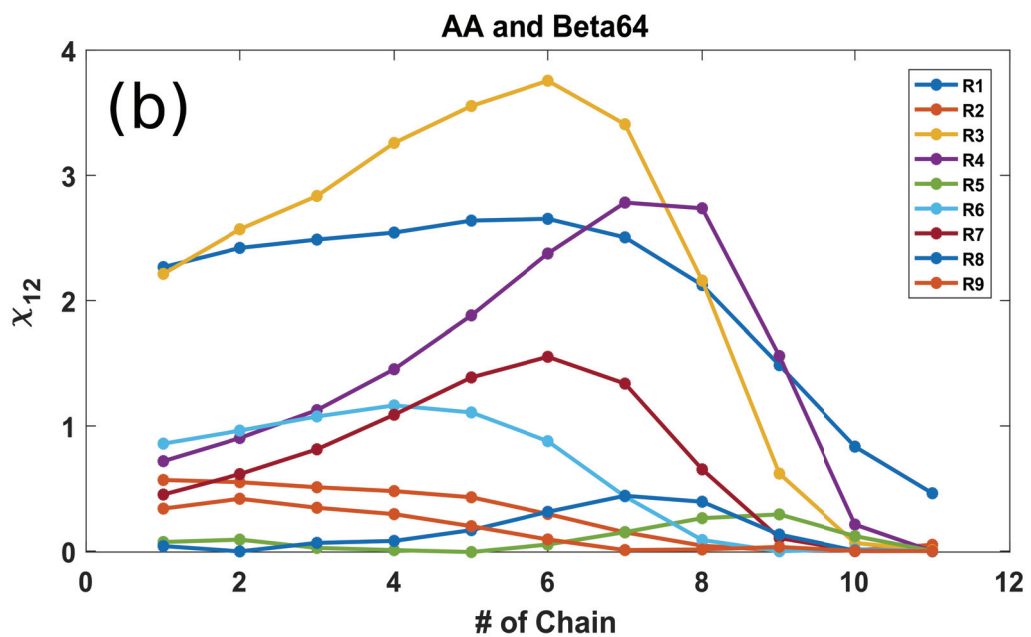
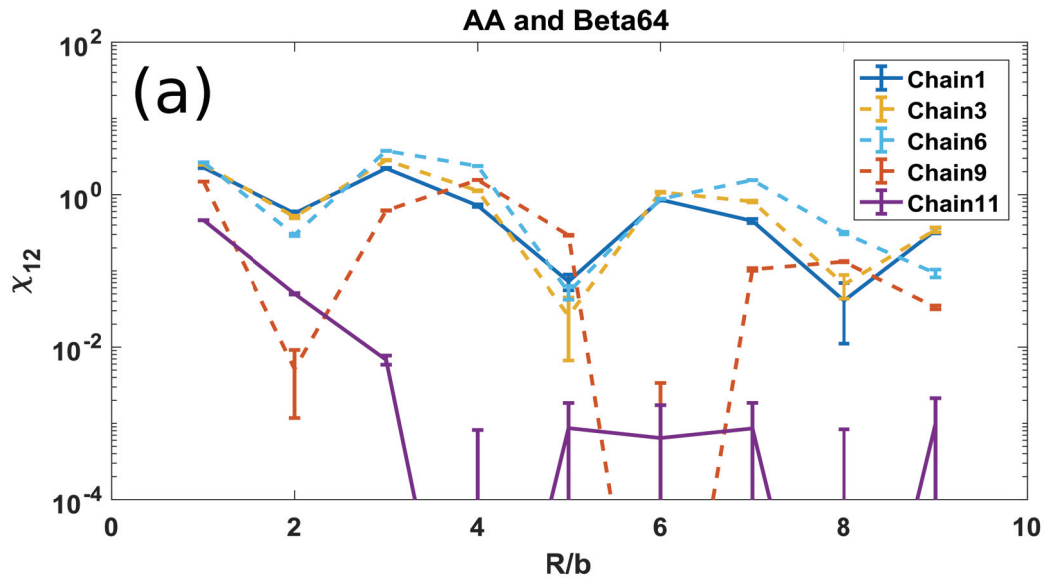


Figure 5.12. (a) The static magnetic susceptibility between two magnetic impurities along the zigzag direction as a function of distance for the *AA* sublattice. The solid lines and dashed lines are obtained by QMC simulations for the one specific inverse temperature $\beta = 64$. All results show same ferromagnetic behaviour. Also, *Chain1* and *Chain11* are located on the middle and edge of ZGNRs, respectively. (b) the static magnetic susceptibility as a function of number of chains.

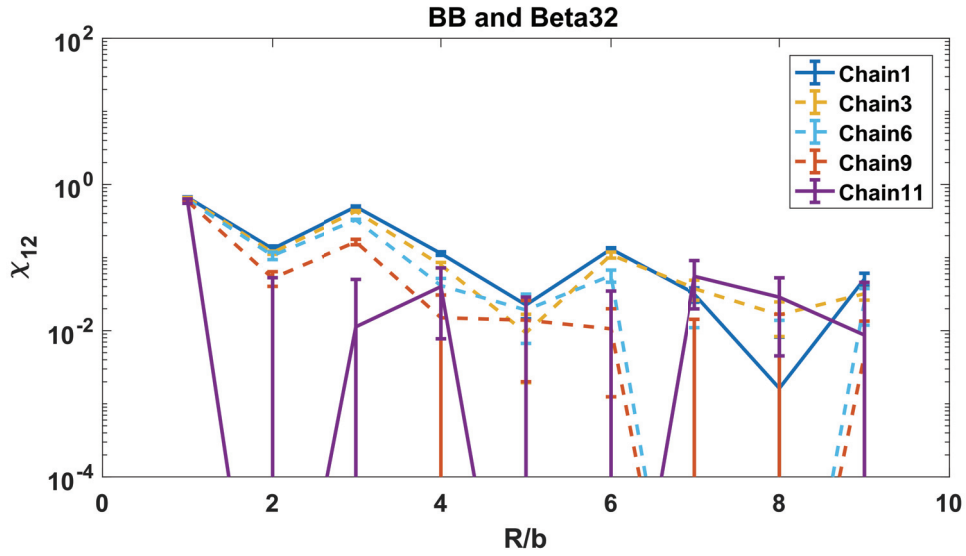


Figure 5.13. The static magnetic susceptibility between two magnetic impurities along the zigzag direction as a function of distance for the BB sublattice. The solid lines and dashed lines are obtained by QMC simulations for the one specific inverse temperature $\beta = 32$. All results show same ferromagnetic behaviour. Also, $Chain1$ and $Chain11$ are located on the middle and edge of ZGNRs, respectively.

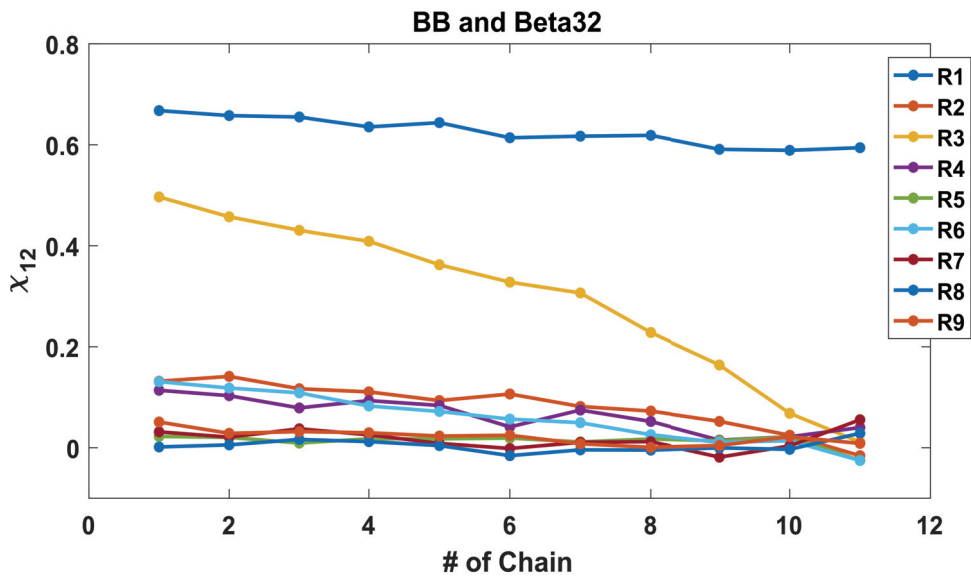


Figure 5.14. The static magnetic susceptibility between two magnetic impurities along the zigzag direction as a function of number of chains and specific distances for the BB sublattice. The solid lines and dashed lines are obtained by QMC simulations for the one specific inverse temperature $\beta = 32$. All results show same ferromagnetic behaviour. Also, $Chain1$ and $Chain11$ are located on the middle and edge of ZGNRs, respectively.

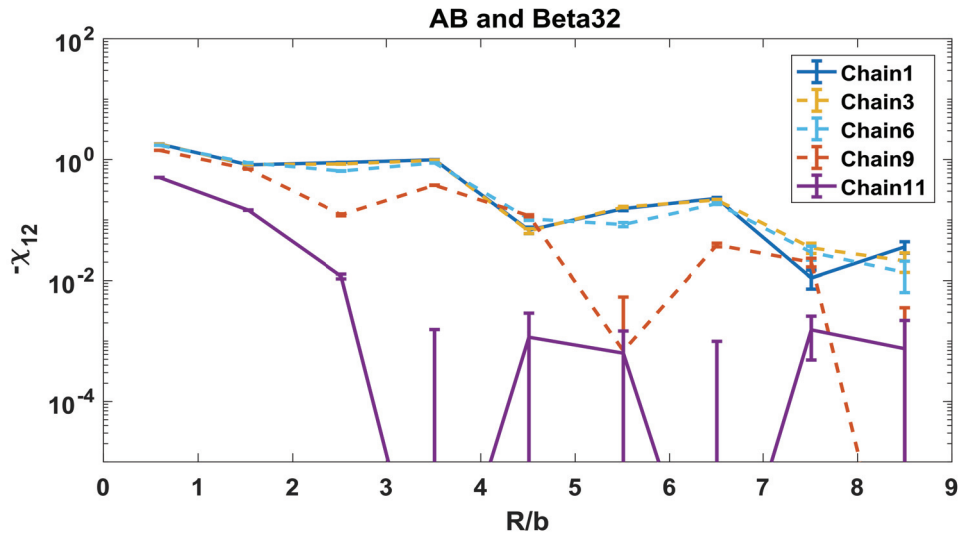


Figure 5.15. The static magnetic susceptibility between two magnetic impurities along the zigzag direction as a function of distance for the AB sublattice. The solid lines and dashed lines are obtained by QMC simulations for the one specific inverse temperature $\beta = 32$. All results show same ferromagnetic behaviour. Also, $Chain1$ and $Chain11$ are located on the middle and edge of ZGNRs, respectively.

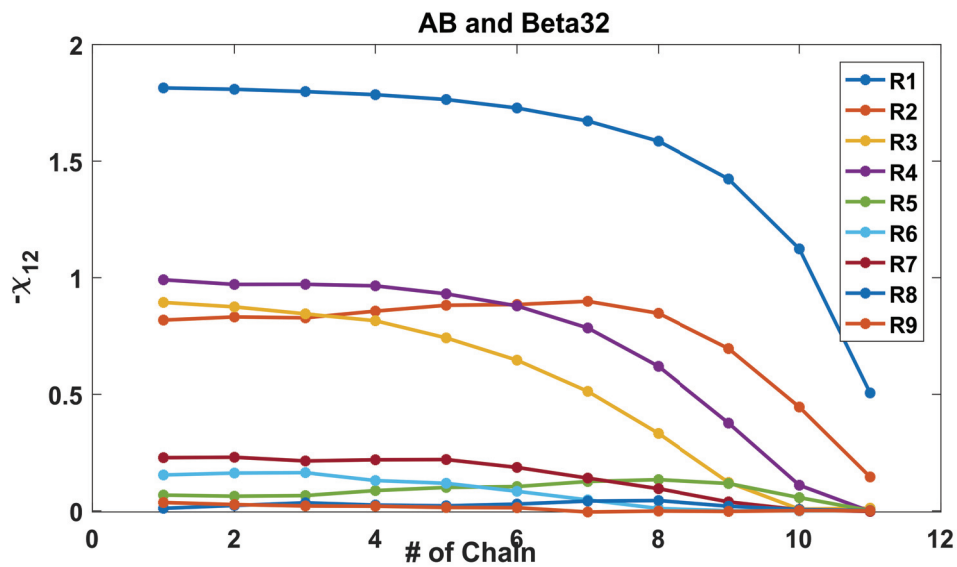


Figure 5.16. The static magnetic susceptibility between two magnetic impurities along the zigzag direction as a function of number of chain for the AB sublattice. The solid lines and dashed lines are obtained by QMC simulations for the one specific inverse temperature $\beta = 32$. All results show same ferromagnetic behaviour. Also, $Chain1$ and $Chain11$ are located on the middle and edge of ZGNRs, respectively.

5.1.2. Torus and ZGNR

The aim of this result section is to make a comparison between Torus graphene and ZGNR. As seen in the Fig.(5.2), graphene nanoribbons has two ends whcih are z and z' . Moreover, these two ends are connected with each other in order to make Torus graphene. So, as seen in the Fig.s(5.17) and (5.18), the static magnetic susceptibility between two magnetic impurities along the zigzag direction for the AA and AB sublattice, have been measured by using QMC simulations, separately.

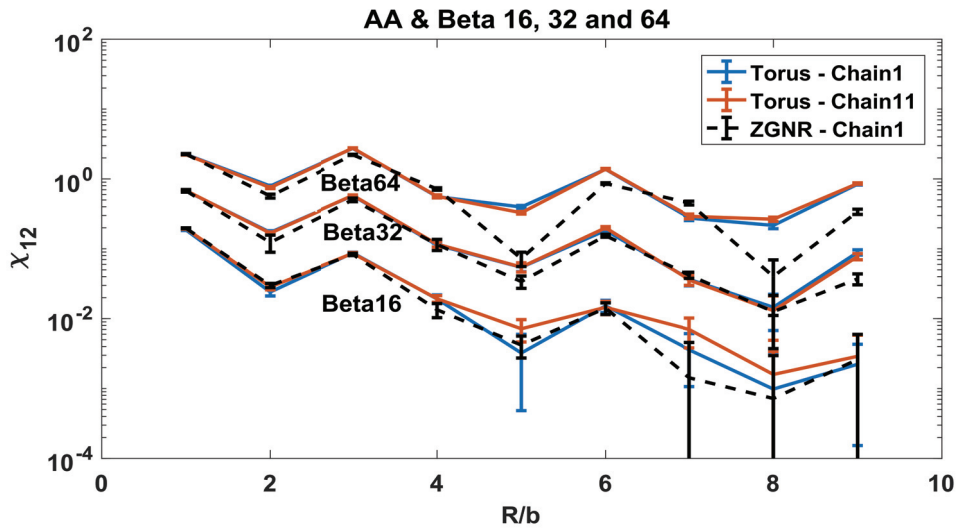


Figure 5.17. The static magnetic susceptibility between two magnetic impurities along the zigzag direction as a function of distance for (a) the AA sublattice. The solid lines and dashed lines are obtained by QMC simulations for the different inverse temperature β . Here, the dashed line belongs to the ZGNR and also, as known, our system has PBC. Besides, the solid lines shows Torus graphene it means that there are no any edges. So, there are no difference between both solid lines $Chain1$ and $Chain11$ when the shape of ZGNR is reshape to the Torus graphene.

First of all, we focus on the Fig.(5.17) for the different inverse temperature β and the AA sublattice. The solid lines are torus graphene results for the $Chain1$ that is blue line and $Chain11$ that is red line. Clearly, there are no difference between when the shape of the system is torus graphene. Besides, the correlations show same FM behaviour, Fermi oscillations and temperature dependency at the different temperature. So, when ZGNR results are added to the graphs, at the short R distance, the correlation are perfectly matched with each other although there is edge effect at ZGNR results. In addition, at the

large R values, the dashed lines which is the ZGNRs results, are slightly diverged from the other results due to the edge effect of ZGNRs. Because of that, the width of ZGNR is good enough in order to be comparable with bulk graphene.

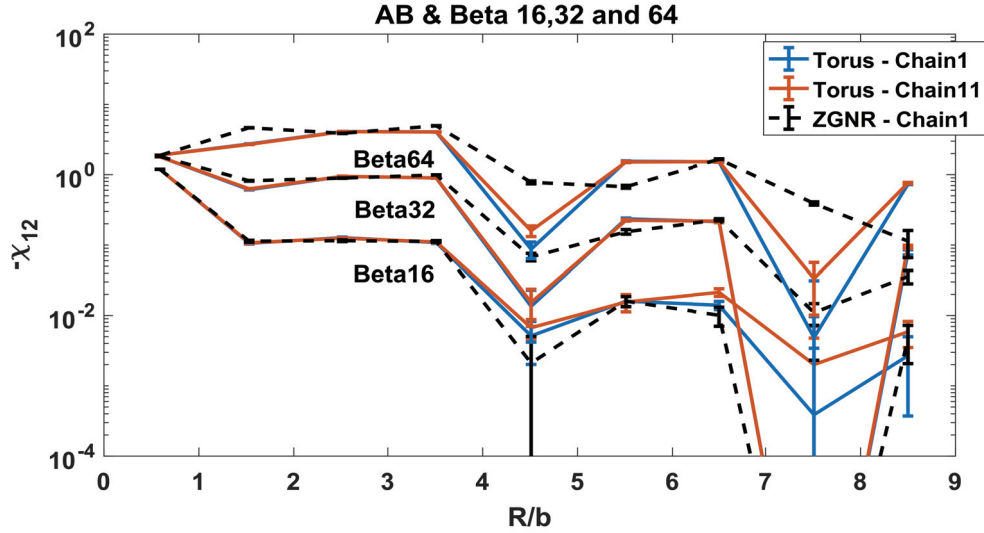


Figure 5.18. The static magnetic susceptibility between two magnetic impurities along the zigzag direction as a function of distance for the AB sublattice. The solid lines and dashed lines are obtained by QMC simulations for the different inverse temperature β . Here, the dashed line belongs to the ZGNR and also, as known, our system has PBC. Besides, the solid lines shows Torus graphene it means that there are no any edges. So, there are no difference between both solid lines $Chain1$ and $Chain11$ when the shape of ZGNR is reshape to the Torus graphene.

In addition, we turn into the AB sublattice. As seen in the Fig.(5.18), the correlations of the magnetic adatoms still show same AFM behaviour and Fermi oscillations for both results. Moreover, at short R distance, the correlations are still matched at the different inverse temperature at $\beta = 16$ and 32 . However, at the 2^{nd} R distance, the result of ZGNRs is different from the torus results for $\beta = 64$. Afterwards, at large R values, the dashed line start to be diverged from solid lines due to the edge effect. However, there are no much differences between the results. On the other hand, we can say that the magnetic correlation of ZGNR are much stronger than torus results for the $R/b = 5$ and $R/b = 8$ at given temperature. As a results of this, there are no significantly differences between Torus and ZGNRs at short R distance for both AA and AB configurations. At long range, the correlations are distinctly affected. However, there are no order of magnitudes between the correlations.

5.1.3. Changing Chemical Potential $\mu \neq 0$

Main idea is that how the system will be affected during this process if we eject the electrons from the system. In reality, we apply gate voltage to the ZGNRs. On the other hand, we theoretically change value of chemical potential in QMC simulations. So, QMC measurements will be done by changing chemical potential μ at inverse temperature $\beta = 32$ for the two-impurity Anderson model. Also, two adatoms are located on closest position for the *AA* and *AB* sublattice as can be seen in Fig.(5.1). Moreover, we did measurements by using QMC simulations for *Chain1* and *Chain11* that are located on the middle and edge of ZGNRs, respectively.

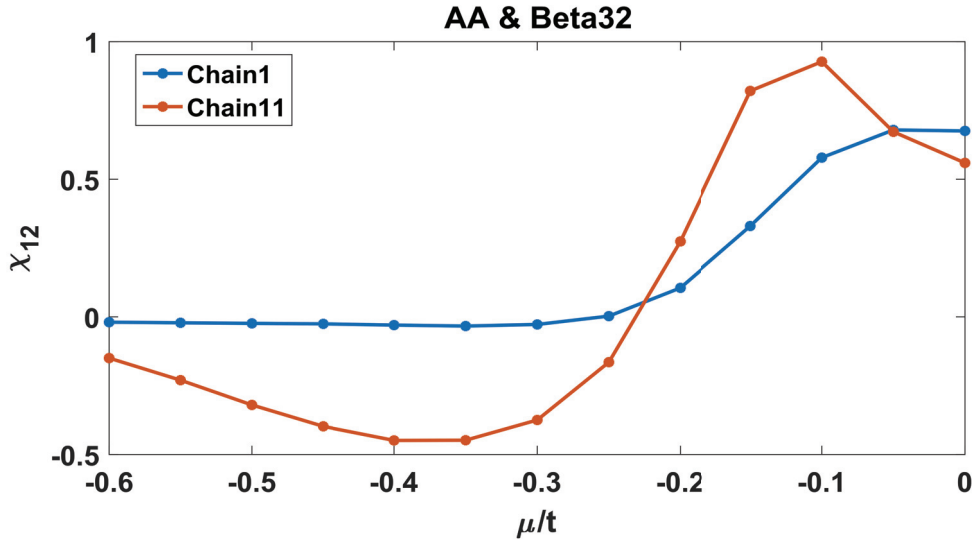


Figure 5.19. The static magnetic susceptibility between two magnetic impurities along the zigzag direction as a function of changing chemical potential μ for the *AA* sublattice shows ferromagnetic behaviour. The solid lines are obtained by QMC simulations for the inverse temperature $\beta = 32$. Also, *Chain1* and *Chain11* are located on the middle and edge of ZGNRs, respectively.

To begin with the Fig.(5.19) for the *AA* sublattice. We focus on the *Chain1* which is blue one. The correlations show FM behaviour at $\mu = 0$. When μ is slowly decreased, magnitude of the correlations start to be decreased. At $\mu = -0.25t$, FM correlation disappears for two magnetic adatoms. On the other hand, we focus on the *Chain11* which is red one and is located on the edge of ZGNRs. The correlation is FM at $\mu = 0$. At $\mu = -0.1t$, magnitude of the correlation is surprisingly increased. Then, the magnitude is decreased. Moreover, at $\mu = -0.25t$, the behaviour of the correlation

is changed from FM case to AFM case. At $\mu = -0.35t$, magnitude of AFM correlation is maximized. Furthermore, AFM correlation is slowly decreased. Then, At $\mu = -0.6t$, AFM correlation vanishes. As a results of this, when, two magnetic impurities are located on edge of ZGNRs, phase transitions can be gradually controlled from FM to AFM unlike *Chain1* calculations.

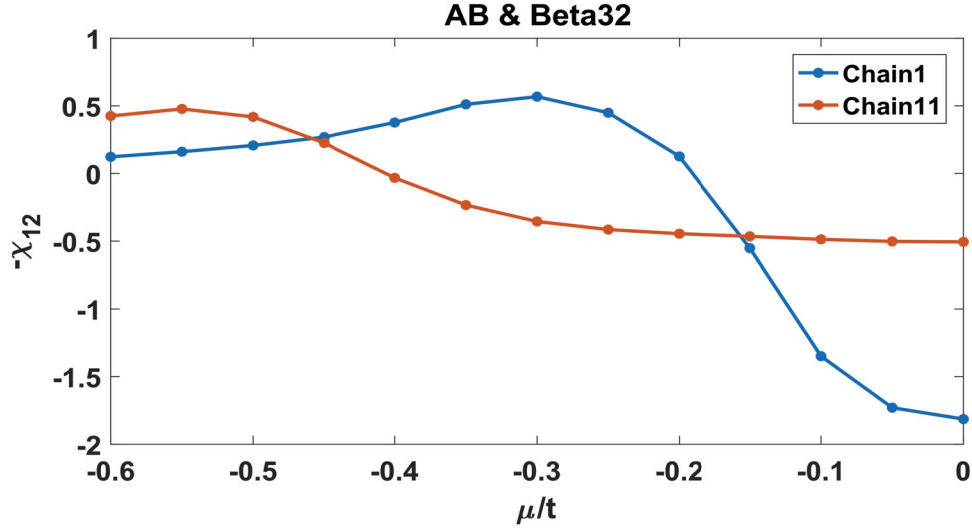


Figure 5.20. The static magnetic susceptibility between two magnetic impurities along the zigzag direction as a function of changing chemical potential μ for the *AB* sublattice shows antiferromagnetic behaviour. The solid lines are obtained by QMC simulations for the inverse temperature $\beta = 32$. Also, *Chain1* and *Chain11* are located in the middle and edge of ZGNRs, respectively.

As seen in the Fig.(5.20), we focus on the *AB* calculations which is AFM behaviour for different sublattice. For *Chain1* that is blue curve, at $\mu = 0$, AFM correlation is strongest and start to be decreased, gradually. Moreover, AFM correlation turns to FM correlations at $\mu = -0.2t$. After that, magnitude of correlation grows as μ is decreased further. Finally, at $\mu = -0.6t$ FM correlation is slightly decreased. On the other hand, we examine *Chain11* calculations which is red curve. At $\mu = 0$, AFM correlation is weaker than blue curve. Furthermore, magnitude of correlation remains same as μ is decreased, gradually. At $\mu = -0.45t$, AFM correlation begin to turn to FM correlation. Strikingly, when $\mu = -0.6t$ is decreased, strength of correlation remains same as absolute strength at $\mu = 0$. As a consequence of this, we can observe a phase transition from AFM to FM correlations.

5.1.4. Different Width of ZGNRs

In this section, we show results of changing width of ZGNRs that are obtained for the *AA* and *AB* configurations thanks to QMC simulations. Also, QMC simulations were done for only *Chain1* and *Chain11* at $\beta = 32$. During this research, actual size of ZGNR has 22 zigzag ($W = 44$ and 10516 host carbon atoms). Moreover, we erase one whole zigzag chain from the upper half of the ZGNRs which has 21 zigzag ($W = 42$ and 10038 host carbon atoms). Furthermore, size of ZGNRs is symmetrically decreased in order to obtain specific widths that are 14, 10 and 6 zigzag ($W = 28$, $W = 20$ and $W = 12$ which have 6692, 4780 and 2868 host carbon atoms, respectively.).

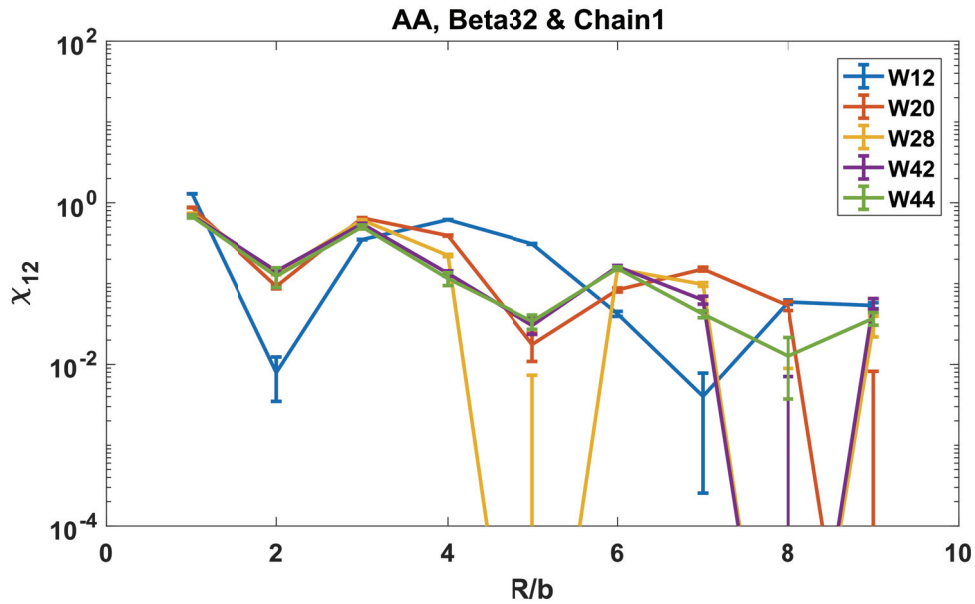


Figure 5.21. The static magnetic susceptibility between two magnetic impurities along the zigzag direction as a function of distance for the *AA* sublattice and *Chain1* is located on the middle of ZGNRs, respectively. The solid lines are obtained by QMC simulations for the inverse temperature $\beta = 32$. Besides, each separated chains belong to different width of ZGNRs $W = 12, 20, 28, 43$ and 44 and $W = 44$ is original width of our ZGNR we used in the beginning of the research.

As seen in the Fig.(5.21), when width of ZGNRs is changed, the static magnetic susceptibility is significantly affected. Moreover, the static magnetic susceptibilities between the two impurities are still FM behaviour and show same Fermi oscillations for the *AA* sublattice at $\beta = 32$ except $W = 12$ that is blue curve. Surprisingly, Fermi oscilla-

tions was supposed to be maxima at every $(3 + 3n)$ th A atom. However, new maxima is at 4 th A atom. Besides, at close R distance, all correlations have no any differences except $W = 12$. Also, at long range, correlations start to be separated from each others.

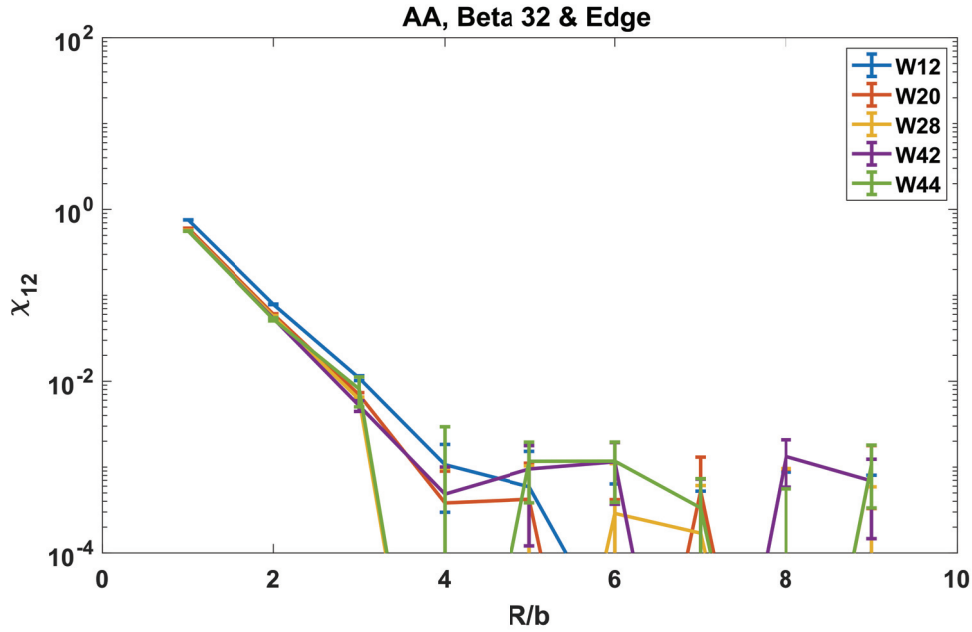


Figure 5.22. The static magnetic susceptibility between two magnetic impurities along the zigzag direction as a function of distance for the *AA* sublattice and *Chain11* is located on the edge of ZGNRs, respectively. The solid lines are obtained by QMC simulations for the inverse temperature $\beta = 32$. Besides, each separated chains belong to different width of ZGNRs $W = 12, 20, 28, 43$ and 44 and $W = 44$ is original width of our ZGNR we used in the beginning of the research.

On the other hand, as seen in the Fig.(5.22) for the *Chain11*, there are no any considerable changing at different width of ZGNRs. At short R distance, All correlations is still same. Moreover, magnitude of the susceptibility is dramatically decreased. Furthermore, at long range, the correlations are stable or disappear.

As seen in the Fig.(5.23), the static magnetic susceptibility between the two impurities have AFM behaviour and show same Fermi oscillations for the *AA* sublattice at $\beta = 32$. When width of ZGNRs is decreased, the spin-spin correlations are apparently changed. In addition, Fermi oscillation with minima at every $(2 + 3n)$ th B atom is slowly and strikingly disappeared like *AA* case and *Chain1*. As a results of this, there are no predictable Fermi oscillations at $W = 12$ that is blue curve.

When width of ZGNRs is changed, the two magnetic impurities is always located

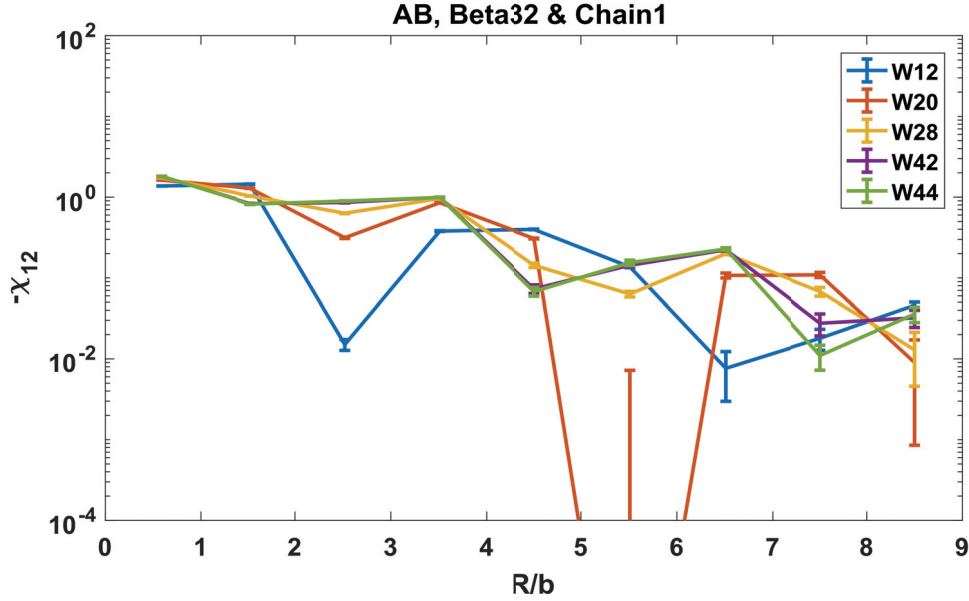


Figure 5.23. The static magnetic susceptibility between two magnetic impurities along the zigzag direction as a function of distance for the *AB* sublattice and *Chain1* is located on the middle of ZGNRs, respectively. The solid lines are obtained by QMC simulations for the inverse temperature $\beta = 32$. Besides, each separated chains belong to different width of ZGNRs $W = 12, 20, 28, 43$ and 44 and $W = 44$ is original width of our ZGNR we used in the beginning of the research.

on the edge sites. As seen in the Fig.(5.24), there are no any changing at the magnetic susceptibilities at short R distance. Beside, at long range, the correlations are still stable or vanish.

5.2. Results for Mean-Field Approximation Measurements

In this section, we have obtained the static magnetic susceptibility for two adatoms by using the mean-field approximation. We will examine and interpret results. Also, we will compare both QMC and MFA results in detail.

In the Fig.(5.25), we compare MFA and QMC results that are respectively dashed and solid lines at different inverse temperature $\beta = 16, 32$ and 64 for the *AA* sublattice. Additionally, there is an extra inverse temperature $\beta = 128$ for the MFA results. MFA and QMC results show same FM behaviour. Surprisingly, MFA results are much more stronger than QMC results. Moreover, at inverse temperature $\beta = 16$ which are the

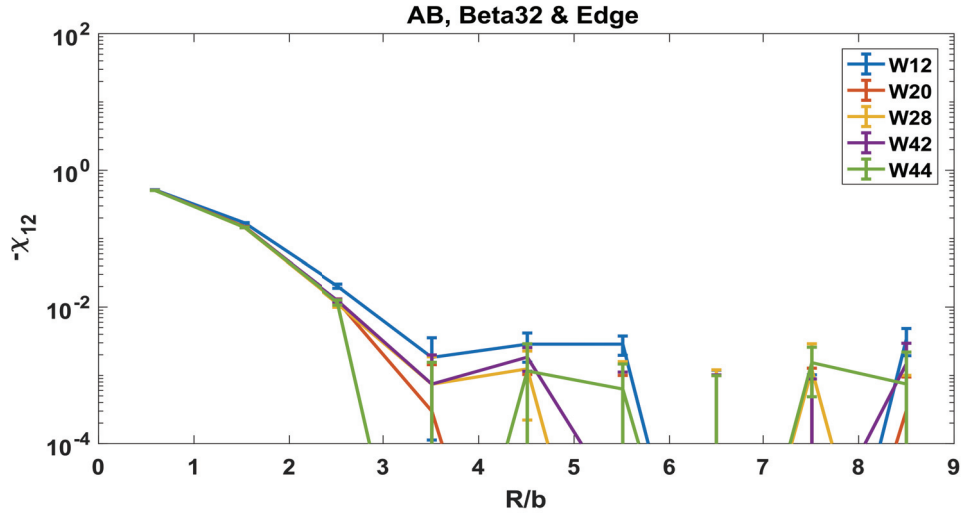


Figure 5.24. The static magnetic susceptibility between two magnetic impurities along the zigzag direction as a function of distance for the AB sublattice and $Chain11$ is located on the edge of ZGNRs, respectively. The solid lines are obtained by QMC simulations for the inverse temperature $\beta = 32$. Besides, each separated chains belong to different width of ZGNRs $W = 12, 20, 28, 43$ and 44 and $W = 44$ is original width of our ZGNR we used in the beginning of the research.

blue solid and blue dashed line, MFA and QMC results are same order of magnitude. Especially, at short R distance, MFA and QMC results indicate same Fermi oscillation. After certain short range, Fermi oscillations of dashed curve vanish. Besides, at low inverse temperature, MFA results are apparently separated from QMC results. On the other hand, when specific dashed curve that is red is zoomed, static magnetic correlations show Fermi oscillations at short R distance. Moreover, Fermi oscillation disappear like $\beta = 16$ that is dashed blue curve at long range.

On the other hand, we can say that MFA results are much stronger than QMC results. So, an important question is apparently risen. In order to answer that question, we need to research magnetization of MFA and QMC simulations by using Eq.(4.66) and Eq.(4.81). As seen in the Fig.(5.26), solid blue curve belongs to magnetization of MFA results and solid black line belongs to the magnetization of QMC results at all inverse temperature. Also, we did curve fitting for the MFA results in order to find critical temperature with red dashed curve. Clearly, we did not expect these magnetization figures for MFA and QMC results. According to obtained results in the Fig.(5.25), magnetization of MFA results would be supposed to be higher than QMC's magnetization. Apparently, the

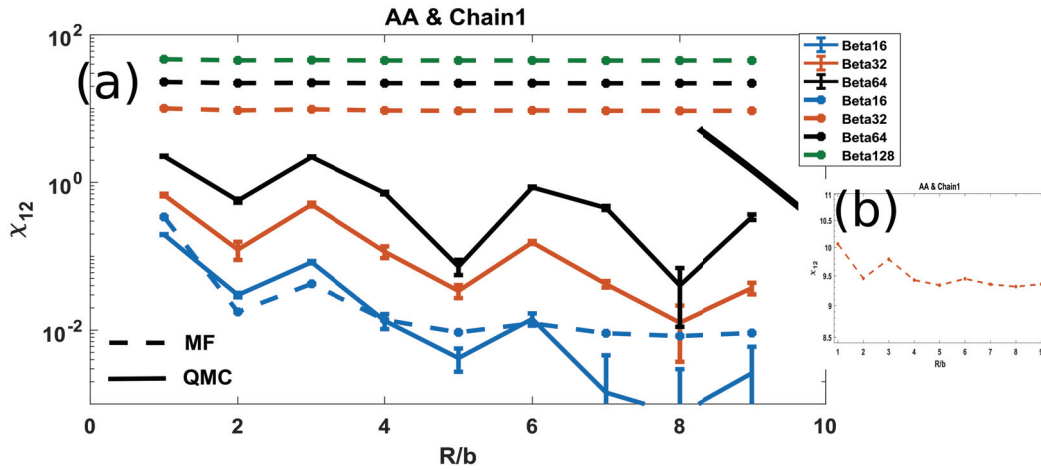


Figure 5.25. The static magnetic susceptibility between two magnetic impurities along the zigzag direction as a function of distance for the *AA* sublattice and *Chain1* is located on the middle of ZGNRs. The solid lines and dashed lines are obtained by QMC and MFA calculations for different inverse temperature β , respectively. All results show same ferromagnetic behaviour. (b) MFA and $\beta = 32$ calculation is zoomed and shown in the inset.

results of Fig.(5.26) leads us to one conclusion. As a result of this, MFA overestimates measurements of the static magnetic susceptibility.

In the Fig.(5.27) for the *AA* sublattice and *Chain11* that is located on edge of the ZGNR, the dashed lines belong to MFA results and the solid lines belong to QMC results. Significantly, MFA and QMC results are consistent with each other. Also, the static magnetic susceptibilities show same FM behaviour. Besides, Fermi oscillation for MFA and QMC results disappear. Moreover, at short R distance, magnitude of each correlation is dramatically decreased. After $R/b = 4$ distance, MFA and QMC results start to be separated from each other. Additionally, MFA results are decreased, gradually. Consequently, we need to observe magnetization of MFA and QMC in order to comprehend very well.

As seen in the Fig.(5.28), the solid blue and solid black line are MFA and QMC results, respectively, at different inverse temperature β for the *AA* and *Chain11*. Strikingly, results of QMC are still solid like magnetization result of *Chain1*. Moreover, results of the MFA are dramatically decreased at each different inverse temperature. Besides, magnetization of MFA apparently disappears. Furthermore, blue solid line remains the same for each inverse temperature at the vicinity of zero.

As seen in the Fig.(5.29), we focus on the *AB* sublattice for *Chain1* and *Chain11*. Moreover, we compare both MFA and QMC results at given inverse temperature. As seen

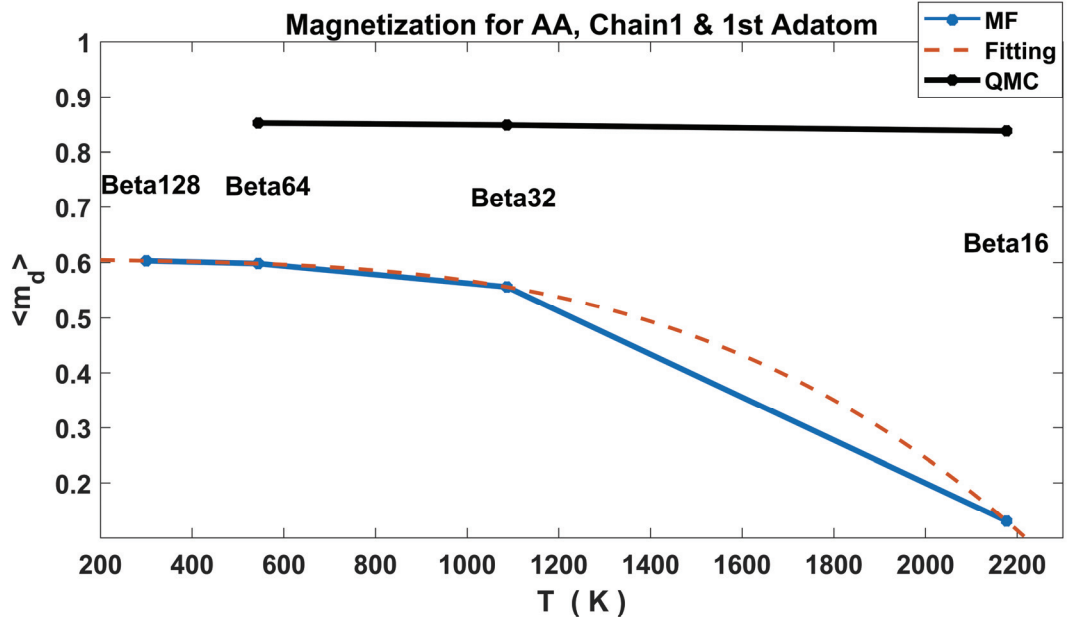


Figure 5.26. The magnetization of QMC results and MFA results as a function of inverse temperature for the *AA* sublattice, *Chain1* and 1st adatom. The blue solid line, the black solid line and the red dashed line belong to MFA results, QMC results and curve fitting of the MFA results, respectively.

in the Fig.(5.29), dashed and solid lines shows MFA and QMC results, respectively. Also, the correlations have AFM behaviour for the *AB* configuration (impurities on opposite sublattice). At inverse temperature $\beta = 16$ and short R distance, results of MFA and QMC simulations are similar with each other. Moreover, when blue solid line indicate expected Fermi oscillations at long range, dashed blue line oscillation are damped and become stable. On the other hand, there are order of magnitude between results of MFA and QMC. Moreover, results of MFA is stronger than QMC results. On the other hand, at $R/b = 1$, magnitude of first correlations of all MFA results stays under QMC results. So, as seen in the inset, two adatoms stand closest position to each other and they are affecting each other directly. Thus, this situation is frustrating the magnetic susceptibility between two adatoms.

In the Fig.(5.30), we calculated the static magnetic susceptibility between two adatoms that are located on edges of ZGNR. MFA and QMC results show same AFM behaviour. Significantly, all evidences of the Fermi oscillations are gone. Because of that, two different results are consistent with each other. Especially, at short R distance, all MFA and QMC results show same behaviour at short range and decrease, gradually. Clearly, after a certain distance $R/b = 3$, blue dashed line is separated from all other

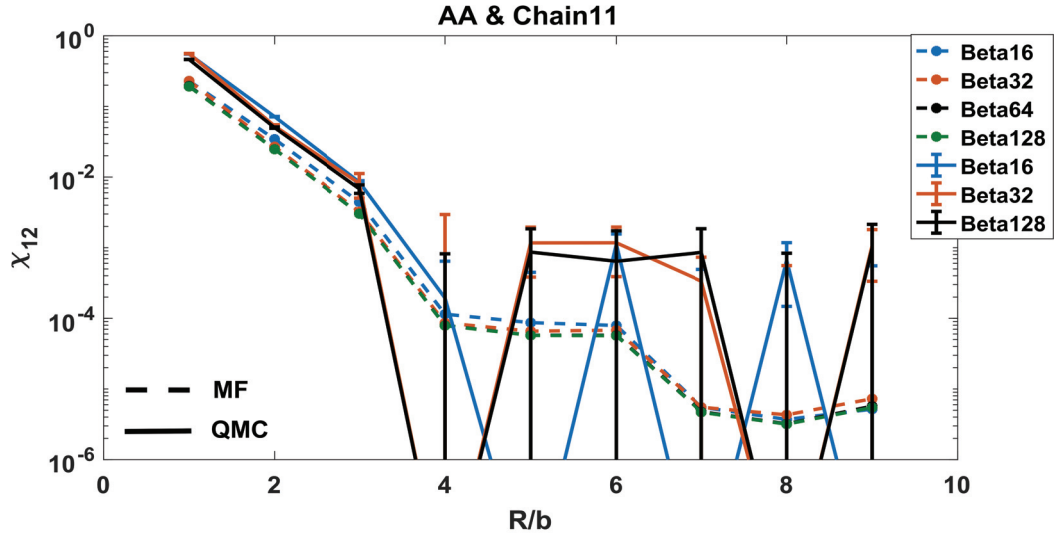


Figure 5.27. The static magnetic susceptibility between two magnetic impurities along the zigzag direction as a function of distance for the *AA* sublattice and *Chain11* is located on the edge of ZGNRs. The solid lines and dashed lines are obtained by QMC and MFA calculations for different inverse temperature β , respectively. All results show same ferromagnetic behaviour.

MFA results at low inverse temperature $\beta = 16$. On the other hand, we focus on specific that are $\beta = 32, 64$ and 128 . Apparently, all MFA results move together with minor deviations. Besides, QMC results that are solid curves, are distinctly separated from MFA results. Moreover, the correlations of QMC results disappear at some certain points.

5.2.1. Results of Different Electron-Electron Interaction Values for the Host Atoms (U_{host})

In this section, we will use mean-field Anderson Hamiltonian given Eq.(4.78) by adding the on-site Coulomb interaction term for host electrons. So, when electron-electron interactions are taken into account as $U_{host} = 0, 1, 1.5$ and 2 in units of t^{-1} for the host atoms, we will examine that how system will be affected for the *AA* and *AB* sublattice at specific inverse temperature $\beta = 32$ and 128 .

In the Fig.(5.31), we have shown the effects of the el-el interaction on the system for the *AA* sublattice, $\beta = 32, 128$ and *Chain1* is located on the edge of the ZGNR. Both separated straight line still show FM behaviour. As seen in the graph, we thought

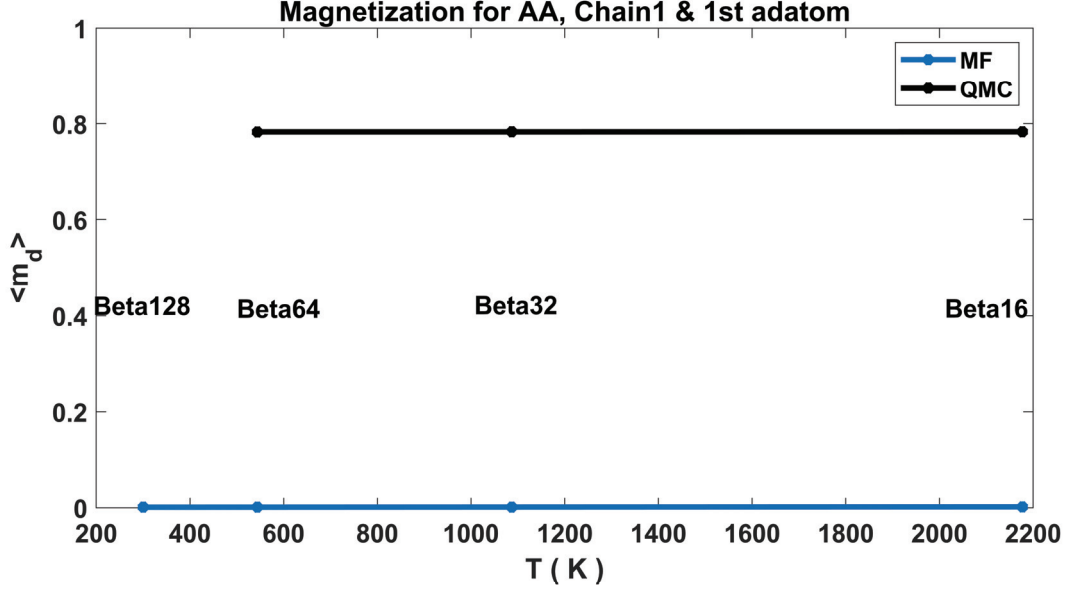


Figure 5.28. The magnetization of QMC results and MFA results as a function of inverse temperature for the *AA* sublattice, *Chain11* and 1st adatom. The blue solid line and the black solid line belong to MFA results and QMC results, respectively.

as if there were no difference between different el-el interaction values. However, when zoomed in the specific correlations for the $\beta = 32$ as shown in the below inset, all magnetic correlations corresponding to U values, are separated with minor deviations from each other as seen in the below inset. While number of U value is increased, the static magnetic susceptibility is individually raised corresponding to U values. At short distance, they also denote pronounced oscillations. Furthermore, at long range, there are no oscillatory R dependence for all results. On the other hand, there are order of magnitude between these two inverse temperatures, so, at low temperature for $\beta = 128$, the magnitude of the correlations are so strong than $\beta = 32$. However, the results of $\beta = 128$ are literally similar to the $\beta = 32$ results. As seen in the above inset for $\beta = 128$, the blue dashed line for $U = 0$ diverge a little bit from the other results, and at short R distance, all correlations act as group and show same Fermi oscillations. At the long range, they are separated from the each other. Moreover, all correlations behave same and all oscillations are gone, eventually.

In the Fig.(5.32), the results of the magnetic susceptibilities as a function of distance for the *AA* sublattice, *Chain11* is located on the edge of the ZGNR at given different inverse temperature $\beta = 32$ and 128, are shown by solid and dashed lines that show

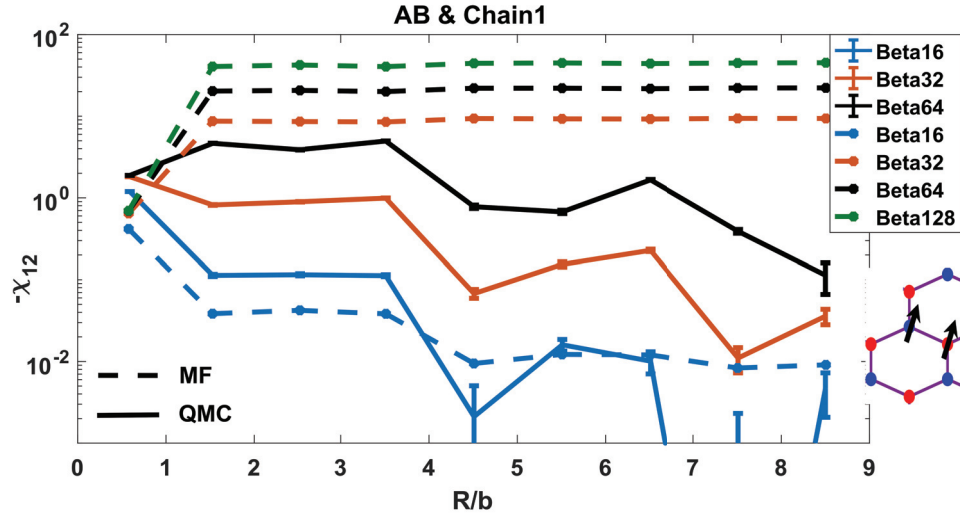


Figure 5.29. The static magnetic susceptibility between two magnetic impurities along the zigzag direction as a function of distance for the *AB* sublattice and *Chain1* is located on the middle of ZGNRs. . The solid lines and dashed lines are obtained by QMC and MFA calculations for different inverse temperature β , respectively. All results show same antiferromagnetic behaviour.

$\beta = 32$ and 128 results, respectively. When two magnetic impurities are located on the edge, the effect of el-el interaction for the host atoms, starts to occur at different U values unlike *Chain1* results, clearly. To begin with $U = 0$, both blue solid and dashed lines move together at even different inverse temperature $\beta = 32$ and 128 , and their magnitude is decreased, gradually. Moreover, there are no fermi oscillations at every R distance. On the other hand, when U is taken as 1, these both red curves differ from the both blue lines. In the beginning, both correlations start as one and after $R/b = 2$, they diverge from each other. So, at long range, the order of magnitude occurs between these red curves, and there is no Fermi oscillations. In addition, when U term is increased to next level, there are magnitude difference for the both black curves at short distance unlike the both red curves, and the stable magnitude difference of the correlations remain same, obviously. The last one is both green curves which belong to $U = 2$ value, and these curves behave same as the behaviours of both black curves, exactly. Also, there are no Fermi oscillations at long range.

Here, we turn into the *AB* configurations for *Chain1*, *Chain11* at different inverse temperature $\beta = 32$ and 128 . As seen in the Fig.(5.33), the first magnetic susceptibility is apparently frustrated due to position of two magnetic adatoms which are located

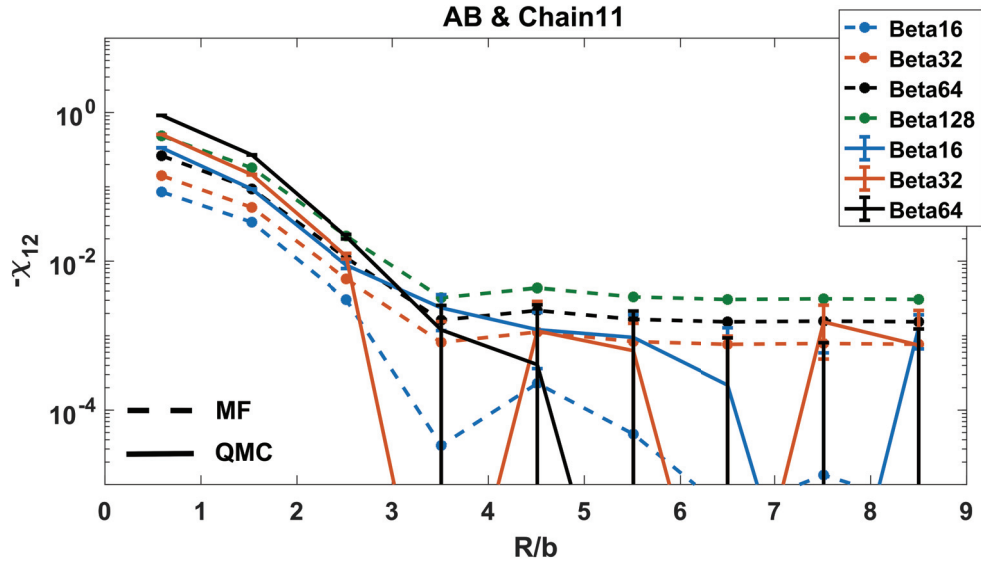


Figure 5.30. The static magnetic susceptibility between two magnetic impurities along the zigzag direction as a function of distance for the *AB* sublattice and *Chain11* is located on the edge of ZGNRs. The solid lines and dashed lines are obtained by QMC and MFA calculations for different inverse temperature β , respectively. All results show same antiferromagnetic behaviour.

on the closest opposite sublattice at $R/b = 1$. On the other hand, as seen in the Fig.(5.33), the static magnetic susceptibilities between two adatoms, have AFM behaviour and have no oscillatory R dependence, when el-el interactions for host electrons are taken into account. Moreover, after particular $R/b = 2$ distance, the magnetic susceptibility is constant in the range of R . As a results of this, there is no el-el interaction dependency for the *AB* configuration and *Chain1*.

In the Fig.(5.34), the static susceptibility are shown for the *AB* configuration and *Chain11* that is located on the edges. Evidently, these results are different from the results shown in the Fig.(5.33) due to the edge effect. On the other hand, both solid and dashed blue curves act same behaviour at different magnitude for $U = 0$ value and different inverse temperatures that are $\beta = 32$ and 128. Moreover, the correlations are dramatically decreased until a certain distance $R/b = 4$. Additionally, Fermi oscillations vanish at all R distance. Secondly, when U term is taken as 1, solid and dashed red curves have no oscillatory at all R distance. Also, the correlations are completely straight line as can be seen in the Fig.(5.34). Additionally, both solid and dashed black curves have same magnitude at all distance. Moreover, magnitude of the correlations is slightly increased

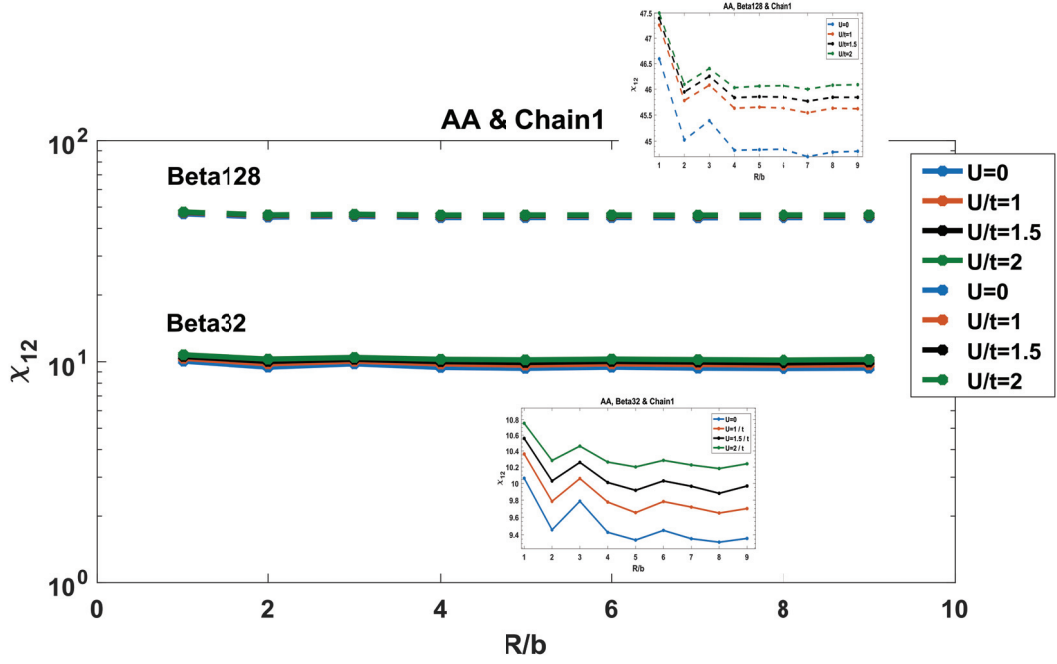


Figure 5.31. The static magnetic susceptibility between two magnetic impurities along the zigzag direction as a function of distance for the *AA* sublattice and *Chain1* is located on the middle of ZGNR. The solid lines and dashed lines are obtained by MFA calculations for different inverse temperature $\beta = 32$ and $\beta = 128$, respectively. All results show same ferromagnetic behaviour. All calculation is done for different on-site Coulomb repulsion of the host carbon atoms taken as $U_{host} = 0, 1, 1.5$ and 2 in units of t^{-1} .

and constant at long range. Furthermore green solid and dashed curves act same like black curves. Their magnitude of susceptibilities is lightly risen and remain constant at long range, distinctly.

To sum up, we have observed, examined and interpreted all results that are obtained by using the quantum Monte Carlo algorithm and the mean-field approximation for two magnetic adatoms on zigzag graphene nanoribbons. When the impurity adatoms are located far from edges, the results we obtained are consistent with the bulk graphene results in the literature for QMC results. Moreover, the specific location and orientation of adatoms on the sublattices, significantly affect the spin-spin correlations of the two impurities. Besides, we observe that phase transition can be controlled by changing chemical potential. On the other hand, results of mean-field approximation significantly differ from quantum Monte Carlo results. Furthermore, when the electron-electron interactions of the host atoms are considered, significant differences are obtained. In the conclusion, we will discuss again briefly.

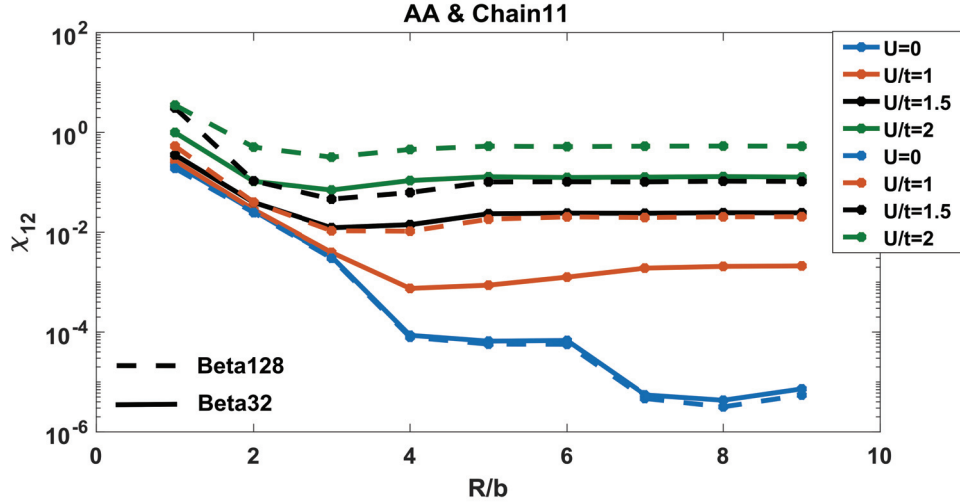


Figure 5.32. The static magnetic susceptibility between two magnetic impurities along the zigzag direction as a function of distance for the *AA* sublattice and *Chain1* is located on the edge of ZGNR. The solid lines and dashed lines are obtained by MFA calculations for different inverse temperature $\beta = 32$ and $\beta = 128$, respectively. All results show same ferromagnetic behaviour. All calculation is done for different on-site Coulomb repulsion of the host carbon atoms taken as $U_{host} = 0, 1, 1.5$ and 2 in units of t^{-1} .

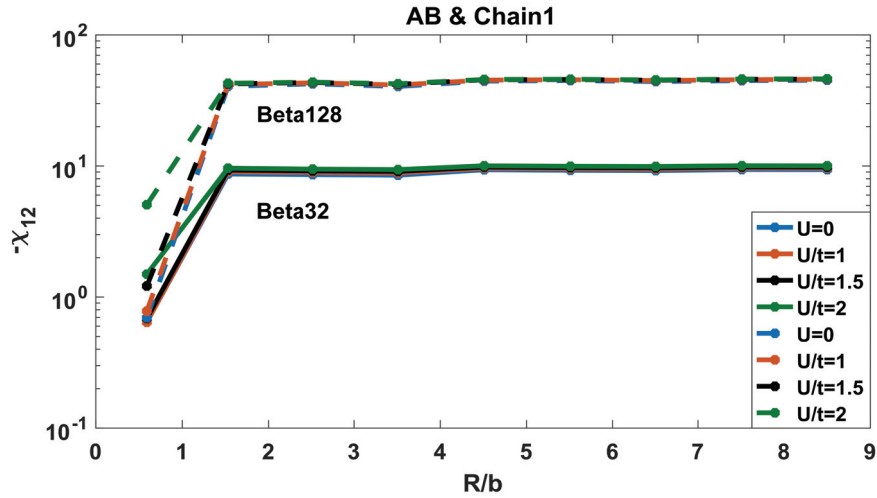


Figure 5.33. The static magnetic susceptibility between two magnetic impurities along the zigzag direction as a function of distance for the *AB* sublattice and *Chain1* is located on the edge of ZGNRs. The solid lines and dashed lines are obtained by MFA calculations for different inverse temperature $\beta = 32$ and $\beta = 128$, respectively. All results show same antiferromagnetic behaviour. All calculation is done for different on-site Coulomb repulsion of the host carbon atoms taken as $U_{host} = 0, 1, 1.5$ and 2 in units of t^{-1} .

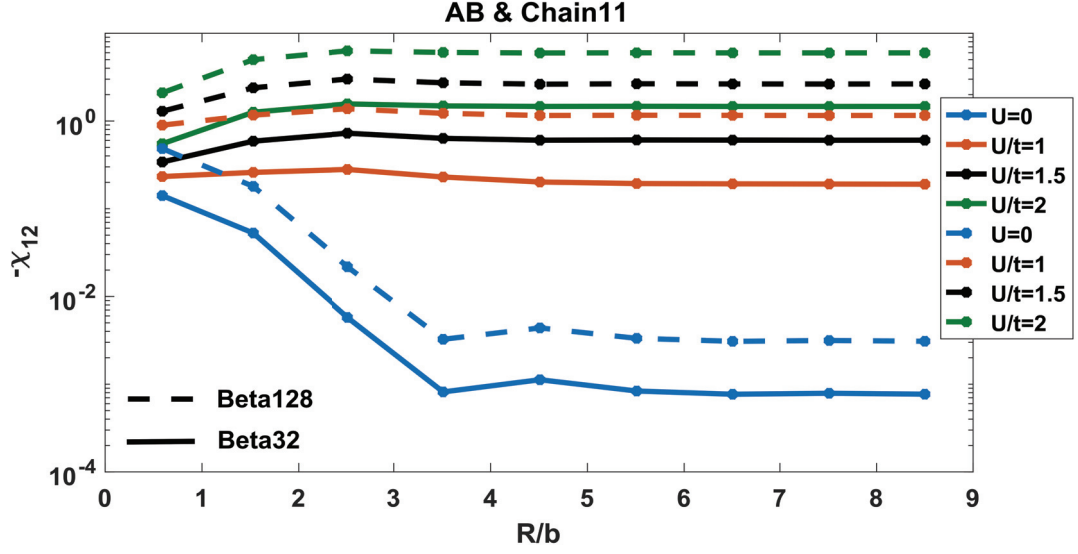


Figure 5.34. The static magnetic susceptibility between two magnetic impurities along the zigzag direction as a function of distance for the *AB* sublattice and *Chain1* is located on the middle of ZGNRs. The solid lines and dashed lines are obtained by MFA calculations for different inverse temperature $\beta = 32$ and $\beta = 128$, respectively. All results show same antiferromagnetic behaviour. All calculation is done for different on-site Coulomb repulsion of the host carbon atoms taken as $U_{host} = 0, 1, 1.5$ and 2 in units of t^{-1} .

CHAPTER 6

CONCLUSION

In this thesis, we have studied the static magnetic susceptibility between the two magnetic impurities in the zigzag graphene nanoribbons with the periodic boundary condition. The two-impurity Anderson model and mean-field Anderson model are numerically solved by using the Hirsch-Fye quantum Monte Carlo simulation and mean-field approximation, respectively. According to obtained results, when two magnetic impurities are located far from the edge sites, the static magnetic susceptibility in ZGNR with PBC is found to be strikingly consistent with the bulk graphene results in the literature despite finite system size. Moreover, our results provides the same magnetic behaviour and Fermi oscillations for the AA , BB and AB configurations like obtained RKKY results at high temperature. However, the magnetic susceptibilities are strongly enhanced and diverged from the RKKY results at low temperature. Also, we need to explain the remarkable feature of the edge effect of ZGNR. Namely, there are zero energy states at the Fermi level. Moreover, their probability distributions are only spread to upper half of ZGNR on the A sublattice. Thus, while two adatoms on the AA sublattice is approached to the edge sites, the states of the two adatoms hybridize with the zero energy edge states. Because of that, strength of the correlation is getting increased, gradually. However, when two adatoms are located on the edge sites, the states of two impurities are split from the degeneracy edge states. Consequently, magnitude of the correlations between the two impurities suddenly is decreased on the edge. On the other hand, we observed that the spin-spin correlations of two magnetic adatoms are slowly and monotonically decreased for the BB and AB sublattice configurations due to the edge effect because probability distribution of these edge states are extended on the A sublattice.

In addition, we investigated the changing effect of the chemical potential μ between the two magnetic impurities which are closest position to each other at $R/b = 1$. Also, these two adatoms are located far from edges for the AA and AB configurations at $\beta = 32$. We observed that the magnitude of the correlations between adatoms can be controlled by ejecting electrons from the system. Moreover, controllable phase transitions are occurred between two impurities from ferromagnetic to antiferromagnetic or vice versa. Furthermore, we repeated all calculations for two magnetic impurities which are located on edge sites.

Another part is that different width of the zigzag graphene nanoribbons with periodic boundary condition was investigated. We found that when width of the ZGNR is decreased, the correlations of the adatoms that are located far from the edges are affected due to hybridization between the adatoms and zero edge states. When width of the system is $W = 12$, minima and maxima points of the expected Fermi oscillations are surprisingly changed for both AA and AB configurations. On the other hand, when two impurity are located on the edge sites, the correlations behave same at every width of the system due to the fact that adatom states and zero energy edge states are separated from each other as we expected.

On the other hand, the mean-field Anderson model was examined by using the mean-field approximation. Moreover, MFA results was compared with QMC results. Strikingly, there are orders of magnitude between the mean-field approximation and quantum Monte Carlo results, when two magnetic adatom are located far from the edges. Because of that, we examined magnetization of the MFA and QMC results and faced with unexpected results. As a results of this, MFA overestimates calculations of the static magnetic susceptibility. Furthermore, we observed effect of electron-electron interactions for the host electrons. When two adatom are located far from the edge sites, there are no differences between the static magnetic susceptibilities at each inverse temperature. However, when strength of on-site Coulomb term for the host carbon atoms is progressively increased, the correlations between two magnetic impurities that are located on edge sites are significantly deviated from each other due to el-el interactions of host atoms.

REFERENCES

- Anderson, P. W. (1961, Oct). Localized magnetic states in metals. *Phys. Rev.* *124*, 41–53.
- Ashcroft, N. and N. Mermin (1976). *Solid State Physics*. HRW international editions. Holt, Rinehart and Winston.
- Awschalom, D. D. and M. E. Flatté (2007, Mar). Challenges for semiconductor spintronics. *Nature Physics* *3*, 153 EP –. Review Article.
- Berger, C., Z. Song, T. Li, X. Li, A. Y. Ogbazghi, R. Feng, Z. Dai, A. N. Marchenkov, E. H. Conrad, P. N. First, and W. A. de Heer (2004). Ultrathin epitaxial graphite: $2d$ electron gas properties and a route toward graphene-based nanoelectronics. *The Journal of Physical Chemistry B* *108*(52), 19912–19916.
- Berger, C., Z. Song, X. Li, X. Wu, N. Brown, C. Naud, D. Mayou, T. Li, J. Hass, A. N. Marchenkov, E. H. Conrad, P. N. First, and W. A. de Heer (2006). Electronic confinement and coherence in patterned epitaxial graphene. *Science* *312*(5777), 1191–1196.
- Black-Schaffer, A. M. (2010a, Aug). Importance of electron-electron interactions in the rky coupling in graphene. *Phys. Rev. B* *82*, 073409.
- Black-Schaffer, A. M. (2010b, May). Rky coupling in graphene. *Phys. Rev. B* *81*, 205416.
- Brey, L., H. A. Fertig, and S. Das Sarma (2007, Sep). Diluted graphene antiferromagnet. *Phys. Rev. Lett.* *99*, 116802.
- Bulut, N. (2002). $d \times 2 - y^2$ superconductivity and the hubbard model. *Advances in Physics* *51*(7), 1587–1667.
- Bulut, N. (2003, Dec). Quantum monte carlo study of a nonmagnetic impurity in the two-dimensional hubbard model. *Phys. Rev. B* *68*, 235103.
- Bulut, N. and S. Maekawa (2006, Oct). Strength of $d_{x^2-y^2}$ pairing in the two-leg hubbard ladder. *Phys. Rev. B* *74*, 132503.

- Bulut, N., K. Tanikawa, S. Takahashi, and S. Maekawa (2007, Jul). Long-range ferromagnetic correlations between anderson impurities in a semiconductor host: Quantum monte carlo simulations. *Phys. Rev. B* 76, 045220.
- Bunder, J. E. and H.-H. Lin (2009, Oct). Ruderman-kittel-kasuya-yosida interactions on a bipartite lattice. *Phys. Rev. B* 80, 153414.
- Cai, J., C. A. Pignedoli, L. Talirz, P. Ruffieux, H. Söde, L. Liang, V. Meunier, R. Berger, R. Li, X. Feng, K. Müllen, and R. Fasel (2014, Sep). Graphene nanoribbon heterojunctions. *Nature Nanotechnology* 9, 896–900.
- Cai, J., P. Ruffieux, R. Jaafar, M. Bieri, T. Braun, S. Blankenburg, M. Muoth, A. P. Seitsonen, M. Saleh, X. Feng, K. Müllen, and R. Fasel (2010, Jul). Atomically precise bottom-up fabrication of graphene nanoribbons. *Nature* 466, 470–473.
- Castro Neto, A. H., F. Guinea, N. M. R. Peres, K. S. Novoselov, and A. K. Geim (2009, Jan). The electronic properties of graphene. *Rev. Mod. Phys.* 81, 109–162.
- Çakmak, K. E. (2018). Effects of random atomic disorder on electronic and magnetic properties of graphene nanoribbons. Master's thesis, İzmir Institute of Technology, Turkey.
- Chappert, C., A. Fert, and F. N. Van Dau (2007, Nov). The emergence of spin electronics in data storage. *Nature Materials* 6, 813 EP –. Review Article.
- Dugaev, V. K., V. I. Litvinov, and J. Barnas (2006, Dec). Exchange interaction of magnetic impurities in graphene. *Phys. Rev. B* 74, 224438.
- Exfoliation (2018). Exfoliation and lithography: Mechanical exfoliation.
- Fischer, B. and M. W. Klein (1975, Mar). Magnetic and nonmagnetic impurities in two-dimensional metals. *Phys. Rev. B* 11, 2025–2029.
- Fujita, M., K. Wakabayashi, K. Nakada, and K. Kusakabe (1996). Peculiar localized state at zigzag graphite edge. *Journal of the Physical Society of Japan* 65(7), 1920–1923.
- Fye, R. M. and J. E. Hirsch (1988, Jul). Monte carlo study of the symmetric

- anderson-impurity model. *Phys. Rev. B* 38, 433–441.
- Geim, A. K. (2009). Graphene: Status and prospects. *Science* 324(5934), 1530–1534.
- Geim, A. K. and K. S. Novoselov (2007, Mar). The rise of graphene. *Nature Materials* 6, 183 EP –.
- Guclu, A., P. Potasz, and M. Korkusinski (2014). *Graphene Quantum Dots*. Springer.
- Guclu, A. D. and N. Bulut (2015, Mar). Spin-spin correlations of magnetic adatoms on graphene. *Phys. Rev. B* 91, 125403.
- Güçlü, A. D., M. Grabowski, and P. Hawrylak (2013, Jan). Electron-electron interactions and topology in the electronic properties of gated graphene nanoribbon rings in möbius and cylindrical configurations. *Phys. Rev. B* 87, 035435.
- Gull, E., A. J. Millis, A. I. Lichtenstein, A. N. Rubtsov, M. Troyer, and P. Werner (2011, May). Continuous-time monte carlo methods for quantum impurity models. *Rev. Mod. Phys.* 83, 349–404.
- Han, M. Y., B. Özyilmaz, Y. Zhang, and P. Kim (2007, May). Energy band-gap engineering of graphene nanoribbons. *Phys. Rev. Lett.* 98, 206805.
- Hass, J., W. A. de Heer, and E. H. Conrad (2008, jul). The growth and morphology of epitaxial multilayer graphene. *Journal of Physics: Condensed Matter* 20(32), 323202.
- Hatano, N. and M. Suzuki (2005). *Finding Exponential Product Formulas of Higher Orders*, pp. 37–68. Berlin, Heidelberg: Springer Berlin Heidelberg.
- Hirsch, J. E. (1983, Oct). Discrete hubbard-stratonovich transformation for fermion lattice models. *Phys. Rev. B* 28, 4059–4061.
- Hirsch, J. E. and R. M. Fye (1986, Jun). Monte carlo method for magnetic impurities in metals. *Phys. Rev. Lett.* 56, 2521–2524.
- Hubbard, J. (1959, Jul). Calculation of partition functions. *Phys. Rev. Lett.* 3, 77–78.

- Hubbard, J. and B. H. Flowers (1963). Electron correlations in narrow energy bands. *Proceedings of the Royal Society of London. Series A. Mathematical and Physical Sciences* 276(1365), 238–257.
- Hwang, E. H. and S. Das Sarma (2008, Oct). Screening, kohn anomaly, friedel oscillation, and rkky interaction in bilayer graphene. *Phys. Rev. Lett.* 101, 156802.
- Ising, E. (1925, February). Beitrag zur Theorie des Ferromagnetismus. *Zeitschrift fur Physik* 31, 253–258.
- Jung, J. and A. H. MacDonald (2009, Jun). Carrier density and magnetism in graphene zigzag nanoribbons. *Phys. Rev. B* 79, 235433.
- Jung, J., T. Pereg-Barnea, and A. H. MacDonald (2009, Jun). Theory of interedge superexchange in zigzag edge magnetism. *Phys. Rev. Lett.* 102, 227205.
- Kandemir, Zafer, Mayda, Selma, and Bulut, Nejat (2016). Electronic structure and correlations of vitamin b12 studied within the haldane-anderson impurity model. *Eur. Phys. J. B* 89(5), 113.
- Kasuya, T. (1956, 07). A Theory of Metallic Ferro- and Antiferromagnetism on Zener's Model. *Progress of Theoretical Physics* 16(1), 45–57.
- Kimouche, A., M. M. Ervasti, R. Drost, S. Halonen, A. Harju, P. M. Joensuu, J. Sainio, and P. Liljeroth (2015, Dec). Ultra-narrow metallic armchair graphene nanoribbons. *Nature Communications* 6, 10177. Article.
- Klinovaja, J. and D. Loss (2013, Jan). Rkky interaction in carbon nanotubes and graphene nanoribbons. *Phys. Rev. B* 87, 045422.
- Kogan, E. (2011, Sep). Rkky interaction in graphene. *Phys. Rev. B* 84, 115119.
- Kosynkin, D. V., A. L. Higginbotham, A. Sinitskii, J. R. Lomeda, A. Dimiev, B. K. Price, and J. M. Tour (2009, Apr). Longitudinal unzipping of carbon nanotubes to form graphene nanoribbons. *Nature* 458, 872–876.
- Kristjan, H. (2006). Lecture note: Quantum monte carlo method in details.

- Lee, H., J. Kim, E. R. Mucciolo, G. Bouzerar, and S. Kettmann (2012, Feb). Rkky interaction in disordered graphene. *Phys. Rev. B* 85, 075420.
- Li, X., X. Wang, L. Zhang, S. Lee, and H. Dai (2008). Chemically derived, ultrasmooth graphene nanoribbon semiconductors. *Science* 319(5867), 1229–1232.
- Lieb, E. H. (1989, Mar). Two theorems on the hubbard model. *Phys. Rev. Lett.* 62, 1201–1204.
- Ma, L., J. Wang, and F. Ding (2013). Recent progress and challenges in graphene nanoribbon synthesis. *ChemPhysChem* 14(1), 47–54.
- Magda, G. Z., X. Jin, I. Hagymási, P. Vancsó, Z. Osváth, P. Nemes-Incze, C. Hwang, L. P. Biró, and L. Tapasztó (2014, Oct). Room-temperature magnetic order on zigzag edges of narrow graphene nanoribbons. *Nature* 514, 608–611.
- Massimi, L., O. Ourdjini, L. Lafferentz, M. Koch, L. Grill, E. Cavaliere, L. Gavioli, C. Cardoso, D. Prezzi, E. Molinari, A. Ferretti, C. Mariani, and M. G. Betti (2015). Surface-assisted reactions toward formation of graphene nanoribbons on au(110) surface. *The Journal of Physical Chemistry C* 119(5), 2427–2437.
- Mayda, S. (2013). Electronic correlations in metalloproteins: A quantum monte carlo study. Master's thesis, İzmir Institute of Technology, Turkey.
- Mayda, S., Z. Kandemir, and N. Bulut (2017, Nov). Electronic structure of cyanocobalamin: Dft+qmc study. *Journal of Superconductivity and Novel Magnetism* 30(11), 3301–3308.
- Nakada, K., M. Fujita, G. Dresselhaus, and M. S. Dresselhaus (1996, Dec). Edge state in graphene ribbons: Nanometer size effect and edge shape dependence. *Phys. Rev. B* 54, 17954–17961.
- Novoselov, K. S., A. K. Geim, S. V. Morozov, D. Jiang, M. I. Katsnelson, I. V. Grigorieva, S. V. Dubonos, and A. A. Firsov (2005). Two-dimensional gas of massless dirac fermions in graphene. *Nature* 438(7065), 197–200.
- Novoselov, K. S., A. K. Geim, S. V. Morozov, D. Jiang, Y. Zhang, S. V. Dubonos, I. V.

Grigorieva, and A. A. Firsov (2004). Electric field effect in atomically thin carbon films. *Science* 306(5696), 666–669.

Onsager, L. (1944, Feb). Crystal statistics. i. a two-dimensional model with an order-disorder transition. *Phys. Rev.* 65, 117–149.

Özdemir, H. U. (2016). Electronic, magnetic and optical properties of graphene nanoribbons. Master's thesis, İzmir Institute of Technology, Turkey.

Öztarhan, G. (2018). Quantum monte carlo study of the multi-orbital anderson model including the su(2) invariant hund's coupling. Master's thesis, İzmir Institute of Technology, Turkey.

Palacio, I., A. Celis, M. N. Nair, A. Gloter, A. Zobelli, M. Sicot, D. Malterre, M. S. Nevius, W. A. de Heer, C. Berger, E. H. Conrad, A. Taleb-Ibrahimi, and A. Tejada (2015). Atomic structure of epitaxial graphene sidewall nanoribbons: Flat graphene, miniribbons, and the confinement gap. *Nano Letters* 15(1), 182–189. PMID: 25457853.

Palacios, J. J., J. Fernández-Rossier, and L. Brey (2008, May). Vacancy-induced magnetism in graphene and graphene ribbons. *Phys. Rev. B* 77, 195428.

Reina, A., X. Jia, J. Ho, D. Nezich, H. Son, V. Bulovic, M. S. Dresselhaus, and J. Kong (2009). Large area, few-layer graphene films on arbitrary substrates by chemical vapor deposition. *Nano Letters* 9(1), 30–35. PMID: 19046078.

Ruderman, M. A. and C. Kittel (1954, Oct). Indirect exchange coupling of nuclear magnetic moments by conduction electrons. *Phys. Rev.* 96, 99–102.

Ruffieux, P., S. Wang, B. Yang, C. Sánchez-Sánchez, J. Liu, T. Dienel, L. Talirz, P. Shinde, C. A. Pignedoli, D. Passerone, T. Dumslaff, X. Feng, K. Müllen, and R. Fasel (2016, Mar). On-surface synthesis of graphene nanoribbons with zigzag edge topology. *Nature* 531, 489–492.

Sandvik, A. W. and J. Kurkijärvi (1991, Mar). Quantum monte carlo simulation method for spin systems. *Phys. Rev. B* 43, 5950–5961.

Saremi, S. (2007, Nov). Rkky in half-filled bipartite lattices: Graphene as an example.

Phys. Rev. B 76, 184430.

Sherafati, M. and S. Satpathy (2011a, Sep). Analytical expression for the rky interaction in doped graphene. *Phys. Rev. B* 84, 125416.

Sherafati, M. and S. Satpathy (2011b, Apr). Rky interaction in graphene from the lattice green's function. *Phys. Rev. B* 83, 165425.

Smerieri, M., I. PÅÅ; L. Ferrighi, S. Nappini, A. Lusuan, C. Di Valentin, L. Vaghi, A. Papagni, M. Cattelan, S. Agnoli, E. Magnano, F. Bondino, and L. Savio (2016). Synthesis of graphene nanoribbons with a defined mixed edge-site sequence by surface assisted polymerization of (1,6)-dibromopyrene on ag(110). *Nanoscale* 8, 17843–17853.

Son, Y.-W., M. L. Cohen, and S. G. Louie (2006, Nov). Energy gaps in graphene nanoribbons. *Phys. Rev. Lett.* 97, 216803.

Sprinkle, M., M. Ruan, Y. Hu, J. Hankinson, M. Rubio-Roy, B. Zhang, X. Wu, C. Berger, and W. A. de Heer (2010, Oct). Scalable templated growth of graphene nanoribbons on sic. *Nature Nanotechnology* 5, 727–731.

Stratonovich, R. L. (1957). A method for the computation of quantum distribution functions. *Dokl. Akad. Nauk SSSR* 115, 1097–1100.

Suzuki, M. (1976, Jun). Generalized trotter's formula and systematic approximants of exponential operators and inner derivations with applications to many-body problems. *Communications in Mathematical Physics* 51(2), 183–190.

Tapasztó, L., G. Dobrik, P. Lambin, and L. P. Biró (2008, Jun). Tailoring the atomic structure of graphene nanoribbons by scanning tunnelling microscope lithography. *Nature Nanotechnology* 3, 397–401.

Trotter, H. F. (1959). On the product of semi-groups of operators. *Proc. Amer. Math. Soc.* 10, 545–551.

Uchoa, B., T. G. Rappoport, and A. H. Castro Neto (2011, Jan). Kondo quantum criticality of magnetic adatoms in graphene. *Phys. Rev. Lett.* 106, 016801.

- Wallace, P. R. (1947, May). The band theory of graphite. *Phys. Rev.* 71, 622–634.
- Wang, X. and H. Dai (2010, Jun). Etching and narrowing of graphene from the edges. *Nature Chemistry* 2, 661–665. Article.
- Weiss, P. (1907). L'hypothèse du champ moléculaire et la propriété ferromagnétique. *J. Phys. Theor. Appl.* 6(1), 661–690.
- Wunsch, B., T. Stauber, F. Sols, and F. Guinea (2006, dec). Dynamical polarization of graphene at finite doping. *New Journal of Physics* 8(12), 318–318.
- Yan, Z., J. Lin, Z. Peng, Z. Sun, Y. Zhu, L. Li, C. Xiang, E. L. Samuel, C. Kittrell, and J. M. Tour (2012). Toward the synthesis of wafer-scale single-crystal graphene on copper foils. *ACS Nano* 6(10), 9110–9117. PMID: 22966902.
- Yang, L., C.-H. Park, Y.-W. Son, M. L. Cohen, and S. G. Louie (2007, Nov). Quasiparticle energies and band gaps in graphene nanoribbons. *Phys. Rev. Lett.* 99, 186801.
- Yazyev, O. V. (2010, apr). Emergence of magnetism in graphene materials and nanostructures. *Reports on Progress in Physics* 73(5), 056501.
- Yazyev, O. V. and L. Helm (2007, Mar). Defect-induced magnetism in graphene. *Phys. Rev. B* 75, 125408.
- Yosida, K. (1957, Jun). Magnetic properties of cu-mn alloys. *Phys. Rev.* 106, 893–898.
- Zhang, Y., S.-Y. Li, H. Huang, W.-T. Li, J.-B. Qiao, W.-X. Wang, L.-J. Yin, K.-K. Bai, W. Duan, and L. He (2016, Oct). Scanning tunneling microscopy of the π magnetism of a single carbon vacancy in graphene. *Phys. Rev. Lett.* 117, 166801.